DISSERTATION FOR DOCTORAL (PHD) DEGREE

TAMÁS KIRÁLY

University of Sopron

Faculty of Wood Engineering and Creative Industries
Sopron

2023

PhD Dissertation
University of Sopron
Faculty of Wood Engineering and Creative Industries
József Cziráki Doctoral School of Wood Sciences and Technologies
Head of institution: Prof. Dr. Róbert Németh

DEVELOPMENT OF A NOVEL FINITE ELEMENT MODEL AND MATERIAL DEGRADATION MODEL FOR SPRUCE TIMBER SPECIMENS

Author: Tamás Király
Supervisors: Dr. Zsolt Karácsonyi
Dr. Rudolf Polgár

Sopron
2023

DEVELOPMENT OF A NOVEL FINITE ELEMENT MODEL AND MATERIAL DEGRADATION MODEL FOR SPRUCE TIMBER SPECIMENS

Dissertation for doctoral (PhD) degree
University of Sopron József Cziráki Doctoral School
of Wood Sciences and Technologies

F3 Timber Structures programme

Written by:
Tamás Király

Made in the framework of
F3 Timber Structures programme

of the József Cziráki Doctoral School, University of Sopron

Supervisors: Dr. Zsolt Karácsonyi
I recommend for acceptance (yes / no)
(signature)

Supervisors: Dr. Polgár Rudolf
I recommend for acceptance (yes / no)
(signature)

The candidate reached …..... % at the complex exam,

Sopron, ...
Chairman of the Examination Board

As assessor I recommend the dissertation for acceptance (yes/no)

First assessor (Dr. .....) yes/no
(signature)

Second assessor (Dr. .....) yes/no
(signature)

(Possible third assessor (Dr. .....) yes/no
(signature)

The candidate reached .....% in the public debate of the dissertation

Sopron,

.....
Chairman of the Assessor Committee

Qualification of the doctoral (PhD) degree ….....

.....
Chairman of the University Doctoral
and Habilitation Council (UDHC)

DECLARATION

I, the undersigned Tamás Király by signing this declaration declare that my PhD thesis entitled "**DEVELOPMENT OF A NOVEL FINITE ELEMENT MODEL AND MATERIAL DEGRADATION MODEL FOR SPRUCE TIMBER SPECIMENS**" was my own work; during the dissertation I complied with the regulations of Act LXXVI of 1999 on Copyright and the rules of the doctoral dissertation prescribed by the Cziráki József Doctoral School, especially regarding references and citations.[1]

Furthermore, I declare that during the preparation of the dissertation I did not mislead my supervisor(s) or the programme leader with regard to the independent research work.

By signing this declaration, I acknowledge that if it can be proved that the dissertation is not self-made or the author of a copyright infringement is related to the dissertation, the University of Sopron is entitled to refuse the acceptance of the dissertation.

Refusing to accept a dissertation does not affect any other legal (civil law, misdemeanour law, criminal law) consequences of copyright infringement.

Sopron, 19.11.2023

……Király Tamás……..

PhD candidate

[1] **Act LXXVI of 1999** Article 34 (1) Anyone is entitled to quote details of the work, to the extent justified by the nature and purpose of the recipient work, by designating the source and the author specified therein.

Article 36 (1) Details of publicly lectures and other similar works, as well as political speeches, may be freely used for the purpose of information to the extent justified by the purpose. For such use, the source, along with the name of the author, shall be indicated, unless this is impossible.

Acknowledgements

I would like to thank all those who helped me to write this thesis.

I thank Dr. Zsolt Karácsonyi, my PhD supervisor, for accepting me as a PhD student. He helped me with my work in the past years and reviewed my work, publications and dissertation with the utmost care.

I would also like to thank my other PhD supervisor, Dr. Rudolf Polgár, who helped me during my studies a decade ago, inspired me in writing my dissertation and he kept pushing me to achieve my goals.

I would also like to thank Vera Tolvaj, who provided me with advice and helped me with administrative issues.

Last but not least, I am indebted to my wife Júlia Király-Hasza, who encouraged and supported me throughout.

Abstract

Tamás Király, MSc mechanical engineering

An important prerequisite for the optimal use of wood as a structural building material is the determination of the strength properties of wood components using a method, that is as economical as possible. In recent years, numerical methods, such as the finite element method, have become increasingly popular as computing power has increased dramatically. Nowadays, numerous finite element models have been developed to describe wood materials. Therefore, wood as a material has been studied in a wide range of anatomical scales, trying to represent it with abstractions as accurate and realistic as possible. Based on the current literature, my research examines Norway spruce (*picea abies*) at the meso scale by approximating the annual ring pattern of specimens to obtain conclusions about their load-bearing capacity and deformation shape. The failure mechanism and the fracture of the specimens are also investigated.

The goal of my research is to develop a finite element modeling technique that can be used to investigate test specimens individually. The modeling process includes a variety of exact and abstract methods. To develop an appropriate methodology, my research includes a thorough review of the recent literature. A further goal of my research is the development and parameterization of a finite element fracture mechanics model for Norway spruce specimens, as well as the comparison of its results with measurement data. For modeling individual specimens using finite element methods, a photoanalytical processing tool was developed that recognizes the specimen in the photo and the pattern of annual rings within it. This tool is required to create a finite element model of the individual specimens.

Thus, the product of my research is a finite element modeling technique that allows to determine the load carrying capacity of a given specimen with a good approximation before measurements are performed, and a finite element damage model that allows to calculate the crack propagation in the specimen during overloading in case of brittle fracture by numerical simulation.

Kivonat

Király Tamás, diplomás gépészmérnök

A fa, mint szerkezeti építőanyag optimális felhasználásának fontos előfeltétele a faelemek szilárdsági tulajdonságainak meghatározása a lehető leggazdaságosabb módszerrel. Az elmúlt években a számítási kapacitás növekedésével a numerikus módszerek, mint a végeselem módszer is, egyre szélesebb körben nyertek teret. A faanyagok pontosabb leírásához is számos végeselemes modell látott napvilágot, ahol a fát, mint anyagot az anatómiai skála széles spektrumán próbálták meg minél valósághűbb absztrakciókkal leképezni. Az aktuális szakirodalmat tanulmányozva, kutatásom során a mezoszintű skálán vizsgálom a lucfenyőt, megközelítően leképezve a próbatestek évgyűrűit, ezáltal következtetve azok teherbírására és deformációs alakjára. A próbatestek a teljes tönkremenetelig kerülnek terhelésre és a tönkremeneteli folyamat, azaz a próbatestek törési alakja is vizsgálatra kerül.

A kutatásom egyik fő célja egy olyan végeselem modellezési technika fejlesztése, aminek segítségével a próbatestek egyedileg is lekepézhetőek. A modellezés során számos egzakt és absztrakt eljárást kell felhasználni. A megfelelő eljárás kidolgozásához, a kutatásomban nagy hangsúlyt fektetek a szakirodalmi elemzésre. A másik fő témám a lucfenyő próbatestekhez egy végeselemes törésmechanikai modell kidolgozása, paraméterezése és a mérési eredményekkel való összevetése. Az egyedi minták végeselemes leképezéséhez egy fotó analizáló program lett fejlesztve, amely felismeri a fényképen a próbatestet, valamint benne az évgyűrűk lefutását. Ez a funkció az egyedi próbatestek végeselemes modelljének létrehozásához szükséges.

A kutatásom terméke így egy modellezési eljárás, melynek segítségével a mérések elvégzése előtt jó közelítéssel megállapítható az adott próbatest terhelhetősége, valamint egy végeselemes törésmodell mely, a túlterhelés során a próbatestben végighaladó repedést képes numerikus szimulációs eljárással kiszámítani rideg törés esetén.

Table of contents

List of Figures

List of Tables

List of Abbreviations

2D or 2-D	2 Dimensional
3D or 3-D	3 Dimensional
BC	Boundary Condition
C3D8I	8-node brick, hexahedral (ABAQUS)
CT	computed tomography
deg	degrees
dGR	diameter of Growth Rings (annual rings)
DSP	Digital Speckle Photography
DXF	drawing interchange file format
Eq./Eqs.	Equations/Equations
EW	EarlyWood
FE	Finite Element
FEM	Finite Element Method
Fig.	Figure
GHT	Generalized Hough Transformation
HSV	Hue, Saturation and Value (color model)
kg	kilogram
LEFM	Linear Elastic Fracture Mechanics
LW	LateWood
LWr	LateWood ratio
m	meter
mm	milimeter
MPa	Mega Pascal
N	Newton
№	identification of specimen
R3D4	4-node rigid shell (ABAQUS)
ROI	region of interest
ROM	Rule Of Mixtures
St. Dev.	Standard Deviation

SVG	Scaleable Vector Graphics
Tab.	Table
UDMGINI	user-defined damage initiation criterion
XFEM	eXtended Finite Element Method

List of Acronyms

$\square_c$	index: compression
$\square_{EW}$	index: earlywood
$\square_L$	index: longitudinal
$\square_{LW}$	index: latewood
$\square_R$	index: radial
$\square_s$	index: shear
$\square_T$	index: tangential
$\square_t$	index: tension
A	area
A_i	area of the i-th section
$\boldsymbol{a}_I$ and $\boldsymbol{b}_I^{\alpha}$	nodal enriched degree of freedom vector
C	length of the clamping
dL_i	elongation of the i-th section
E	elastic modulus
E_c	compression modulus
E_f	flexural modulus
E_L	longitudinal modulus
E_R	radial modulus
E_T	tangential modulus
E_t	tensile modulus
F	force
f	fracture criterion
$f_{c,L}$	compressive failure stress in longitudinal direction
$f_{c,R}$	compressive failure stress in radial direction
$f_{c,R}$	compressive failure stress in tangential direction
$f_{s,L}$	failure shear stress in longitudinal direction
$f_{s,Q}$	failure shear stress in transverse direction
$f_{t,L}$	tensile failure stress in longitudinal direction
$f_{t,R}$	tensile failure stress in radial direction

$f_{t,T}$	tensile failure stress in tangential direction
f_i	fracture criterion of the i-th damage mode
F_u	ultimate force
$F_\alpha(x)$	symptotic crack-tip function
G	shear modulus
G_f	energy release rate
H	height
h	height at the edge-notch
$H(x)$	jump function
I_i	moment of inertia of the i-th section
K_{IC}	stress intensity factor
${K_{IC}}^a$	fracture toughness along the grain
${K_{IC}}^n$	fracture toughness normal to the grain
L	length of the bulk (i.e. Eq. 5) or span length (i.e. Fig. 6)
l	distance between support and edge-notch (i.e. Fig. 6)
$\overline{n}$	normal vector to the crack surface
n and m	number of earlywood and latewood rings
$N_I(x)$	I-th shape function
r_i	radius of the i-th ring
r_{xy}	correlation coefficient
SDV_FMAXI	most critical damage criterion
SDV_RFCL	compressive failure mode parallel-to-grain in longitudinal direction
SDV_RFCR	compressive failure mode perpendicular to- grain in radial direction
SDV_RFCT	compressive failure mode perpendicular to- grain in tangential direction
SDV_RFTL	tensile failure mode parallel-to-grain in longitudinal direction
SDV_RFTR	tensile failure mode perpendicular-to grain in radial direction
SDV_RFTT	tensile failure mode perpendicular-to grain in tangential direction
t_i	thickness of the i-th ring
u	deflection
$\boldsymbol{u}^{enr}$	enrichment function of standard Finite Element
$\boldsymbol{u}^{FE}$	displacement function of standard Finite Element

$\boldsymbol{u}_I$	I-th nodal displacement vector
u_u	ultimate elongation/deflection
v	Poisson's ratio
v	volume fraction
V	volume
V_c	total volume of the composite
v_i	volume fraction of the i-th constituent
v_{EW}	volume fraction of earlywood
v_{LW}	volume fraction of latewood
V_i	volume of the i-th constituent
W	width
α	angle of the arc length corresponding to the i-th ring (Eq. 5) or annual ring orientation (Fig. 6)
ϵ	strain
ρ	density
$\overline{\rho}$	average density
ρ_c	density of the composite
ρ_i	density of the i-th constituent
ρ_s	density of the cell wall material
σ	stress

1 Introduction

Wood is one of our most natural and human-friendly building materials and has played a significant role as a structural element both in the past and in the present. Considering its many advantages as a natural raw material, wood is becoming increasingly popular as a building material, not only for carpentry, but also for the construction of supporting structures (Raposo et al. 2017). As a result of this increasing usage, wood is being used in many new areas where it was not previously considered. For this reason, the material properties of wood are studied again in order to be able to improve the design of the constructions. In the last decade, it has become a trend to use wood alone or as part of a composite material (Andor et al. 2015, Raftery and Kelly 2015, Thorhallsson et al. 2017).

An important prerequisite for the optimal use of wood as a structural building material is the determination of the strength properties of wood components using a method, that is as economical as possible. Since the development of computer science at the end of the 20th century, the computational power and usability of numerical methods have increased dramatically, making complex finite element simulations increasingly popular. Recently, numerous finite element models have been developed to describe wood materials. Therefore, wood as a material has been studied in a wide range of anatomical scales, trying to represent it with abstractions as accurate and realistic as possible. Based on the current literature, my research examines Norway spruce (*picea abies*) at the meso scale by approximating the annual ring pattern of specimens to obtain conclusions about their load-bearing capacity and deformation shape. The failure mechanism and the fracture of the specimens are also investigated.

At the beginning of this research, the main goal was to develop a finite element modelling technique that, when applied to an individual specimen, can properly predict the outcome of the measurement results (i.e., deflection by a predefined loading) by simulation only. In this phase of the research, 4-point bending tests were performed with clear wood specimens with different sizes and various annual ring patterns. The results gained through experiments gave a better understanding of the behavior of timber beams under loading. Afterwards, the aim was to reconstruct the experiments by using the photos of end-grains. For the development of the finite element model of timber beams, their unique annual ring pattern is considered. The HSV color spectrum of picture of the end-grain pattern is analyzed in combination with the Canny edge detection technique using a proprietary photo analytical tool in order to separate the earlywood and latewood phases in the bulk. Based on the determined

surface ratio of the phases, it is hypothesized that the volume ratio and the surface ratio are equal. For the description of wood as a material the rule of mixtures of the fiber reinforced materials is used. As for any other modeling approach, a major issue lies in the determination of the necessary mechanical properties, and the model's performance and prediction capacity is highly dependent on these properties. The results of the compared measurements and finite element models based on the introduced hypotheses show good agreement within the linear elastic limit.

With the information obtained so far, another research objective was formulated. The idea was to create a damage model for Norway spruce, which was also adapted from the topic of fiber reinforced materials and develop the presented material model even further. The results of many researchers' experimental campaigns show how difficult it is to determine the failure properties of wood, which are often system properties rather than material properties. In this research, extended finite element method (XFEM) with linear elastic fracture mechanics (LEFM) is used to describe the crack initiation and propagation. In the cases, where Norway spruce behaves mainly like a brittle material, the results of the presented linear elastic damage model lead to a good agreement with the experiments. To describe the failure mechanisms of the Norway spruce clear wood specimens, 6 damage initiation criteria are used. A normal vector to the crack surface is calculated for each damage mode, taking into account the orientation of the maximum and minimum principal stresses. In addition, further experiments were conducted for a better understanding of the fracture properties of Norway spruce and to calibrate the developed damage model. In these experiments clear wood specimens weakened by edge-notch with different annual ring orientations were tested until failure. The specimens were subjected to 3-point bending, tension and compression tests. The failure mode during loading is investigated using a high-resolution camera. Based on the experiment results the correlation between latewood ratio, ultimate force, ultimate elongation/deflection, calculated moduli, annual ring orientation and diameter of the annual ring at the edge-notch were obtained. Based on the population data of the three tests conducted, only one parameter pair, namely the ratio of latewood to calculated modulus, influences the measurement results to almost the same extent. The other parameter pairs show different values and correlations. Ultimately, in case of brittle fracture, the goal of determining the load-bearing capacity, locating structural weakpoints, and obtaining a realistic crack propagation path by means of XFEM was achieved.

Parts of this dissertation have published in peer-reviewed conferences and/or accepted for publication. Tab. 1 provides an overview of these and shows in which chapters the content of these papers has been used.

Tab. 1: Overview of own publications used for the dissertation.

(Source: own illustration)

Publication	**Chapter**	**Thesis**
Király T., Polgár R., Andor K. (2020): Modeling the early- and latewood annual rings as orthotropic material for FE calculation of Norway spruce timber beams using the rule of mixture. Abstract book for the 16th Miklós Iványi International PhD & DLA Symposium, Pollack Press, pp. 73-74	1, 2, 3, 4, 5	1, 2
Király T. (2021): Macroscopic Material Degradation Model of Wood for XFEM using the Rule of Mixtures. Abstract book for the 17th Miklós Iványi International PhD & DLA Symposium, Pollack Press, pp. 147-148	1, 6	3
Király, T., & Karácsonyi, Z. (2023a): Fracture testing of edge-notched timber beams with different growth ring orientations. Wood Research, Vol. 68(3), pp. 558–571	1, 3	
Király, T., Karácsonyi, Z., & Polgár, R. (2023b): Modeling the earlywood and latewood growth rings of Norway spruce timber beams for finite element calculation. Wood Research, Vol. 68(1), pp. 28–43	1, 2, 3, 4, 5	1, 2
Király, T., Karácsonyi, Z., & Polgár, R. (2023c): Macroscopic material degradation model of Norway spruce clear wood for XFEM. Results in Materials	1, 3, 4, 5, 6	3

2 Material model

2.1 Structure of wood

The macroscopic properties of wood, such as density, hardness and other properties, are derived from the cells that make up the wood. There is a strong relationship between density and strength of the wood (Ross 2010). Therefore, density of wood is considered one of the most important parameters that determine its mechanical and physical properties. It also determines the quality and use of the wood, because with a higher density it has greater strength and is therefore more suitable for loadbearing structures. Other properties that affect strength, such as variation in moisture content or consideration of local material defects in the form of knots and splits, are not considered in this research due to the novelty of the finite element modeling method.

The earlywood is the portion of the annual ring that is formed during the early part of the growing season. It has a brighter color and it is less dense and weaker mechanically than latewood, because it contains larger lumina and thinner cell walls than the latewood (Bodig and Jayne 1993). The latewood is the part of the annual ring that forms after the end of the earlywood formation. It has a darker color, it is denser and stronger mechanically than earlywood, because its cells are densely layered and its walls are stronger and thicker. This is due to the colder temperatures and drier conditions. The transition from earlywood to latewood is abrupt, usually without a distinct transition-zone (Ross, 2010). In past decades, many researchers have published on the elastic behavior of spruce timber (Keunecke et al. 2007, Dívós and Horváth 2006, Dahl and Malo 2009, Ebrahimi and Sliker 1981, Hearmon 1948, Fajdiga et al. 2019).

The wood as a material has a cylindrical symmetry (Szalai 1994), see Fig. 1. Its longitudinal direction is along the axis, while radial and tangential directions are in the transverse plane. The longitudinal modulus E_L of wood is over 10 times larger than the radial modulus E_R or tangential modulus E_T, whereas the radial and tangential moduli are considered similar but the difference should not be ignored. Therefore, wood may be described as an orthotropic material and its three mutually perpendicular axes are (Ross 2010): the longitudinal axis "L" (parallel to the fiber grain), the radial axis "R" (normal to the annual rings, perpendicular to the grain in the radial direction) and the tangential axis "T" (perpendicular to the grain but tangent to the annual rings).

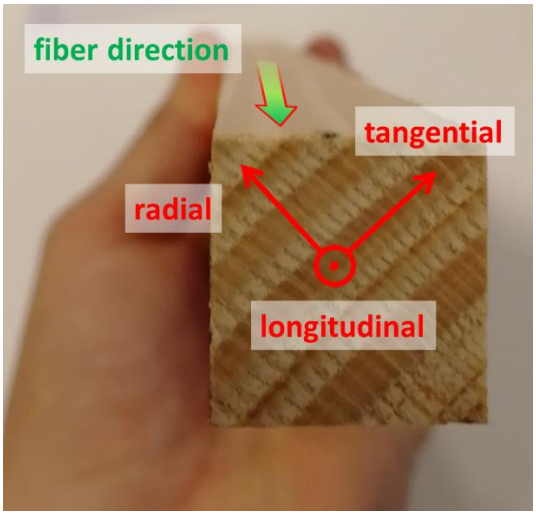

Fig. 1: Wood as an orthotropic material and it's three principial axes.
(Source: own illustration)

Depending on the purpose, researchers carried out studies at the micro scale, the cells and its structure (Modén and Berglund 2008, Salmén and Megistris 2008, Qing and Mishnaevsky 2010) and at meso or macro scale, so they consider the bulk itself with or without annual rings (Fleischmann 2005, Qing and Mishnaevsky 2010, Sandhaas and van de Kuilen 2013, Gereke et al. 2015, Shao et al. 2020, Moshtaghin et al. 2021). Some researchers have found it obsolete to take into account the annual rings of the wooden beams and claim to have obtained good results by considering other kind of abstractions (Zhu 2014, Gecys et al. 2015, Saad and Lengyel 2021). According to Qing and Mishnaevsky Jr. (2010), not taking into account the structure of the softwood by distinguishing just low density (earlywood) and high density (latewood) regions, leads to an oversimplification. Considering the orientation of the annual rings is therefore of great importance. Many researchers took a two-phased wood model into account by investigating the annual rings, the earlywood and latewood, for various applications (Serrano and Enquist 2010, Hu et al. 2018, Fajdiga et al. 2019, Belalpour et al. 2021).

In the past years many computational models of wood were developed (Fleischmann 2005, Modén and Berglund 2008, Ormarsson et al. 2008, Qing and Mishnaevsky 2010, Sandhaas and van de Kuilen 2013). The earlywood and latewood are treated as homogeneous, but the bulk is considered as a composite material, thus heterogeneous. The challenge is to distinguish regions governed by having earlywood and latewood in the bulk in focus, and nevertheless to determine the material properties of earlywood and latewood.

2.2 Abstractions to describe wood as a material

After a thorough study of the current literature, I decided to explicitly model earlywood and latewood in a meso scale, which means modelling timber beams with individual annual rings. Models of softwoods, that take into account more relevant levels of wood structure, offer a better understanding of the mechanical properties and strength of wood. Some kind of abstraction is needed to create a material model that describes wood as a complex material. The two main abstractions introduced in this research are treated as hypotheses. To examine their reality base, measurement results were compared with the results of finite element models based on the hypotheses.

2.2.1 Surface ratio equals volume ratio

For predicting the mechanical properties of fiber reinforced materials, the rule of mixtures (ROM) is used, as a weighted mean. In broadest definition a composite is a combination of at least two constituents (Isaac and Ori 2006). Considering wood as a composite material because of the annual rings, the formulas of the fiber reinforced materials can be reinterpreted to the earlywood and latewood. Some also considered the micromechanical properties on different scale levels from microfibrils to annual rings (Qing and Mishnaevsky 2010). In the following investigation, the determination of the properties of the earlywood and the latewood is carried out semi-empirically.

The following general formula defines the composition of a mixture with a dimensionless quantity (Warnet and Akkerman 2008, Eq. 2.1-3):

$$\sum_{i=1}^{n} \mathrm{v_i} = 1 \quad \text{with} \quad \mathrm{v_i} = \frac{V_i}{V_c} \tag{1}$$

where: $\mathrm{v_i}$ is the volume fraction of the i-th constituent, V_i is the volume of the i-th constituent, V_c is the total volume of the composite. The similar rule for mass content by substituting the product of density and volume leads to (Warnet and Akkerman 2008, Eq. 2.1-4):

$$\rho_c = \sum_{i=1}^{n} \rho_i \ \mathrm{v_i} \tag{2}$$

Now rewriting the formula of the relative content of the earlywood and latewood:

$$\mathrm{v}_{EW} + \mathrm{v}_{LW} = 1 \tag{3}$$

$$\overline{\rho} = \rho_{EW} \cdot \mathrm{v}_{EW} + \rho_{LW} \cdot \mathrm{v}_{LW} \tag{4}$$

where: $\overline{\rho}$ is the average density of analyzed wooden structure (this value can be easily measured), v_{EW}, ρ_{EW} is the relative volume and density of the earlywood respectively and v_{LW}, ρ_{LW} is the relative volume and density of the latewood respectively.

Hypothesis 1 (Király et al. 2020) (Király et al. 2023a): For class A (highest quality class) or class B wood it can be assumed, that proportion of earlywood and latewood in the end cross-section of the analyzed beam is constant in all cross-sections along its longitudinal axis. This assumption leads to:

$$V = L \cdot (A_{EW} + A_{LW}) = L \cdot \left(\sum_{i=1}^{n} \alpha_i^{EW} \cdot r_i^{EW} \cdot t_i^{EW} + \sum_{i=1}^{m} \alpha_i^{LW} \cdot r_i^{LW} \cdot t_i^{LW} \right) \quad \text{with n , m} \gg 1 \tag{5}$$

where: n and m is the number of earlywood and latewood rings, r_i is the radius of the i-th ring, t_i is the thickness of the i-th ring and α refers to the angle of the arc length corresponding to the i-th ring. If n and m is high enough, it can be assumed the amount of earlywood and latewood rings is equal and the Eq. 5 can be further simplified.

The density of the earlywood and latewood rings can be determined by measuring finite small specimens. If the assumptions are good enough, the given formula should lead to the measured weight of the beam.

The assumption in the hypothesis that the wood should be of class A (or B) (Anon. 1997) is necessary because the inclusion of significant wood defects, such as knots, would make this research much more difficult. Given the novelty of the development, I am not in a position to address this in the present research.

2.2.2 Stiffness relations for the Norway spruce between earlywood and latewood

The ROM is used for establishing a connection between the composite bulk and its two phases, the earlywood and latewood. The two basic models used for linear elastic materials are the Voigt's and Reuss models. Fig. 2 is valid for the two-phase composite materials.

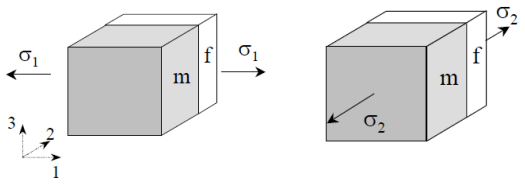

Fig. 2: Voigt's (left) and Reuss-model (right).

(Source: Warnet and Akkerman 2008)

The longitudinal modulus E_L and tangential modulus E_T are obtained by considering that earlywood and latewood rings are in parallel. The average stress $\sigma_{L/T}$ in the cross-section is:

$$\sigma_{L/T} = \sigma_{EW,\mathrm{L/T}} \cdot \mathrm{v}_{EW} + \sigma_{LW,\mathrm{L/T}} \cdot \mathrm{v}_{LW} \tag{6}$$

According to the strain energy approach and by acknowledging the orthotropic character of the earlywood and latewood, the strains induced in both are equal:

$$E_{L/T} \cdot \epsilon_{L/T} = E_{EW,\mathrm{LT}} \cdot \epsilon_{EW,L/T} \cdot \mathrm{v}_{EW} + E_{LW,L/T} \cdot \epsilon_{LW,L/T} \cdot \mathrm{v}_{LW} \tag{7}$$

The radial modulus E_R is obtained by considering that earlywood and latewood rings are in series. The strain ϵ_R is the sum of the strain of the earlywood and latewood rings:

$$\epsilon_R = \epsilon_{EW,R} \cdot \mathrm{v}_{EW} + \epsilon_{LW,R} \cdot \mathrm{v}_{LW} \tag{8}$$

For linear-elastic material using the Hooke's law, it can be written as:

$$\frac{\sigma_R}{E_R} = \frac{\sigma_{EW,R} \cdot \mathrm{v}_{EW}}{E_{EW,R}} + \frac{\sigma_{LW,R} \cdot \mathrm{v}_{LW}}{E_{LW,R}} \tag{9}$$

In case of the Reuss-model the stresses σ_R, $\sigma_{EW,R}$ and $\sigma_{LW,R}$ are equal.

$$\frac{1}{E_R} = \frac{\mathrm{v}_{EW}}{E_{EW,R}} + \frac{\mathrm{v}_{LW}}{E_{LW,R}} \tag{10}$$

For the shear moduli, the approach of the radial modulus is used:

$$\frac{1}{G} = \frac{\mathrm{v}_{EW}}{G_{EW}} + \frac{\mathrm{v}_{LW}}{G_{LW}} \tag{11}$$

$$G = \frac{G_{EW} \cdot G_{LW}}{\mathrm{v}_{LW} \cdot G_{EW} + \mathrm{v}_{EW} \cdot G_{LW}} \tag{12}$$

Qing and Mishnaevsky Jr. (2010) doesn't mention any approach how to determine the ROM of shear moduli. According to some research results (Gereke et al. 2015), there is no need for the ROM to be used to determine the Poisson's ratios. The same Poisson's ratios can be applied to earlywood and latewood as well. The formulas proposed so far allow determination of material properties of the analyzed wooden beams if the properties of the two

phases, earlywood and latewood, are known. These equations give the ROM-relation for the orthotropic material parameters.

If the material properties of wood as a composite of earlywood and latewood are unknown, the proposed way of solution has to be inverted to calculate the unknown values. Yet there is a need to obtain more equations to describe the relationship between earlywood and latewood. Jernkvist and Thuvander (2001) used an optical method, called digital speckle photography (DSP), to measure the radial dependence of material properties of Norway spruce. The DSP is well suited for measurements on objects with small details, since the method can be combined with microscopy.

Hypothesis 2 (Király et al. 2020) (Király et al. 2023a): rules of mixtures combined (Eqs. 13-15) with the correlation between the orthotropic material properties and density of earlywood and latewood lead to Eqs. 16-22. The following considerations of obtaining stiffness relations for Norway spruce take the difference between the cells of earlywood and latewood into account while referencing on other publications with experimental values.

The ROM-relation of the longitudinal and tangential modulus:

$$E_{L/T} = E_{EW,\mathrm{L/T}} \cdot \mathrm{v}_{EW} + E_{LW,\mathrm{L/T}} \cdot \mathrm{v}_{LW} \tag{13}$$

After the rearrangement of the Eq. 10, the following equation gives the ROM-relation of the radial modulus:

$$E_R = \frac{E_{EW,R} \cdot E_{LW,R}}{\mathrm{v}_{LW} \cdot E_{EW,R} + \mathrm{v}_{EW} \cdot E_{LW,R}} \tag{14}$$

The ROM-relation of the shear moduli:

$$G = \frac{G_{EW} \cdot G_{LW}}{\mathrm{v}_{LW} \cdot G_{EW} + \mathrm{v}_{EW} \cdot G_{LW}} \tag{15}$$

The Poisson's ratios of the earlywood and latewood are considered equal.

The Eqs. 16-22 define the stiffness relations for the Norway spruce between earlywood and latewood. Gibson and Ashby (1997) observed a linear relation between density and longitudinal modulus E_L (Eq. 16). Gibson and Ashby (1997) and Nairn (2006) predicted that tangential modulus scales with the cube of density (Eq. 17). Recent publication from Modén and Berglund (2008) propose a scaling of the radial modulus less than cubic, also like in Nairn (2006) (Eq. 18). Measuring the shear moduli by generating pure shear deformation state, comes with great difficulty. Gibson and Ashby (1997) observed a cubic relation between density, G_{RT} and E_L, a linear relation between density, $G_{TL/RL}$ and E_L, (Eqs. 19, 20). Other publications, e.g.

(Qing and Mishnaevsky 2010), suggest to select a reasonable value like the one of the bulk or empirical values obtained through parameter studies of earlywood and latewood.

The Poisson's ratios $\nu_{EW/LW,TL}$ and $\nu_{EW/LW,RL}$ have very small values and their determination (Eq. 21) is less precise than for ν_{TR} (Ross 2010). The DSP measurements of Jernkvist and Thuvander (2001) showed the inequality of $\nu_{EW,RT}$ and $\nu_{LW,RT}$. Due the lack of a more precise determination these values, in this paper the Poisson's ratios in Eq. 22 are considered as equal.

$$E_{LW,L} = E_{EW,L} \cdot \left(\frac{\rho_{LW}}{\rho_{EW}}\right) \tag{16}$$

$$E_{LW,T} = E_{EW,T} \cdot \left(\frac{\rho_{LW}}{\rho_{EW}}\right)^3 \tag{17}$$

$$E_{EW,R} = E_{LW,R} \cdot \left(\frac{\rho_{LW}}{\rho_{EW}}\right)^{1.63} \tag{18}$$

$$G_{LW,RT} = G_{EW,RT} \cdot \left(\frac{\rho_{LW}}{\rho_{EW}}\right)^3 \tag{19}$$

$$G_{LW,TL/RL} = G_{EW,TL/RL} \cdot \left(\frac{\rho_{LW}}{\rho_{EW}}\right) \tag{20}$$

$$\nu_{EW,\mathrm{TL/RL}} = \nu_{LW,\mathrm{TL/RL}} = \nu_{\mathrm{TL/RL}} \tag{21}$$

$$\nu_{LW,RT} \sim \nu_{EW,RT} \tag{22}$$

(but in the reality $\nu_{LW,RT} > \nu_{EW,RT}$)

In the following only linear material behavior of wood is considered. This means nonlinearities in material properties, such as different stiffness values in tension and compression parallel to grain are not taken into account. To guarantee the positive-definiteness of the elasticity tensor, the following conditions have to be fulfilled:

$$\nu_{LR}^2 < \frac{E_L}{E_R}, \qquad \nu_{LT}^2 < \frac{E_T}{E_L}, \qquad \nu_{RT}^2 < \frac{E_R}{E_T} \tag{23}$$

$$1 - \nu_{LR}^2 - \nu_{LT}^2 - \nu_{RT}^2 - 2 \cdot \nu_{LR} \cdot \nu_{LT} \cdot \nu_{RT} > 0 \tag{24}$$

3 Experiments

3.1 Description of the conducted experiments

A preliminary investigation of relevant researches was conducted before planning and conducting the experiments. The most common test to determine the strength of wood are tension, compression, static bending, indentation, shear and brittleness tests. Testing small clear specimens is the most reliable comparison of different species (Tampone 2007). Sliker and Yu (1993) presented the elastic constants for hardwoods from measurement data by carrying out plate and tension tests. Liu (2002) presented a stress analysis of the off-axis tension test using an orthotropic material model. The off-axis tension test is attractive because of its economy and ease of application. Liu and Ross (2005) estimated the compressive modulus in radial direction with his verified shear modulus model, based on the weak band theory (Bodig 1965). In the radial direction, earlywood and latewood layers are arranged in series and both layers carry the same load, but the latewood deforms much less. The failure occurs therefore in the weakest earlywood band.

Within the scope of the doctoral dissertation, 2 measurement campaigns were conducted. In the first measurement campaign, only 4-point bending tests were performed. In this measurement campaign, the aim was to develop a modeling method of timber beams with linear elastic material properties. To compare the tested specimens, the most obvious choice was to determine the elastic modulus. In addition, the specimens were weighed and photographed from all sides before testing, in order to estimate the latewood ratio, like proposed in chapter 2.2. In the second measurement campaign, 3-point bending, tensile and compression tests were carried out with edge-notched specimens. The aim of this series of tests was to investigate the fracture behavior of specimens with different annual ring patterns under different types of loading. The measurements were filmed with a high-resolution camera and the force-displacement curves were documented as well.

3.2 First measurement campaign: 4-point bending tests

3.2.1 Measurement setup

As the first measurement campaign, 4-point bending tests with small sized timber beams were conducted in a laboratory accredited for timber structural testing. These destructive tests were performed according to DIN EN 408-2012-10 (2012) using the material testing device FPZ-100. The load was applied by a single actuator and transmitted to the centrally aligned specimen with a rate of 5 $mm \cdot min^{-1}$. The measurement of the deflection at the middle of the timber beam

was performed with a videoextensometer, which was connected to a computer storing all the recorded data, like depicted on Fig. 3.

Fig. 3: 4-point bending test measurement set-up of the specimens (left); Videoextensometer for non-contact measurement of strain and material parameters (right).

(Source: own illustration)

All of the specimens were sawn of Norway spruce (*picea abies*) in rectangular solid cross-sections and dried to a moisture content of 12%. The experiments were carried out at a room temperature of 20°C. Tab. 2 shows the measurement setup of the specimens.

Tab. 2: Measurement setup of 4-point bending tests

(Source: own illustration)

Specimens (mm)	**Span of pressure stamps**		**Radius of stamps** (mm)
	L_A (mm)	L_B (mm)	
20 x 20 x 400	120	360	15
40 x 40 x 800	230	650	15

The idea of using 20 x 20 mm cross-sectioned beams (Fig. 4a) was based on ensuring with visual inspection (followed by a destructive test), that none of the specimens has a major visible defect, drying splits or even knots, which is a natural feature of the species. It is safe to say, that the carefully selected specimens did not contain any major failures, which could have had an effect on the mechanical properties. The 40 x 40 mm specimens are shown in Fig. 4b. Via visual inspection and non-destructive tests, it was ensured that none of the specimens used for the experiments had major defects, yet the presence of small knots was allowed. Slightly damaged end-cross-sections (like specimen 10, damaged on both sides) require to extrapolate beyond the range of acquirable information.

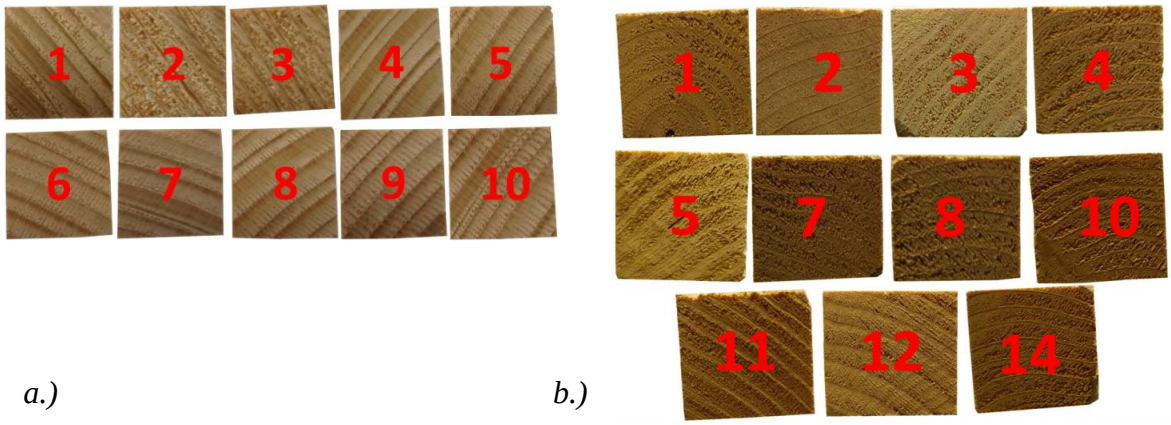

a.) *b.)*

Fig. 4: a.) End-grains of the 20x20 specimens; b.) End-grains of the 40x40 specimens. (Source: own illustration)

3.2.2 Experiment results

For the experiment with 20x20 specimens shown in Tab. 3, a total of 10 specimens were prepared. The measured density of the given specimens gave an average 551.37 kg.m-3 with a standard deviation of 50.19. The average ratio of the latewood proportion is 38.45% with a standard deviation of 6.70%.

For the 40x40 specimens, 14 pieces were prepared for measurements, see Tab. 4. Due to errors during the measurement of the specimens 6, 9 and 13 have no results available. The measured density of the given specimens gave an average 327.19 $kg \cdot m^{-3}$ with a standard deviation of 15.80. The average ratio of the latewood proportion is 19.00% with a standard deviation of 2.23%.

A higher proportion of latewood is observed in case of the 20x20 specimens. The earlywood and latewood separation error is more pronounced in smaller samples, and Fig. 4 shows that the specimens are from different bulk and thus from a different population.

The error in separating earlywood and latewood is more pronounced in smaller specimens. Additionally, Fig. 4 shows that the specimens are from different log and thus from a different population.

Tab. 3: Experiment results of the 20x20 specimens

(Source: own illustration)

№	**Cross-section** (mm)	**Ratio of latewood** (%)	**Weight** (g)	**Density** ($kg \cdot m^{-3}$)	**Max deflection** (mm)	**Ultimate load** (kN)	**Deflection by 0.5 kN** (mm)
1	19.54 x 20.18	43.68	98	621.33	11.642	1.585	2.889
2	19.52 x 19.93	36.51	79	507.67	9.744	1.523	2.377
3	19.61 x 20.15	28.46	74	468.19	12.280	1.529	2.751
4	19.67 x 19.85	48.63	97	621.08	12.876	1.619	3.224
5	19.69 x 20.23	32.68	81	508.37	14.578	1.644	3.047
6	19.73 x 20.33	29.61	84	523.55	17.423	1.727	2.839
7	20.12 x 19.81	42.65	93	583.32	16.957	1.763	2.927
8	19.74 x 20.13	44.69	89	559.94	12.616	1.543	2.994
9	19.79 x 20.22	37.86	88	549.79	18.064	1.761	3.312
10	19.78 x 20.16	39.74	91	570.51	12.804	1.625	3.139
Average	19.72 x 20.10	38.45	87.4	551.37	13.901	1.632	2.951
St. dev.	0.17 x 0.17	6.70	7.8	50.19	1.630	0.092	0.266

Tab. 4: Experiment results of the 40x40 specimens

(Source: own illustration)

№	**Cross-section** (mm)	**Ratio of latewood** (%)	**Weight** (g)	**Density** ($kg \cdot m^{-3}$)	**Max deflection** (mm)	**Ultimate load** (kN)	**Deflection by 0.5 kN** (mm)
1	40.58 x 41.49	16.27	460	341.510	11.560	3.167	8.679
2	41.35 x 40.05	21.21	417	314.776	12.064	3.733	7.563
3	39.43 x 41.11	19.35	409	315.449	16.138	4.267	7.738
4	40.73 x 41.20	21.52	418	311.372	10.605	3.250	7.985
5	41.36 x 39.56	18.33	407	310.926	15.936	4.517	7.597
7	40.26 x 38.97	17.93	447	356.170	15.125	4.767	6.639
8	40.27 x 39.65	16.07	402	314.699	10.431	2.933	8.337
10	41.46 x 40.06	17.64	437	328.921	12.207	3.733	7.702
11	39.95 x 39.33	22.37	414	329.317	13.025	3.900	7.855
12	39.55 x 41.64	18.03	445	337.808	11.433	3.383	7.883
14	39.17 x 40.21	20.33	426	338.110	13.739	3.950	8.351
Average	40.37 x 40.30	19.00	425.6	327.187	12.933	3.782	7.848
St. dev.	0.85 x 0.97	2.23	20.0	15.801	2.156	0.608	0.562

3.3 Second measurement campaign: 3-point bending, tension- and compression tests

3.3.1 Measurement setup

The second measurement campaign consists of 3 different types of tests: 3-point bending, tension- and compression tests. To capture the more complex fracture mechanisms, all of these measurements were taken perpendicular to the grain orientation. As in case of the first measurement campaign, all the experiments with edge-notched timber specimens were

conducted in a laboratory accredited for timber structural testing. All the specimens were sawn of Norway spruce (*picea abies*) and dried to a moisture content of 12%. The experiments were carried out at a room temperature of 20°C. The equipment used for the tests consists of a material testing machine (Tinius Olsen H10KT), an LED lamp (Jinbei EF-200) as an additional light source focused on the sample, a camera with Red Dragon 5K sensor and Samyang 3.1/100 mm optics. The displacement was controlled at a constant speed during a test. The feed rates of the specimens were documented in the range of 0.1 – 5 mm·min^{-1}.

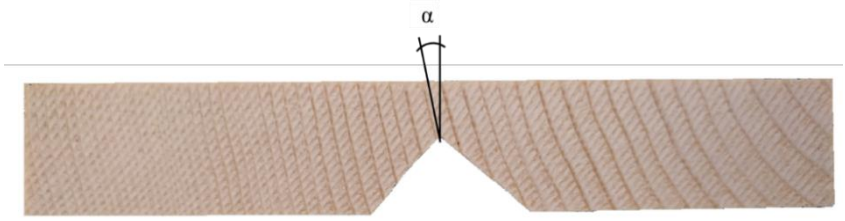

Fig. 5: Annual ring orientation (α) in the specimen at the notch (Source: own illustration)

The orientation of annual rings in the specimens are aligned in an angle α between 0 to 90 degrees as shown in Fig. 5. The value of α is 0, if the end-grains are perpendicular to the longitudinal axis of the specimen and 90, if the end-grains are parallel. In the population, the mode of failure is the same between similar specimens, but the cracking may vary depending on the orientation of the annual rings. The diameter of the annual rings (dGR) at the location of the edge-notch is also documented in the table of specimen data (Tab. 5, Tab. 6 and Tab. 7). The proportions of latewood and earlywood in the specimens are determined using a photo-analytical algorithm, discussed later in chapter 4.2 and 4.3. As suggested in before in chapter 2.2, the volume ratio of the latewood in the specimen can be estimated from its surface ratio.

3.3.1.1 3-point bending tests

This test method covers the determination of the flexural properties of structural beams (ASTM D198-02). The flexural modulus E_f (also called bending modulus) is a property that is computed as the ratio of stress to strain in flexural deformation and it describes the tendency for a material to resist bending (Yoshihara et al. 1998). As bending occurs in the specimen, its top surface experiences compression while the bottom side experiences tension. Calculation of flexural modulus E_f of the 3-point bending tests for rectangular shaped specimens with constant cross-section, where u stands for the maximal deflection of the beam under the load F:

$$E_f = \frac{F \cdot L^3}{u \cdot 4W \cdot H^3} \tag{25}$$

Because of the edge-notch, the cross-section and also the moment inertia of area must be considered as variable. As a conservative simplification, the cross section with the edge-notch is considered with a rectangular cross section with height "h" (Fig. 6):

$$I_1 = \frac{W \cdot H^3}{12} \quad for\ 0 \le x \le l \tag{26}$$

$$I_2 = \frac{W \cdot h^3}{12} + \left(\frac{H-h}{2}\right)^2 \cdot W \cdot H \quad for\ l < x \le \frac{L}{2} \tag{27}$$

The Eq. 25 can be extended in the following way, to get more accurate results:

$$E_f = \frac{F}{u \cdot I_2}\left(\frac{L^3}{48} + \frac{l^3}{3}\right) + \frac{F}{u \cdot I_1} \cdot \frac{l^3}{6} \tag{28}$$

The parameters of the specimens used for the 3-point bending test are as shown in Fig. 6 and Tab. 5.

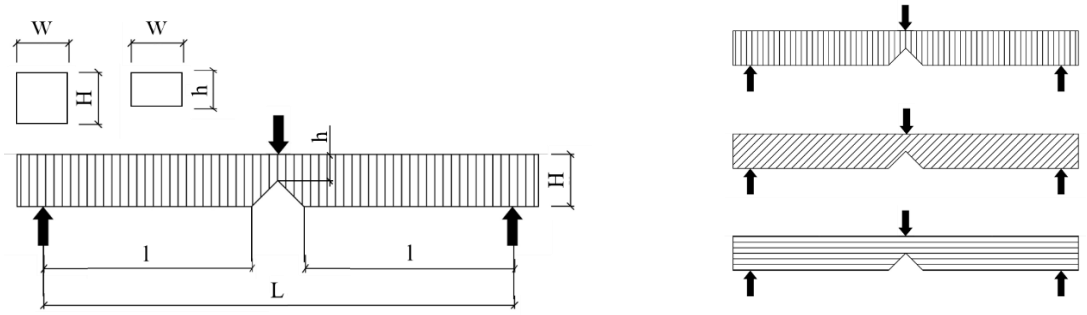

Fig. 6: Schematic of specimen types with different annual ring orientations used for the 3-point bending test: L – span length of specimen, W – width of specimen, h – height at the notch, l – distance between support and edge-notch.

(Source: own illustration)

Tab. 5: Data of specimens used for the 3-point bending test

(Source: own illustration)

№	**L** (mm)	**W** (mm)	**h** (mm)	**α** (deg)	**Weight** (g)	**Latewood ratio** (%)	**Feed rate** (mm/min)	**dGR** (mm)
HA01	110.0	20.1	8.9	28.6	18.95	17.4	0.1	194.4
HA02	110.0	20.0	9.0	16.2	18.16	15.5	0.1	167.5
HA03	110.0	20.0	8.8	24.0	18.69	18.3	0.1	156.7
HA04	110.0	20.0	8.9	23.2	19.05	12.7	0.1	147.4
HA05	50.0	20.6	9.7	3.0	14.77	11.5	0.5	70.4
HA06	50.0	20.6	9.5	6.7	14.65	12.1	0.5	68.4
HA07	50,0	20.7	10.5	2.5	14.88	16.0	0.5	66.6
HA08	110.0	20.3	9.4	90.0	24.60	18.2	1.0	92.0
HA09	110.0	20.3	9.4	90.0	24.61	16.0	1.0	94.3

3.3.1.2 Tension tests

This test method covers the determination of the tensile properties of structural elements made primarily of lumber equal to and greater than nominal 1 inch (19 mm) thick (ASTM D198-02). The specimen is clamped at the extremities of its length and subjected to a tensile load so that in sections between clamps the tensile forces shall be axial and generally uniformly distributed throughout the cross-sections without flexure along its length.

Wood has a moderately high tensile strength and requires a high clamping force device to secure it. Wood is also moderately soft, which presents a challenge for conventional mechanical vices. The basic formula for obtaining the elastic tensile modulus E_t in case of tension:

$$E_t = \frac{\sigma}{\epsilon} = \frac{F/A}{dL/L} \tag{29}$$

Because of the edge-notch, the cross-section must be considered as variable. Elongation dL of the specimen can be considered as springs connected in series. The total elongation corresponds to the sum of the length changes of the individual sections of the specimen:

$$dL = 2 \cdot dL_1 + dL_2 = \frac{F}{E_t} \cdot \left(\frac{2 \cdot l}{A_1} + \frac{L - 2 \cdot l}{A_2}\right) \tag{30}$$

The cross-sections of the considered segments are:

$$A_1 = W \cdot H \tag{31}$$

$$A_2 = W \cdot h \tag{32}$$

The Eq. 29 is therefore extended in the following way:

$$E_t = \frac{F}{dL} \cdot \left(\frac{2 \cdot l}{A_1} + \frac{L - 2 \cdot l}{A_2}\right) \tag{33}$$

The parameters of the specimens used for the tension test are as shown in Fig. 7 and Tab. 6.

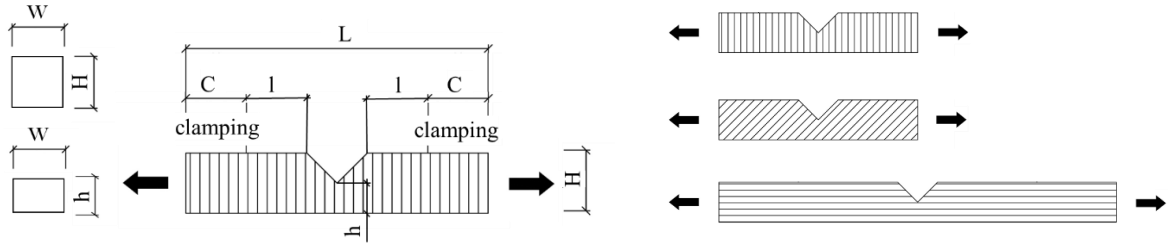

Fig. 7: Schematic of specimen types with different annual ring orientations used for the tension test: L – free length of specimen, W – width of specimen, C – length of the clamping, h – height at the notch, l – distance between clamping and edge-notch.

(Source: own illustration)

Tab. 6: Data of specimens used for the tension test

(Source: own illustration)

№	**L** (mm)	**C** (mm)	**W** (mm)	**h** (mm)	**α** (deg)	**Weight** (g)	**Latewood ratio** (%)	**Feed rate** (mm/min)	**dGR** (mm)
HU01	160.0	40.0	19.9	13.1	90.0	31.29	11.3	0.1	56.7
HU02	160.0	40.0	20.0	12.0	90.0	32.67	13.2	0.1	95.0
HU03	160.0	40.0	20.1	13.1	33.4	32.23	12.4	0.1	124.9
HU04	80.0	20.0	20.2	8.5	22.4	18.85	13.2	0.1	138.8
HU05	80.0	20.0	20.5	9.8	3.9	14.55	14.2	0.1	140.0
HU06	80.0	20.0	20.5	9.7	9.3	14.64	14.0	0.1	134.0
HU07	80.0	20.0	20.6	9.1	11.8	14.63	15.1	0.1	114.7
HU08	160.0	40.0	20.2	10.3	90.0	24.17	16.3	0.1	145.6
HU09	160.0	40.0	20.0	10.0	90.0	24.11	17.2	1.0	148.8

3.3.1.3 Compression tests

This test method covers the determination of the compressive properties of elements taken from structural members made of solid wood, when such an element has a slenderness ratio (length to least radius of gyration) of less than 17 (ASTM D198-02). If the slenderness ratio is less than 17, the specimen is considered small and no lateral support is required. The elastic compression modulus E_c can be obtained by using Eq. 33.

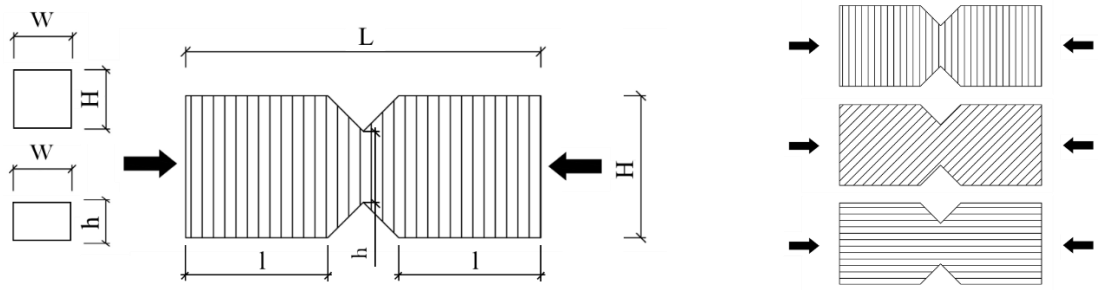

Fig. 8: Schematic of specimen types with different annual ring orientations used for the compression test: L – length of specimen, W – width of specimen, h – height at the notch, l – distance between support and edge-notch.

(Source: own illustration)

Tab. 7: Data of specimens used for the compression test

(Source: own illustration)

№	**L** (mm)	**W** (mm)	**h** (mm)	**α** (deg)	**Weight** (g)	**Latewood ratio** (%)	**Feed rate** (mm/min)	**dGR** (mm)
NY01	100.0	39.6	15.7	26.2	60.56	10.8	1.0	174.6
NY02	100.0	39.8	15.7	27.1	60.91	12.3	5.0	157.2
NY03	100.0	40.5	19.8	90.0	70.44	18.1	5.0	129.7
NY04	100.0	40.5	19.4	90.0	71.48	21.3	5.0	112.8
NY05	100.0	40.5	19.1	13.7	70.38	18.4	5.0	132.4
NY06	100.0	40.4	19.3	1.4	71.97	19.3	5.0	126.1
NY07	100.0	40.4	18.8	90.0	69.76	18.2	5.0	119.4
NY08	100.0	40.5	19.0	90.0	68.88	21.1	5.0	122.0
NY09	100.0	40.5	19.7	7.0	72.23	19.1	5.0	122.1

3.3.2 Experiment results

In examining the fracture of wood at the meso scale, no attempt is made to investigate the failure at lower levels of material structure, only the behavior under load. The measurement method is responsible for the nonlinear initial phase (Bodig 1965). There are always surface irregularities, especially in wood. The force applied is proportional to the size of the contact area, which may be smaller in the initial stage. In case of the tension test, also a minimal sliding in the clamping may occur at the start of the measurement (most striking example is HU2 in Fig. 9b).

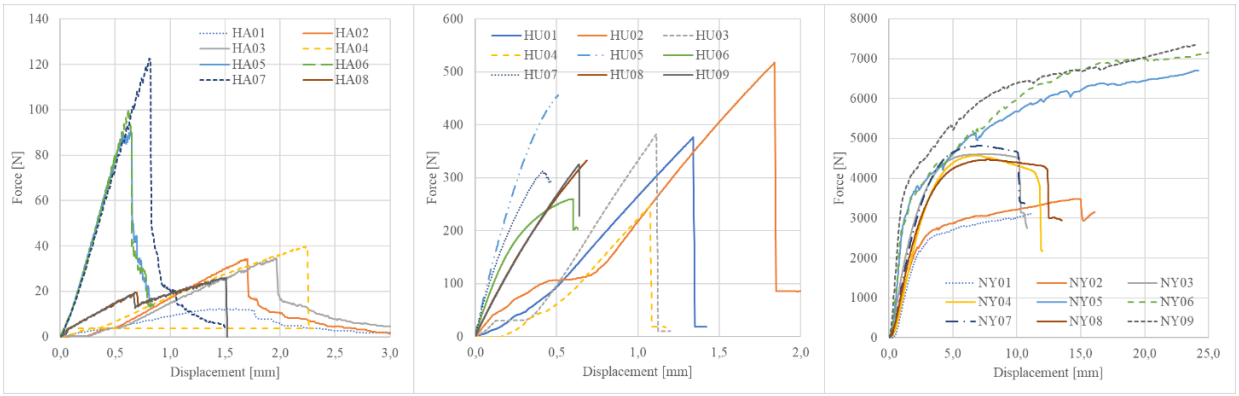

a.) b.) c.)

Fig. 9: Force-displacement diagrams of the tests:
a.) 3-point bending test;b.) Tension test; c.) compression test.

(Source: own illustration)

In the 3-point bending test 9 specimens were successfully tested (Tab. 8). During the measurement, the force-displacement diagram was documented, from which the flexure modulus can be calculated. With the video recording the failure mode as well as the crack path was captured. After the first crack appears, the resistance of the specimen drops rapidly. The weakened cross-section yields and the crack grows proportionally with the feed through

the specimen in the direction of the punch. Depending on the orientation of the annual rings, the typical failure is cross-grain tension (ring orientation perpendicular) and brash tension (ring orientation parallel), see Fig. 10.

a.)

b.)

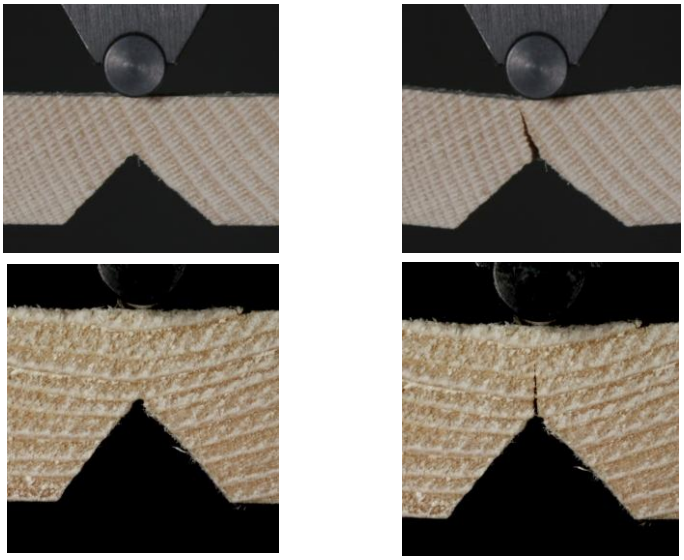

Fig. 10: 3-point bending test at the start of the test (left) and atmaximum load (right)
a.) Failure mode is cross-grain tension (specimen HA1);
b.) Failure mode is brash tension (specimen HU9).
(Source: own illustration)

Tab. 8: Experiment results of the 3-point bending test

(Source: own illustration)

№	**L** (mm)	**α** (deg)	**dGR** (mm)	**Ultimate force** (N)	**Ultimate deflection** (mm)	**Lin. flexure modulus** (MPa)	**Failure mode**
HA01	130.0	28.6	194.4	12.0	1.6	63.7	cross-grain tension
HA02	130.0	16.2	167.5	34.3	1.7	139.7	cross-grain tension
HA03	130.0	24.0	156.7	34.7	2.0	127.7	cross-grain tension
HA04	130.0	23.2	147.4	39.7	2.2	129.0	cross-grain tension
HA05	80.0	3.0	70.4	91.0	0.6	54.3	cross-grain tension
HA06	80.0	6.7	68.4	99.7	0.6	56.3	cross-grain tension
HA07	80.0	2.5	66.6	122.6	0.8	45.3	cross-grain tension
HA08	130.0	90.0	92.0	24.0	1.3	186.7	simple- and brash tension
HA09	130.0	90.0	94.3	26.0	1.5	189.4	brash tension
Average	***113.3***	***31.6***	***117.6***	***53.8***	***1.4***	***110.2***	
St. dev.	***23.6***	***32.5***	***46.2***	***37.4***	***0.5***	***53.8***	

In the tensile test 9 specimens were tested (Tab. 9). As for the bending test, the same parameters were documented. The crack grows through rapidly in the weakened cross-section. The 100 Hz frame rate of the camera is not sufficient for the crack growth to be resolved as for the 3-point bending test. Usually, 2-3 frames are recorded of the crack growth until complete

failure. Depending on the orientation of the annual rings, the typical failure is brittle tension (ring orientation perpendicular) and shearing along the annual ring (ring orientation parallel), see Fig. 11.

a.)

b.)

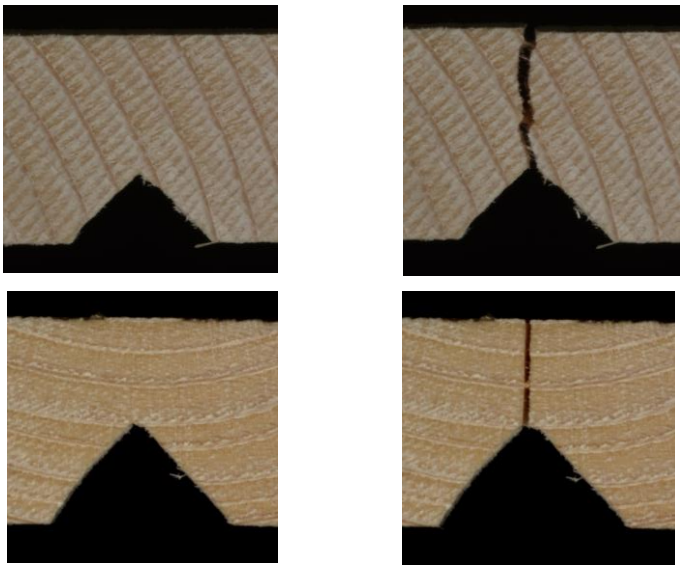

Fig. 11: Tension test at the start of the test (left) and at maximum load (right): a.) Failure mode is a combination of shearing along the annual ring and tension failure of earlywood (specimen HU3); b.) Failure mode is brittle tension (specimen HU8). (Source: own illustration)

Tab. 9: Experiment results of the tension test

(Source: own illustration)

№	**L** (mm)	**α** (deg)	**dGR** (mm)	**Ultimate force** (N)	**Ultimate elongation** (mm)	**Tension modulus** (MPa)	**Failure mode**
HU01	160.0	90.0	174.6	376.4	1.3	80.0	tension parallel to grain: brittle tension
HU02	160.0	90.0	157.2	517.5	1.8	83.9	tension parallel to grain: brittle tension
HU03	160.0	33.4	129.7	382.4	1.1	91.6	tension perpendicular to the grain: combination of shearing along the annual ring and tension failure of earlywood
HU04	80.0	22.4	112.8	247.0	1.1	38.4	tension perpendicular to the grain: shearing along the annual ring
HU05	80.0	3.9	132.4	455.4	0.5	284.7	tension perpendicular to the grain: shearing along the annual ring
HU06	80.0	9.3	126.1	259.4	0.6	197.9	tension perpendicular to the grain: shearing along the annual ring
HU07	80.0	11.8	119.4	313.2	0.4	251.8	tension perpendicular to the grain: shearing along the annual ring
HU08	160.0	90.0	122.0	332.4	0.7	225.0	tension parallel to grain: brittle tension
HU09	160.0	90.0	122.1	325.6	0.6	224.9	tension parallel to grain: brittle tension
Average	***124.4***	***49.0***	***122.1***	***356.6***	***0.9***	***164.2***	
St. dev.	***39.8***	***37.5***	***28.0***	***82.7***	***0.4***	***85.2***	

In the compression test 9 specimens were tested (Tab. 10). The documented parameters are the same, as in case of the other tests. Crack growth (in the macro range) is a slow process and occurs after extensive elastoplastic deformation. The force-displacement curves always show a bend after the compressive force increases slowly. When the specimen buckles laterally, the force that can be applied decreases, as for example in NY04, NY07, NY09. Depending on the orientation of the annual rings, the typical failure is the collapse of earlywood layers in the middle of the specimen combined with shearing along the side (ring orientation perpendicular) and crushing and splitting (ring orientation parallel), see Fig. 12.

a.)

b.)

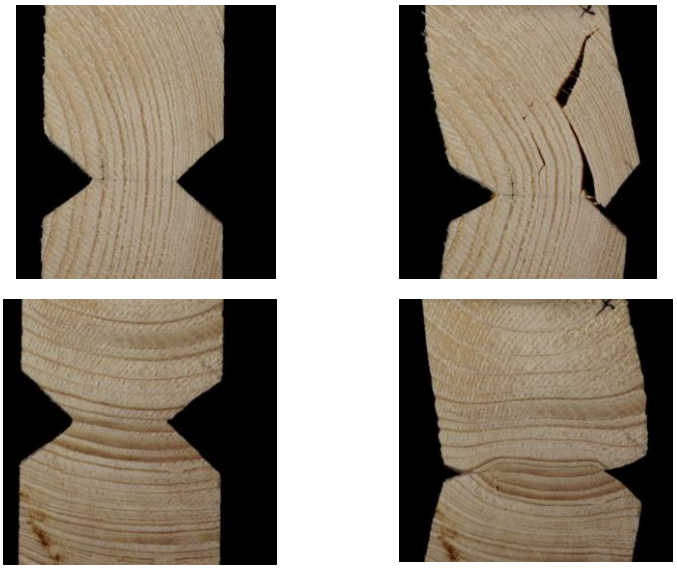

Fig. 12: Compression test at the start of the test (left) and at maximum load (right): a.) Failure mode is crushing and splitting (specimen NY3); b.) Failure mode is collapse of earlywood layers (specimen NY6).
(Source: own illustration)

Tab. 10: Experiment results of the compression test

(Source: own illustration)

№	**L** (mm)	**α** (deg)	**dGR** (mm)	**Ultimate force** (N)	**Ultimate elongation** (mm)	**Compression modulus** (MPa)	**Failure mode**
NY01	100.0	26.2	174.6	3128.0	11.3	78.2	compression perpendicular to grain: in the middle earlywood layers collapse, while on the side shearing along the annual ring
NY02	100.0	27.1	157.2	3484.0	14.8	97.5	compression perpendicular to grain: in the middle earlywood layers collapse, while on the side shearing along the annual ring
NY03	100.0	90.0	129.7	4610.0	8.0	128.9	compression parallel to the grain: crushing and splitting
NY04	100.0	90.0	112.8	4565.0	7.0	87.0	compression parallel to the grain: crushing and splitting
NY05	100.0	13.7	132.4	6705.0	24.2	196.2	compression perpendicular to grain: earlywood layers collapse
NY06	100.0	1.4	126.1	7417.5	28.6	209.8	compression perpendicular to grain: earlywood layers collapse
NY07	100.0	90.0	119.4	4810.0	7.4	111.4	compression parallel to the grain: crushing and splitting
NY08	100.0	90.0	122.0	4465.0	7.9	102.6	compression parallel to the grain: crushing and splitting
NY09	100.0	7.0	122.1	7357.5	24.0	271.4	compression perpendicular to grain: earlywood layers collapse
Average	***100.0***	***48.4***	***132.9***	***5171.3***	***14.8***	***142.6***	
St. dev.	***0.0***	***38.0***	***18.9***	***1509.6***	***8.1***	***63.3***	

3.3.3 Correlation of variables based on the measurement data

In the experiments, the specimens were subjected to 3-point bending-, tension- and compression tests. In each type of test, 9 specimens with different orientation and diameter of the annual rings at the edge-notch were investigated.

Based on the measurement results (Tab. 8, Tab. 9 and Tab. 10) the correlation between the variables can be calculated. Tab. 11 shows the correlation of the variables annual ring orientation (α), the diameter of the annual ring at the edge-notch (dGR), latewood ratio (LWr), ultimate force (F_u), ultimate elongation/deflection (u_u) and the calculated moduli (E_f , E_t , E_c). The correlation coefficient (r_{xy}) indicates the strength of the linear relationship between the variables:

$$r_{xy} = \frac{\sum(x_i - \overline{x})(y_i - \overline{y})}{\sqrt{\sum(x_i - \overline{x})^2 \sum(y_i - \overline{y})^2}} \; ; \; -1 < \; r_{xy} < 1 \qquad (34)$$

A negative value of r_{xy} means negative correlation, which means that the variables tend to have an inverse relationship. The value 0 means no correlation at all. A positive correlation means, that the variables tend to have a direct relationship.

Tab. 11: Correlation of the variables based on the measurement data

(Source: own illustration)

Test type	x: α y: F_u	x: α y: u_u	x: α y: $E_{f/t/c}$	x: LWr y: F_u	x: LWr y: u_u	x: LWr y: $E_{f/t/c}$	x: dGR y: F_u	x: dGR y: u_u	x: dGR y: $E_{f/t/c}$
3-p. bend. tests	-0,337	-0,685	0,755	-0,554	-0,619	0,446	-0,737	0,389	-0,941
tension test	0,311	0,517	-0,254	-0,244	-0,629	0,715	-0,378	-0,628	0,480
compr. test	-0,506	-0,900	-0,638	0,555	0,031	0,335	-0,542	0,008	-0,338

Strength of relationship	-0,1 to 0,1	-0,3 to -0,1 or 0,1 to 0,3	-0,5 to -0,3 or 0,3 to 0,5	-1,0 to -0,5 or 1,0 to 0,5
	very weak	weak	moderate	strong

From this we can conclude that based on the population data of the 3 tests considered, only one parameter pair, the latewood ratio versus the calculated moduli, influences the measurement results to almost the same extent. The other parameter pairs show different values and correlations. This means that the corresponding measurements are sensitive to changes in certain parameters. It can be clearly seen that in the compression test, the elongation in relation to the diameter of the annual rings at the edge-notch and to the latewood ratio has a correlation value close to zero, while for the bending test and tension test these parameter pairs have a high impact.

The annual ring orientation has a great influence on the load-bearing capacity and on the ultimate elongation/deflection. For the calculation of the correlation of F_u and u_u, the measurement values were normalized to eliminate the influence of the length of the specimens. In case of the 3-point bending test and compression test lower values of α lead to a higher ultimate force and ultimate elongation /deflection. Although these specimens with high α values (grains are parallel) have a higher calculated modulus of elasticity before the first sign of the material degradation, the crack in the edge notch occurs earlier in the bending tests and splitting occurs earlier in the compression tests, which affects the load-carrying capacity. In the compression tests, the collapse of the earlywood layers delays buckling because the edge notch zone is squeezed, and the specimen shortens.

A higher latewood ratio (LWr) does not necessarily lead to higher ultimate load F_u and calculated moduli (E_f, E_t , E_c), while these are more influenced by the orientation of the annual rings in the specimens. The largest positive influence of higher LWr values on the calculated moduli is seen in the compression tests. The LWr in the specimens tested is between 10.8% and 21.3% with an average of 15.7% and standard deviation of 3.0%.

The smaller diameter of the annual ring at the edge-notch (dGR) in most cases causes higher F_u values in the tested population, mainly because the crack has to propagate through

several earlywood and latewood layers instead of spreading in just one layer. In case of the 3-point bending tests the correlation between dGR and E_f shows, that smaller diameters lead to higher flexural modulus. This is only the case, because in the population the specimens with the annual ring orientations parallel to the grains ($\alpha = 90°$) have tendentially smaller dGR values. In this case, population size leads to a misinterpretation of the correlation between variables. In practice, as in the tension tests, a larger E modulus is obtained with a larger dGR and parallel to the grain orientation. In case of the compression test with parallel to the grain orientation splitting occurs earlier if the dGR values are higher. The diameter of the annual ring in the specimens tested are between 56.7 mm and 194.4 mm with an average of 131.1 mm and standard deviation of 28.9 mm.

4 Modeling method

4.1 Image recognition techniques in case of wood

The annual ring detection tools use the fact, that the brightness of the wood changes in the radial direction and ideally follows a ramp model. The brightness (or luminous brightness) of a digital image is a measure of relative intensity values across the pixel array after the image has been acquired (Balter 1993). The intensity refers to the magnitude of light energy reflected from or transmitted through the imaged object. Intensity for grayscale images is depicted by the grey level value at each pixel. In Fig. 13, the wood has grown from left to right, with the lighter earlywood forming in the spring and gradually changing to the darker latewood until it stopped growing at the end of the summer.

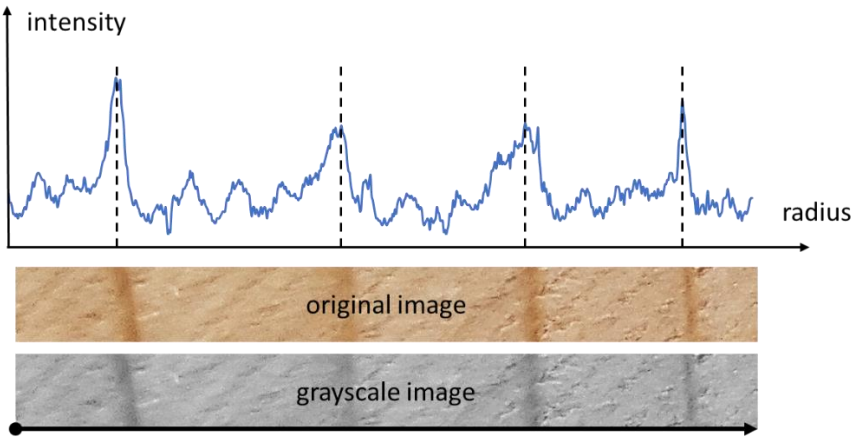

Fig. 13: Relation between density and brightness (image intensity) of the wood. (Source: own illustration)

A prerequisite for the detection of annual rings is the recognition of the end-grain cross section in the image. For this an object detection algorithm is required. Object detection is a computer vision technique for locating instances of objects in images or videos. Due to the drastic increase in computing power, the topic of computer vision has become quite popular. In the last decade, many researchers have published algorithms for object recognition, e.g., George (2013) with the Canny edge detection algorithm, or even complete tools such as Ruta et al. (2011) for traffic sign recognition or Pietikäinen & Okun (2001) and Cho & Jun (2016) for text recognition. The first step in object detection is to segment an image based on discontinuity detection technique (edge-based) or similarity detection technique (region-based) (Ramadevi et

al. 2010). Edge detection is one of the frequently used techniques and these algorithms use the Canny, Sobel, Scharr, Prewitt, or Roberts method (Anphy et al. 2014).

Cerda M. et al. (2007) proposed an automatic process which allows the detection of the latewood rings by using the Generalized Hough Transformation (GHT). According to their statement, the algorithm can detect 80% of the annual rings in their sample database. Habite T. et al. (2021) proposed a tool with a simple deep learning-based algorithm for automatic detection of surface annual rings and pith location along knot-free clear wood sections of Norway spruce board. There are also detection methods based on 3D X-ray CT images (Bulcke et al. 2014), but they are much more costly.

4.2 Recognition of annual rings from images

At the beginning, a modified version of the photoanalytical processing tool of (Polgár 2017) was used for the creation of the finite element models to analyze the color spectrum (HSV color model) and to detect the end-grain on the image. The main disadvantage of this tool is that the detection of end-grain and the separation of earlywood and latewood is based only on the HSV color spectrum. The subsequent spline fitting technique improves the contour of the result for end-grain detection but does not work as accurately for the annual ring separation.

In order to achieve better results, the recognition procedure was developed further. The detection of the annual rings on an image with the developed tool, consists of 5 phases, see Fig. 14. The tool separates earlywood and latewood, creating the contour between the earlywood and latewood layers. By filling the closed contours, surfaces can be generated for each earlywood and latewood annual ring layers. The generated surfaces were used to create the mesh for the finite element models.

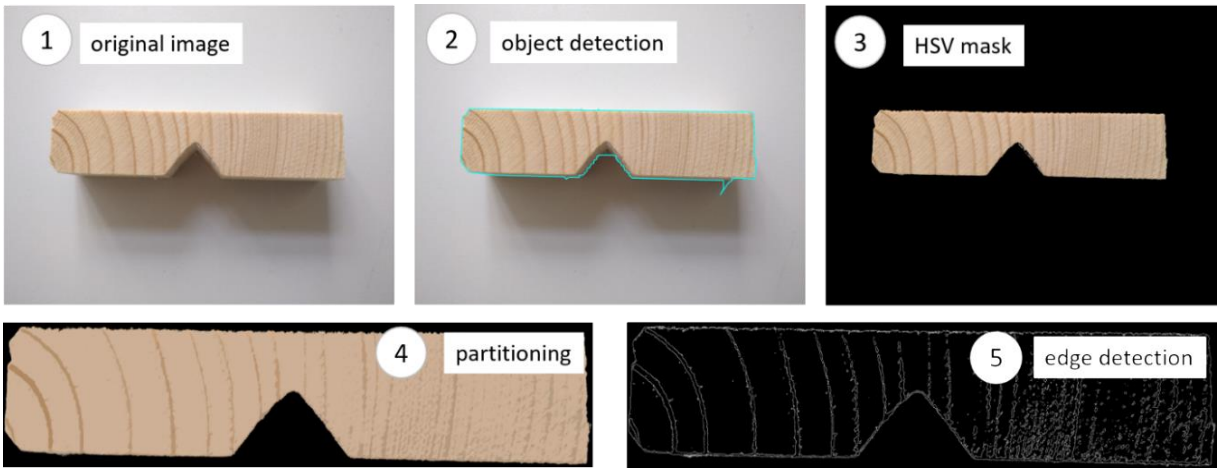

Fig. 14: Process of the annual ring detection: 1.) Original image with background; 2.) Mask background with object detection algorithm; 3.) Use an HSV mask to cut out all unnecessary details; 4.) Partitioning algorithm to separate earlywood and latewood; 5.) Edge detection to get the contours.

(Source: own illustration)

An edge is a place of rapid change in the image intensity function. To detect edges or objects, one must detect discontinuities in the image. This can be done by deriving the intensity of the image. The implemented algorithm uses the Canny edge detection, which is a multi-stage algorithm based on grayscale images developed by John F. Canny (1986). The Canny edge detection algorithm consists of 6 steps: conversion the image to grayscale, noise reduction (Gaussian blur), gradient calculation for detecting the edge intensity, non-maximum suppression to thin out the edges, double threshold to filter out non-relevant edges and finally edge tracking by hysteresis to link edges. A subsequent spline fitting technique improves the contour of the result. The tool tries to create edges with closed loops, which can be exported as a DXF (drawing interchange file format) file or as a SVG (scaleable vector graphics) file. For the detected edge loops, the surfaces can be calculated, and small surfaces can be filtered out if the user wishes.

The tool was developed in Python 3.x and consists of several functions, such as cropping the image for selecting the region of interest (ROI), taking a sample of a ROI and determine its HSV range, rescaling the image and generating output images for each stage of the recognition process, see Fig. 15. For some images, the tool also detects anomalies, so user intervention may be required. The recognition process works for both single images and high-resolution videos. To improve the performance of the annual ring detection tool, the specimens can be painted without affecting their physical properties. Some of the specimens were painted with a colorless nitro topcoat (Milesi LEC 040). The treatment does not affect the strength properties of the

specimens, but it does highlight the annual rings. The treatment makes it easier for the tool to distinguish between latewood and earlywood.

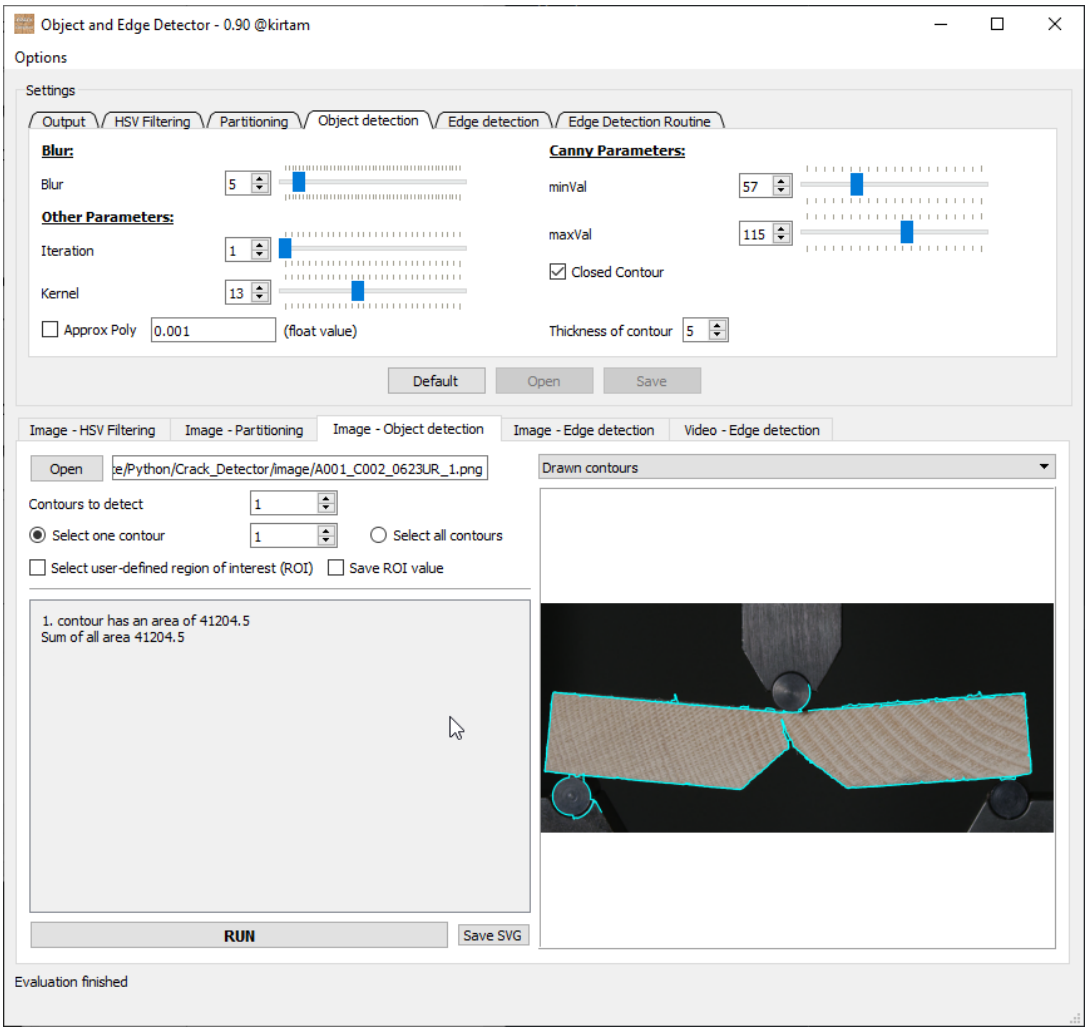

Fig. 15: Image of the developed tool, as an example the object detection menu is shown.

(Source: own illustration)

4.3 Modeling the annual ring pattern

The FE models (finite element models) were created based on photos of the end-grains of the specimens. For the analyses, a mesh was created for each individual Norway spruce timber specimen, taking into account the ratio and geomtery of earlywood and latewood in the bulk. There are three main steps in order to obtain a meshed model for the FE analysis (Fig. 16). As a first step, one must shoot a macro photo, so that all the details and pattern of the annual rings are well recognizable. After the photo was taken, the proprietary developed tool was used for analyzing the color spectrum and for detecting the end-grain on the picture. With the help of

the implemented features of the tool it is possible to separate earlywood and latewood. The result is the contour of each earlywood and latewood layer, respectively in a DXF (or SVG) file. Next, the 2-D surfaces are generated in FE preprocessor for each annual ring as shown in Fig. 16. The skewed surfaces can be stretched to achieve a the real (maybe a bit imperfect) rectangular shape used for the FE calculations. The final preprocessing step of the mesh creation is the extrusion of the obtained 2-D mesh to achieve the final 3-D mesh of the beam. In the end, the material properties are defined and the measurement setup is created in the FE-model in terms of boundary conditions, acting loads and contacts.

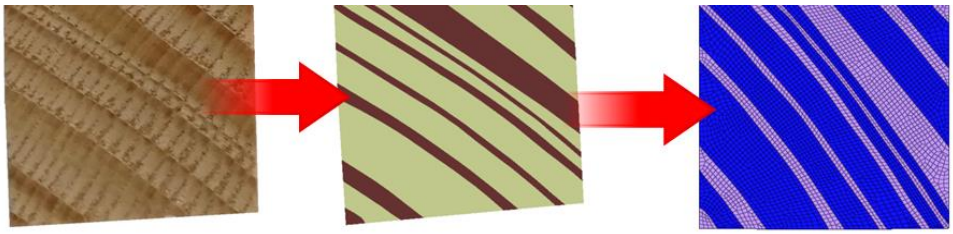

a.) b.) c.)

Fig. 16: Obtaining a FE-mesh from a picture of the end-grain: a.) Photo of the end-grain of the specimen; b.) Generated surfaces of earlywood and latewood; c.) Meshed surfaces of earlywood and latewood.

(Source: own illustration)

For the definition of orthotropic material properties, a local coordinate system is used with respect to the alignment of annual rings in the cross-section of each specimen. Wood properties are usually defined in a cylindrical (or polar) material coordinate system with the origin in the pith. In case the annual rings lie on a large radius, hence their alignment is approximately parallel to each other, a rectangular coordinate can be used (Fig. 17).

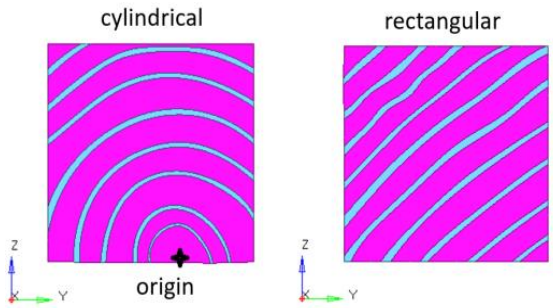

Fig. 17: Choice of local coordinate system depending on the alignment and size of the annual rings.

(Source: own illustration)

5 Linear-elastic simulation of timber beams considering the annual rings

5.1 Description of the linear-elastic FE models

In this research the linear-elastic FE models were only used to calculate structural deformation and stresses. Like mentioned before, the specimens are modeled with straight grain without any knots, holes or cracks. The created geometry is meshed with continuum elements first order (8-node brick, hexahedral) as depicted in Fig. 18. The models satisfy the disciplines of linear elastic solver for quasistatic analysis, in respect to proper mesh quality, non-follower loading, small displacements and linear elastic material properties. For the analysis only ”half” models are used to decrease computing time and because the conditions of symmetry are fulfilled, see Fig. 19.

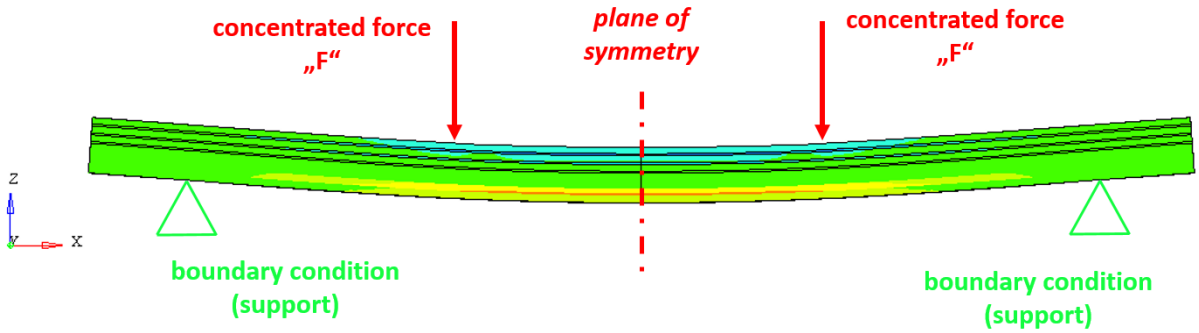

Fig. 18: Symmetry of the model and results.

(Source: own illustration)

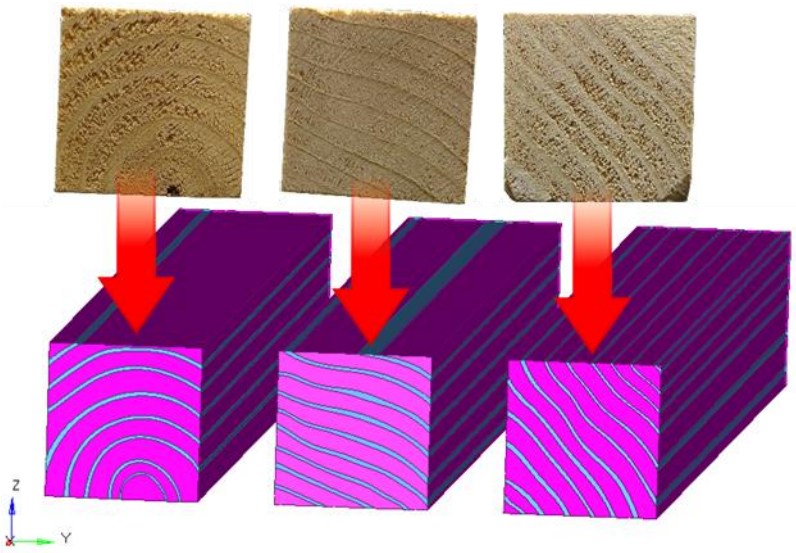

Fig. 19: Some of the FE models of the timber beams as example.

(Source: own illustration)

5.2 Material properties of earlywood and latewood

When investigating the material parameters, there was no opportunity to perform other tests besides the 4-point bending test (see chapter 3.2). However, specimens with different annual ring patterns were examined. According to the FE simulations conducted, in case of the 4-point bending tests, the deflection of the specimens depends on average 93% on the longitudinal modulus E_L. Based on the experiment results and the parameter study performed with FE, the other orthotropic material parameters of the bulk could be studied, but at this stage I also had to rely on the research results of other researchers. After obtaining the material properties of the bulk, the material properties for earlywood and latewood were calculated according to Hypothesis 2 using Eqs. 16-22.

For the FE analyzes the values in Tab. 12 were used, which are based on the studies by Qing and Mishnaevsky (2010), Fleischmann (2005), Nilsen (2015), Khokhar et al. (2010), Modén and Berglund (2008), Gibson and Ashby (1997), Nairn (2006) (2007) and the own experiments. In Tab. 12 not all of the values of earlywood and latewood are experimental results (like the Poisson's ratios), they are however reasonable values, which are consistent with the bulk properties. The values of Tab. 12 are considered for 45% volume ratio of latewood in the bulk. For the FE calculations, the densities of spruce timber had to be determined statistically. The density of the earlywood and latewood rings was determined by measuring finite small specimens. Based on the populations in Tab. 3 and Tab. 4, the earlywood has a density (ρ_{EW}) of 258 kg·m^{-3} and the latewood has a density (ρ_{LW}) of 984 kg·m^{-3}.

Tab. 12: Linear-elastic orthotropic material properties of earlywood and latewood used for the finite element simulations

(Source: own illustration)

Material constants	Symbol	Unit	Bulk	Earlywood (EW)	Latewood (LW)	Exponent
Density	$\rho_{EW/LW}$	kg·m^{-3}	-	258$^{(*)}$	984$^{(*)}$	-
Long. modulus	$E_{EW/LW,L}$	MPa	11286$^{(*)}$	4979.97	18993.37	1$^{(a)}$
Rad. modulus	$E_{EW/LW,R}$	MPa	960$^{(d)}$	576.35	5108.91	1.63$^{(b)}$
Tang. modulus	$E_{EW/LW,T}$	MPa	620$^{(d)}$	24.30	1348.13	3$^{(c)}$
Poisson's ratio LR	$\nu_{EW/LW,LR}$	-	0.041$^{(d)}$	0.041$^{(d)}$	0.041$^{(d)}$	-
Poisson's ratio LT	$\nu_{EW/LW,LT}$	-	0.033$^{(d)}$	0.033$^{(d)}$	0.033$^{(d)}$	-
Poisson's ratio RT	$\nu_{EW/LW,RT}$	-	0.35$^{(d)}$	0.350$^{(d)}$	0.350$^{(d)}$	-
Shear modulus LR	$G_{EW/LW,LR}$	MPa	580$^{(e)}$	387.43	1477.64	1$^{(b)}$
Shear modulus LT	$G_{EW/LW,LT}$	MPa	590$^{(e)}$	394.11	1503.12	1$^{(b)}$
Shear modulus RT	$G_{EW/LW,RT}$	MPa	80$^{(d)}$	44.65	2477.12	3$^{(a)}$

$^{(a)}$ Gibson and Ashby (1997), $^{(b)}$ Nairn (2006), $^{(c)}$ Modén and Berglund (2008), $^{(d)}$ Nairn (2007), $^{(e)}$ Nilsen (2015), $^{(*)}$ based on own experiments. The unlabeled values are the values calculated according to Hypothesis 2 using equations 16-22.

5.3 Comparison of the linear elastic finite element and experiment results

For the measurements, a few other parameters must be documented in addition to the force-deflection data. For example, the weight of the timber beam respective the photo of the end-grain cross-section. Based on these, parameters can be calculated to measure the validity of simplification assumptions and modeling.

According to the *Hypothesis 1* from the measured weight of the specimens, their average density can be obtained. These density values can be compared to the average density, which is calculated by using the assumptions and the annual ring ratio determined from the photos. According to the *Hypothesis 2* the ROM combined with the correlation among the orthotropic material properties and density of earlywood and latewood, the material properties of the Norway spruce can be obtained (Tab. 12). The measured deflections at a given load can be compared with the deflections calculated with the finite element models.

A qualitative comparison between experimental data and FE results demonstrates good agreement. An overview of all results is shown in Tab. 13 and Tab. 14 respectively. Modeling results were satisfying in terms of stiffness, deflection and as well in control parameters like; measured and calculated mass of the specimens. Clearly the greatest deflection for 4-point bending test for symmetrical models is measured in the middle of the beams. Depending on the cross-sections a torsional twist can occur, in that case the average deflection in the middle cross-section is calculated.

For the 20 x 20 specimens the density errors range between -15% and -33%. The deviation of the calculated density values is due to the inaccurate detection of the earlywood and latewood ratio in the end-grain. It seems that the ratio of latewood is generally underestimated by the photo analytic processing tool. In case of bending, the percentage errors range between 3% and 37%.

Tab. 13: Comparison of experiment and FE calculation results of the 20 x 20 x 400 specimens. (Source: own illustration)

Nº	Max		Weight (g)	LW ratio (%)	Average density		Error (%)	Deflection by 0.5 kN		Error (%)
	Deflection (mm)	Force (N)			Measured ($kg \cdot m^{-3}$)	Calculated ($kg \cdot m^{-3}$)		Measured (mm)	Calculated (mm)	
1	11.642	1.585	43.68	43.68	621.327	479.264	-29.64	2.89	3.75	22.96
2	9.766	1.523	36.51	36.51	507.668	435.886	-16.47	2.38	2.77	14.19
3	12.280	1.529	28.46	28.46	468.187	387.183	-20.92	2.75	3.33	17.39
4	12.876	1.619	48.63	48.63	621.079	509.212	-21.97	3.22	3.31	2.72
5	14.578	1.644	32.68	32.68	508.374	412.714	-23.18	3.05	3.75	18.75
6	17.423	1.727	29.61	29.61	523.546	394.141	-32.83	2.84	4.49	36.74
7	16.957	1.763	42.65	42.65	583.325	473.033	-23.32	2.93	3.61	18.92
8	12.616	1.543	44.69	44.69	559.937	485.375	-15.36	2.99	3.45	13.22
9	18.064	1.761	37.86	37.86	549.789	444.053	-23.81	3.31	4.10	19.22
10	12.804	1.625	39.74	39.74	570.512	455.427	-25.27	3.14	3.41	7.92
Average	13.901	1.632	38.45	38.45	551.374	441.585	-23.28	2.95	3.60	17.20
Std. dev.	2.754	0.092	6.70	6.70	50.187	34.403	5.30	0.27	0.47	9.10

For the 40 x 40 specimens the density errors are in the worst case between ± 10%. In case of bending, the percentage errors move on a slightly larger scale, in which case the values range between -9% and +16% percent. It can be stated that the 40 x 40 specimens generally lead to a better correlation of the measured and calculated values. For natural wood, EUROCODE 5 (EN 1995) requires a safety factor of at least 1.3, which is very optimistic. For this reason, the values within the 30% margin of error can be considered good.

Tab. 14: Comparison of experiment and FE calculation results of the 40 x 40 x 800 specimens. (Source: own illustration)

Nº	Max		Weight (g)	LW ratio (%)	Average density		Error (%)	Deflection by 0.5 kN		Error (%)
	Deflection (mm)	Force (N)			Measured ($kg \cdot m^{-3}$)	Calculated ($kg \cdot m^{-3}$)		Measured (mm)	Calculated (mm)	
1	11.560	3.167	460	16.27	341.510	313.417	-8.96	8.68	8.06	-7.69
2	12.064	3.733	417	21.21	314.776	343.330	8.32	7.56	7.54	-0.25
3	16.138	4.267	409	19.35	315.449	332.082	5.01	7.74	7.69	-0.63
4	10.605	3.250	418	21.52	311.372	345.186	9.80	7.99	7.63	-4.63
5	15.936	4.517	407	18.33	310.926	325.893	4.59	7.60	7.73	1.68
7	15.125	4.767	447	17.93	356.170	323.495	-10.10	6.64	7.88	15.74
8	10.431	2.933	402	16.07	314.699	312.216	-0.80	8.34	8.41	0.86
10	12.207	3.733	437	17.64	328.921	321.722	-2.24	7.70	8.10	4.89
11	13.025	3.900	414	22.37	329.317	350.338	6.00	7.86	7.25	-8.39
12	11.433	3.383	445	18.03	337.808	324.069	-4.24	7.88	7.87	-0.22
14	13.739	3.950	426	20.33	338.110	338.015	-0.03	8.35	7.65	-9.12
Average	12.933	3.782	425.6	19.00	327.187	329.978	0.67	7.85	7.80	-0.71
Std. dev.	2.156	0.608	20.0	2.23	15.801	13.518	6.70	0.56	0.33	7.10

Stress distributions in the beam cross-sections are also of interest. Because of the absence of earlywood-latewood transitions, there are sharp changes in stresses between the layers. No transition zone between earlywood and latewood is considered. It is clear, that for 4-

point bending tests the dominating stress is the longitudinal stress, see Fig. 20a. The highest longitudinal stress magnitudes are present in the latewood layers and they are about 4 times higher than the ones in the earlywood layer (compare the longitudinal moduli in Tab. 12).

The presence of shear stresses is almost not noticeable at this loadcase and their distribution strongly depends on the annual ring pattern. The shear stress distribution in some of the specimens is shown in Fig. 20b. It can be observed in the specimens that shear stresses in earlywood are rather constant in the entire cross-section, while in latewood there are some stress hot-spots. Shear stresses in the TL- and LR-plane tend to show higher values the in the RT-plane. The results of further FE models are not shown. In order to have a complete overview of all the relevant data, Tab. 13 and Tab. 14 were created.

a.)

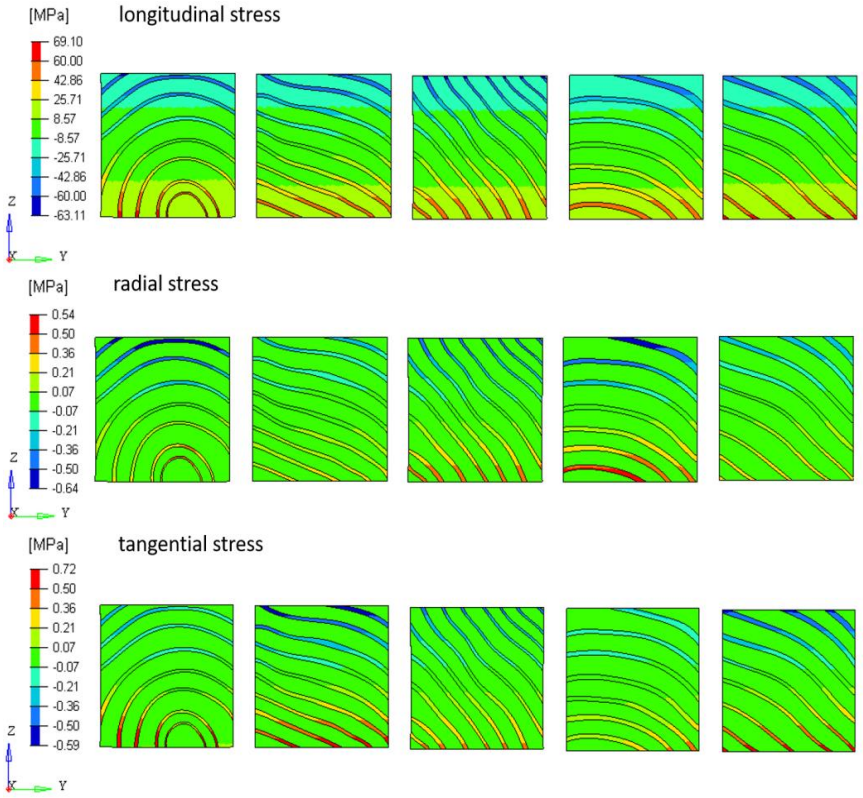

b.)

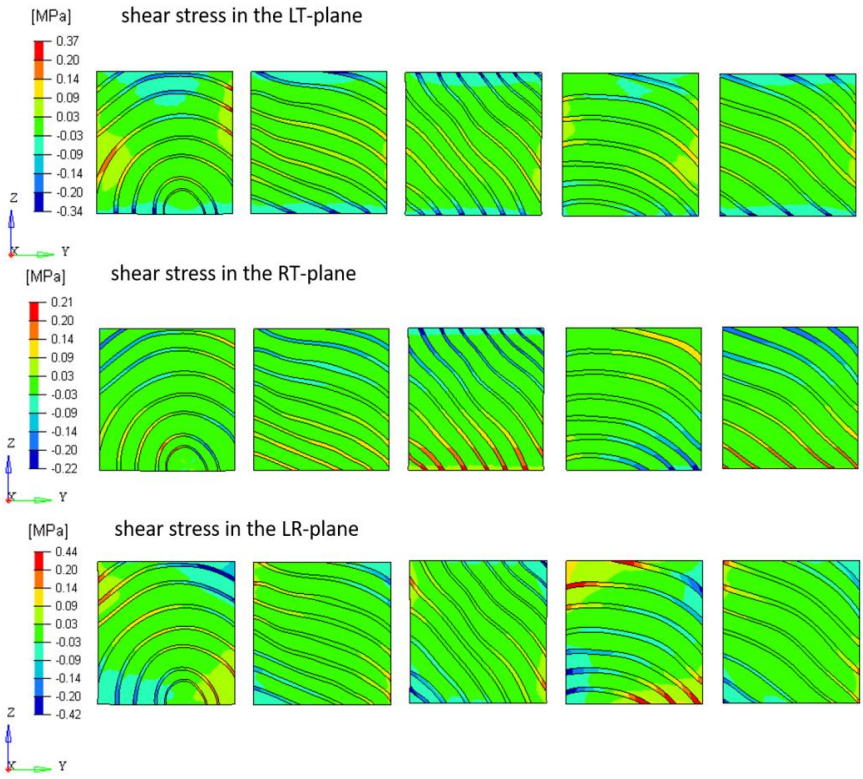

Fig. 20: Stresses in the 40 x 40 x 800 mm timber beams (under the loading F = 1250 N on the half model), middle section close-up view: a) normal stresses, b) shear stresses.

(Source: own illustration)

6 Linear elastic fracture mechanics

6.1 Brief overview of the theory of XFEM

The developement of the XFEM came a long way since its introduction by Belytschko & Black (1999) and Moës et al. (1999) based on the partition of unity proposed by Melenk & Babuska (1996). The XFEM allows the presence and propagation of cracks without the need for the mesh to match the crack path. Thus, XFEM is an excellent tool for the LEFM (linear elastic fracture mechanics) to simulate failure. It is more suitable for brittle fracture and can also be used when there is no initial crack.

The advantage of LEFM is that due to the linearity of the constitutive equations and because of the assumption of small strains, closed form solutions for stress and strain fields at a crack tip can be obtained (Brocks 2018). These assumptions do not apply for incremental plasticity, because the constitutive equations are non-linear, moreover, the current stress-strain state depends on the loading history. LEFM is suitable for problems with small-scale yielding, which means that the zone of plasticity is small compared to the crack size.

XFEM is able to achieve optimal convergence rates on structured meshes, where arbitrary discontinuities and singularities exist within the elements. There are two different types of discontinuities which should be considered: in case of a weak discontinuity the gradient has a jump and in case of a strong discontinuity the field quantity has a jump. Through the use of level-set method in ABAQUS (Dassault Systèmes 2019), the location of discontinuities with respect to the existing mesh is determined. A level-set function is a scalar function within the domain whose zero-level is interpreted as the discontinuity (Stolarska et al. 2001). The combination of XFEM with the level-set method allows the representation of an arbitrary 3D crack, where the crack is completely described by nodal data. XFEM allows the presence of discontinuities in an element by enriching the degrees of freedom with special displacement functions, shown in Eq. 35. The displacement function consists of a standard FE (finite element) approximation part $\boldsymbol{u}^{FE}$ and an enrichment $\boldsymbol{u}^{enr}$ (Moës et al. 1999):

$$\boldsymbol{u} = \boldsymbol{u}^{FE} + \boldsymbol{u}^{enr} = \sum_{I=1}^{N} N_I(x) \cdot \left[\boldsymbol{u}_I + H(x) \cdot \boldsymbol{a}_I + \sum_{\alpha=1}^{4} F_\alpha(x) \cdot \boldsymbol{b}_I^\alpha \right] \tag{35}$$

where $\boldsymbol{u}$ displacement vector, $N_I(x)$ shape functions, $\boldsymbol{u}_I$ nodal displacement vectors, $H(x)$ jump function, $\boldsymbol{a}_I$ nodal enriched degree of freedom vector, $F_\alpha(x)$ asymptotic crack-tip

function, $\boldsymbol{b}_I^{\alpha}$ nodal enriched degree of freedom vector. The terms in Eq. 35 have the following function (Moës et al. 1999):

1. term: $N_I(x) \cdot \boldsymbol{u}_I$, applies to all nodes in the model;
2. term: $N_I(x) \cdot H(x) \cdot \boldsymbol{a}_I$, applies to nodes whose shape function support is cut by the crack interior (see Fig. 21);
3. term: $N_I(x) \cdot [\sum_{\alpha=1}^{4} F_\alpha(x) \cdot \boldsymbol{b}_I^{\alpha}]$, applies to nodes whose shape function support is cut by the crack tip (see Fig. 21).

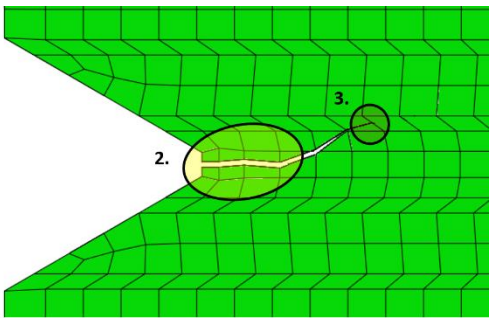

Fig. 21: Displacement vector of enriched elements

(Source: own illustration)

For this research the XFEM based cohesive segments method is used to simulate the crack initiation and propagation, where only the displacement jump across a cracked element is considered. For propagation cracks the third term in the Eq. 1 is neglected, therefore the near-tip singularity is not considered. The crack must propagate over an entire element at once to avoid consideration of the stress singularity.

In order to represent the discontinuity of the crack, phantom nodes are introduced (Song et al. 2006). The phantom nodes are overlaid on the 4 original ones and they stay connected to each other while the element is intact. The element intersected by a crack, divides into two parts. Both parts consist of a combination of real and phantom nodes depending on the orientation of the crack.

However, according to the ABAQUS User Manual (Dassault Systèmes 2019), there are limitations to the enriched function. Important limitations are that an enriched element cannot be intersected by more than one crack and that the crack is not allowed to turn more than 90° in one increment during an analysis. Also, some techniques are not supported, like adaptive remeshing and import analysis or elements like composite solid elements.

6.2 Damage Initiation

The damage initiation is the point at which material properties are first affected. In fracture mechanics of solids, three pure modes of crack propagation are considered (Janssen et al., 2004):

- mode I: tensile mode, where crack surfaces move directly apart;
- mode II: sliding (in-plane shear mode), where crack surfaces slide across one another in the direction perpendicular to the crack;
- mode III: tearing (antiplane shear mode), where the crack surfaces move parallel to the crack.

In addition, there is the so called mixed-mode fracture, which involves a combination of two to three of the modes.

The failure prediction of wood is a complex issue. Many researchers published different approaches as a failure criterion for wood, like Le-Ngoc & Mc-Callion (1997), Kyziol (2010), Sandhaas & van de Kuilen (2013), De Megistris & Salmén (2015) or Füssl et al. (2016), but there is no general agreement for a best fit. Guindos (2014) compared several failure criteria, i.e., Tsai-Hill, Tsai-Azzi, Norris, extended Yamada-Sun, Hoffmann, Hashin and Tsai-Wu, while varying the element size of the FE-model. Guindos considered a transversely isotropic material property and established Tsai-Hill as the best criterion for failure prediction. T. Akter & K. Bader (2020) compared Hill's and Hoffman's failure criteria using experimental data.

The Tsai-Hill (Tsai 1968) criterion uses the average strength and it does not take into account the differences between tensile and compressive strength. A more advanced version of the Tsai-Hill criterion is the Hoffman criterion (Hoffman 1967). It distinguishes tension and compression, but according to the study of Guindos (2014), it does not always lead to better results. The Hashin criterion (Hashin & Rotem 1973) allows the identification of parallel-perpendicular and tensile-compressive failure. This criterion is used for predicting various failure modes, such as fiber breakage in tension, fiber buckling in compression, matrix cracking and debonding. Hashin and Rotem proposed a criterion for plane stress state (Hashin & Rotem 1973) and few years later the criterion was also extended for 3-D stress state (Hashin & Rotem 1980). The criterion of Hashin does not always fit the experimental results in the case of matrix compression well (Pinho et al. 2005). The proposed quadratic failure criteria mean, that the failure plane of the matrix mode is the maximum transverse shear plane. In their own research report, they note that this fact seems unacceptable in general.

The mode I failure is considered to major cause for engineering failure (P. C. Conrad et al. 2003). The wood failure has often a significant mode II component and according to P. C.

Conrad et al. (2003) the majority of the researchers found it difficult to obtain values or relations for pure mode II failure. The reason for this is the low fracture toughness in mode I parallel to the grain. Ehart et al. (1999) found that fracture energy values were significantly higher for mode III than for Mode I. Therefore, only mode I fracture toughness is considered in this research.

The studies of other researchers show, that none of the failure criteria could predict a full failure envelope. The best suited criteria in one stress state can lead to the worst prediction in another stress-state. One of the first criteria for wood was defined by Norris (1962). Based on the fact, that the classical theory of plasticity is generally based on single-surface failure criteria that are not able to identify single failure modes, he postulated 3 equations.

Tab. 15: Description of the material constants for the failure criteria (Source: own illustration)

variable	description
$f_{t,R}$	tensile failure stress in radial direction
$f_{c,R}$	compressive failure stress in radial direction
$f_{t,T}$	tensile failure stress in tangential direction
$f_{c,R}$	compressive failure stress in tangential direction
$f_{t,L}$	tensile failure stress in longitudinal direction
$f_{c,L}$	compressive failure stress in longitudinal direction
$f_{s,L}$	failure shear stress in longitudinal direction
$f_{s,Q}$	failure shear stress in transverse direction

Based on the research results of T. Akter & K. Bader (2020), Luimes et al. (2018) and Sandhaas & van de Kuilen (2013), in this research 6 failure criteria are considered for clear wood (Eq. 36-41), taking into account the following damage initiation mechanisms: tension and compression in the 3 main directions. In contrast to the aforementioned studies, these failure criteria are considered separately for the earlywood and latewood layers. Sandhaas & van de Kuilen (2013) also suggested pure shear failure modes, but these criteria seem to be obsolete, since the same shear components are also considered in the tensile failure mode in the direction perpendicular to the grain. For each damage mode a normal vector to the crack surface $\overline{n}$ is assigned. Each wood species has its own fracture characteristic. In case of Norway spruce, the direction of the failure vectors was determined from the experiments conducted within the

framework of this doctoral dissertation. After a series of parametric studies, it was found that there is a correlation between the direction of crack growth and the orientation of principal stresses in the finite element reached by the crack tip.

Hypothesis 3 (Király 2021) (Király et al. 2023c): With the presented failure criteria it is possible to describe the damage processes of Norway spruce in case of brittle failure:

- Damage initiation mode 1: Tensile failure mode in parallel-to-grain direction if $\sigma_{LL} \geq 0$. It is a maximum stress criterion:

$$\frac{\sigma_{LL}}{f_{t,L}} = 1 \tag{36}$$

The normal of failure vector is perpendicular to the maximum principal stress.

- Damage initiation mode 2 and 3: Tensile failure mode in perpendicular to- grain direction if $\sigma_{RR} \geq 0$, respectively $\sigma_{TT} \geq 0$. The failure mode is caused by tensile stresses σ_{RR}, respectively σ_{TT} and shear stresses σ_{TL}, respectively σ_{RL} as well as rolling shear stress σ_{RT}. They are a quadratic criteria:

$$\left(\frac{\sigma_{RR}}{f_{t,R}}\right)^2 + \left(\frac{\sigma_{RT}}{f_{s,Q}}\right)^2 + \left(\frac{\sigma_{TL}}{f_{s,L}}\right)^2 = 1 \tag{37}$$

$$\left(\frac{\sigma_{TT}}{f_{t,T}}\right)^2 + \left(\frac{\sigma_{RT}}{f_{s,Q}}\right)^2 + \left(\frac{\sigma_{RL}}{f_{s,L}}\right)^2 = 1 \tag{38}$$

The normal of failure vector is perpendicular to the maximum principal stress.

- Damage initiation mode 4, 5 and 6: Compressive failure mode in parallel-to-grain direction if $\sigma_{LL} < 0$ and compressive failure mode in perpendicular-to-grain direction if $\sigma_{RR} < 0$, respectively $\sigma_{TT} < 0$. It is assumed that other stress components do not influence the tension strength (Sandhaas & van de Kuilen 2013). They are a maximum stress criteria:

$$if\, \sigma_{LL} < 0 \qquad \frac{\sigma_{LL}}{f_{c,L}} = 1 \tag{39}$$

$$if\, \sigma_{RR} < 0 \qquad \frac{\sigma_{RR}}{f_{c,R}} = 1 \tag{40}$$

$$if\, \sigma_{TT} < 0 \qquad \frac{\sigma_{TT}}{f_{c,T}} = 1 \tag{41}$$

In case of σ_{LL} the normal vector is parallel and in case of σ_{RR} and σ_{TT}it is defined perpendicular to the minimal principal stress.

When at least one of the failure criteria is met, the damage initiation is triggered. The criterion that reaches the critical value earliest is responsible for the onset of failure. The list of material constants for the failure criteria is given in Tab. 15.

6.3 Damage Evolution

The process of degradation begins when the stresses satisfy at least one of the defined crack initiation criteria, shown in Eqs. 36-41. The criterion that has the highest value at the given timepoint is responsible for the failure. The damage evolution defines the post damage-initiation material behavior and describes the rate of degradation of the material stiffness. The damage evolution law can be specified in terms of fracture energy (per unit area) or equivalent plastic displacement (Le-Ngoc & McCallion 1997). Stress fields in the vicinity of a crack tip can be characterized by a parameter, which is called the stress intensity factor and it is denoted by K_{IC} for the crack opening mode I. For an elastic and isotropic material Irwin (1957) derived the relationship between the stress intensity factor K_{IC} and the strain energy release rate G_f. The equation for pure mode I is the following:

$$G_f = \frac{(K_{IC})^2}{E} \tag{42}$$

Later on Sih et al. (1965) defined the relationship between K_{IC} and G_f for anisotropic materials. However, the simulations yielded more accurate results, when Eq. 42 was used in conjunction with the defined damage initiation criteria:

$$G_{f,LL} = \frac{({K_{IC}}^a)^2}{E_{LL}} \tag{43}$$

$$G_{f,RR} = \frac{({K_{IC}}^n)^2}{E_{LL}} \tag{44}$$

$$G_{f,TT} = \frac{({K_{IC}}^n)^2}{E_{TT}} \tag{45}$$

Although fracture toughness has been measured for a wide range of species, there is no standard method for determining fracture toughness in any mode. The fracture toughness of wood increases with increasing density and relationships between density and K_{IC} can be postulated (Ashby et al. 1985):

$${K_{IC}}^n = 20 \cdot \left(\frac{\rho}{\rho_s}\right)^2 MPa \cdot \sqrt{m} \tag{46}$$

$${K_{IC}}^a = 1.81 \cdot \left(\frac{\rho}{\rho_s}\right)^2 MPa \cdot \sqrt{m} \tag{47}$$

where $K_{IC}{}^{n}$ is the Mode I fracture toughness normal to the grain, $K_{IC}{}^{a}$ is the Mode I fracture toughness along the grain, ρ is the wood density and ρ_s is the density of the cell wall material.

6.4 Material properties and degradation due to mechanical stress of Norway spruce

The material degradation can be initiated by external influences. Such influences can be: heat, moisture, chemicals, fungi, bacteria, UV-light or, as in this research case, mechanical stress. Currently there are no pre-selectable wood material models in ABAQUS (Dassault Systèmes 2019) for FEM analyses considering material degradation due to mechanical stress, but there is a possibility to create user defined ones. ABAQUS uses several subroutines programmed in FORTRAN language to allow the user to define his own material degradation model. In my case, it was necessary to use the UDMGINI subroutine to implement the damage initiation criteria explained in chapter 6.3. User subroutines combined with engineering know-how provide a really powerful tool for analysis. They are interfaces, which allow to increase the functionality of ABAQUS.

The first step is to define the orthotropic material model for the earlywood and latewood separately. This is done with the values of Tab. 12, which are the engineering constants associated with the material's principal directions. The method for determining the orthotropic material properties of earlywood and latewood, and the relationship between the density and strength of Norway spruce was determined in a previous research, see chapter 5.2.

Next, the user-defined damage initiation criteria must be implemented. Each damage initiation mechanism is represented by a fracture criterion f_i (see Eqs. 36-41) and its associated normal direction to the crack plane. Crack initiation refers to the beginning of degradation of the cohesive response at an enriched element. Although there are 6 damage initiation mechanisms defined, the actual damage initiation for an enriched element is determined by the most severe damage initiation mechanism:

$$f = \max(f_1, f_2, \dots f_6) \tag{48}$$

Damage is initiated when f, as defined in the Eq. 48, reaches the critical value of 1.0. An additional crack is introduced or the crack length of an existing crack is extended after an equilibrium increment when the fracture criterion, f, reaches the critical value within a given tolerance (by default 0.05) (Dassault Systèmes 2019). Empirically, the best results were obtained with a tolerance of 0.01 without drastically increasing the simulation time.

For the complete description of the damage process, the damage evolution must be defined in addition to the user-defined damage initiation criteria. It is possible to define a separate damage evolution law for each damage initiation criterion. Therefore, each

combination of a damage initiation criterion with a corresponding damage evolution law is referred to as a failure mechanism. Damage is accumulated for only one failure mechanism per element, the mechanism whose damage initiation criterion was reached first in the increment. Deleting elements is possible in conjunction with XFEM, but it is not necessary because the XFEM elements split and the crack propagates.

Tab. 16: Fracture toughness of Norway spruce considering the density of early- and latewood

(Source: own illustration)

variable	**value [$MPa \cdot \sqrt{m}$]**	
	EW	**LW**
$K_{IC,LR}$ $K_{IC,LT}$	1.504	11.181
$K_{IC,RL}$ $K_{IC,TL}$ $K_{IC,RT}$ $K_{IC,TR}$	0,136	1,012

The Eqs. 46-47 and the density of the cell wall material can be used to calculate the fracture toughness of the earlywood and latewood, see Tab. 16. The mean mass density of the cell wall material of spruce timber is estimated at 1450 kg/m3 (Füssl et al. 2016).

Tab. 17: Energy release rates of Norway spruce for early- and latewood

(Source: own illustration)

variable	**value [N/mm]**	
	EW	**LW**
$G_{f,L}$	0.452	6.582
$G_{f,R}$	0.032	0.200
$G_{f,T}$	0.759	0.759

In ABAQUS one can specify the fracture energy per unit area, G_f , to be dissipated during the damage process directly. If G_f is specified as 0, immediate failure would occur, which can lead

to severe convergence issues. The values of G_f in table 4 can be obtained by using the Eqs. 43-45, the material properties of earlywood and latewood defined in Tab. 12 and the K_{IC}values in Tab. 17.

6.5 Description of the FE models for the XFEM calculations

The FE models were created in a mesh-based preprocessor (*Altair Hypermesh*) and calculated using the implicit static solver of ABAQUS (Dassault Systèmes 2019). The specimens were meshed with first order continuum elements C3D8I (8-node brick, hexahedral) as depicted in Fig. 22. In the area where the failure is expected, enriched finite elements are used. After the calculations, the results were carefully checked and it was ensured that the highest stresses, therefore the starting point of failure was certainly in the selected area. Nevertheless, the amount of enriched elements must be chosen reasonably in order to reduce the computation time. The stamps and clamps were meshed with R3D4 type rigid elements (4-node rigid shell) without thickness.

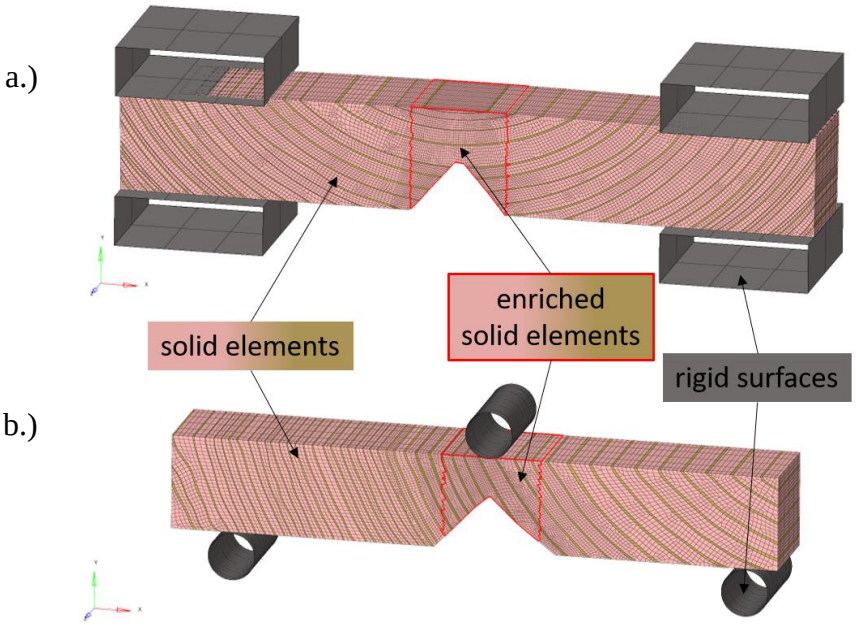

Fig. 22: Used element types of the FE models:
a.) Tensile test; b.) 3-point bending test.
(Source: own illustration)

The interaction between specimen and stamps or clamps is established by small-sliding contact with friction. The defined contact surfaces are shown in Fig. 23. The defined contact interaction of cracked element surfaces is also based on the small-sliding formulation. In this formulation,

the contact surfaces can undergo only a minor sliding relative to each other, but rotation of the bodies is permitted. Only static friction is considered in the simulations. Friction values for wood are given in scientific literature as 0.3-0.5 for dry and smooth wood against hard smooth surfaces, i.e. stamps and clamps (Deta et al. 2019). The range of friction values for wood-on-wood is 0.25-0.55. Therefore, the general static friction coefficient was assumed to be 0.4 in the simulations.

a.)

b.)

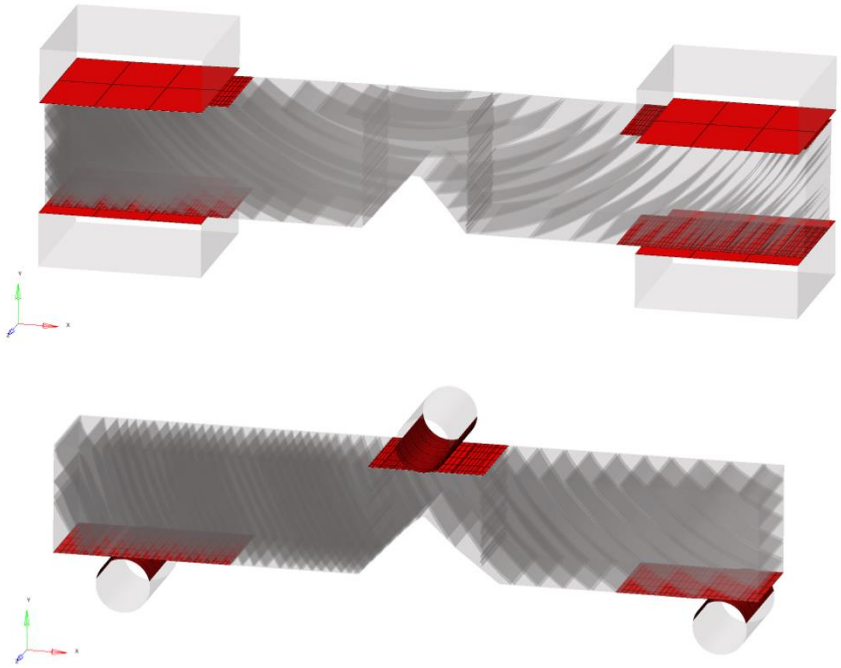

Fig. 23: Contact surfaces of the FE models: a.) Tensile test; b.) 3-point bending test. (Source: own illustration)

Fig. 24 shows the boundary conditions for the tensile and 3-point bending tests. In the tensile tests, the clamps are fixed in all directions on one side, while on the other side displacement is only permitted in the x-direction. In the 3-point bending tests, the stamps on the bottom are fixed in all directions, but rotation about the z-axis is allowed, and the top stamp is also fixed, but displacement in the y-direction is permitted. The selected boundary conditions accurately represent reality.

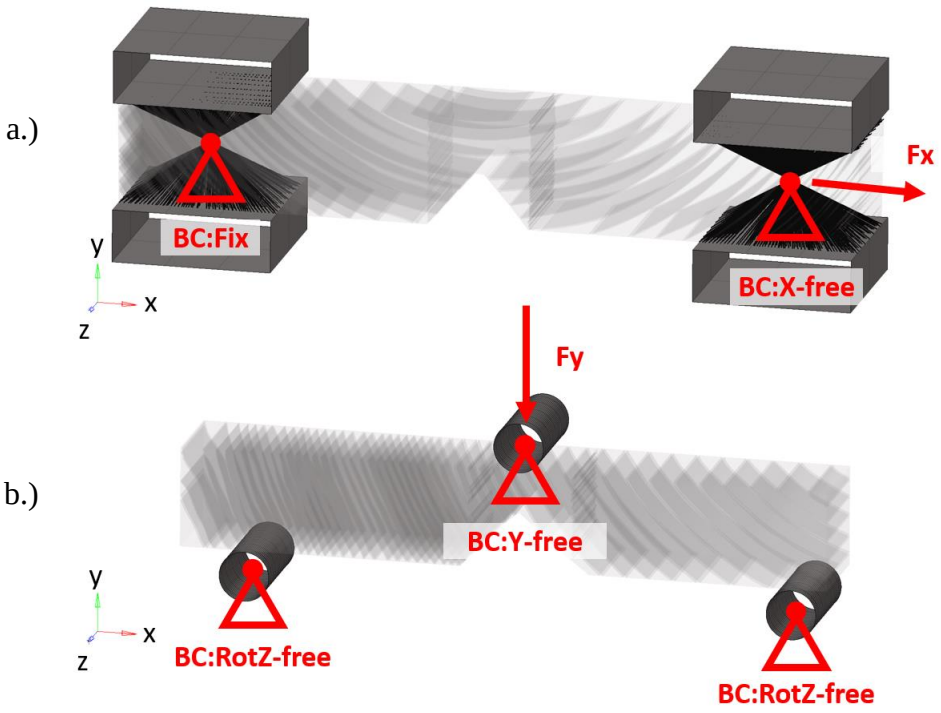

Fig. 24: Boundary conditions of the FE models: a.) Tensile test; b.) 3-point bending test (Source: own illustration)

6.6 Calibration of the material model

The predictive capabilities of the material model strongly depend on their calibration. As presented in chapter 3.3, tests such as 3-point bending tests, tensile and compression tests were conducted until failure. In each type of test 9 samples with different annual ring orientation were tested. The experiments were recorded with a high-resolution high-speed camera (Red Dragon 5K sensor and Samyang 3.1/100 mm optics), where the failure mode and the crack path are clearly visible. The test results were evaluated afterwards and the results were reproduced with FE models. Subsequently, linear-elastic FEM calculations were performed, documenting the stress tensors of the finite elements in the area of the edge-notch, as well as the displacement and reaction force of the stamp or the clamp. For the linear calculations, an optimization loop was performed in which the origin of the cylindrical coordinate system was varied so that the stiffness of the specimen in the FE model matched the calculated stiffness of the measurement with an error less than 5%. The algorithm was allowed a maximum displacement of the origo of 10% of the radius at the tip of the edge-notch of the specimen, like depicted on Fig. 25.

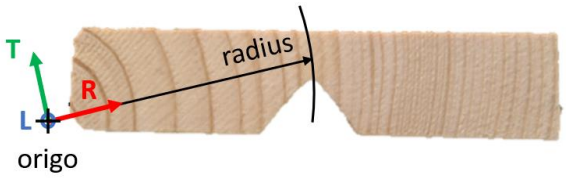

Fig. 25: Position of the cylindrical coordinate system and radius at the tip of the edge-notch.

(Source: own illustration)

Another optimization loop, a parameter fitting, was used to determine the failure stresses of the Norway spruce. The stresses obtained were used to calculate the utilization of each damage initiation mode (Eqs. 36-41) for all finite elements in the area of the edge-notch. The fracture stresses determined by Füssl et al. (2016) were used as initial values for the optimization. The goal of the optimization was to find the failure stresses at which the correct damage initiation criterion is activated at the correct location for all the specimens. The result of the optimization is shown in Tab. 18. These failure stresses were used for the further XFEM calculations.

Tab. 18: Failure Stress values of Norway spruce

(Source: own illustration)

variable	**value [N/mm]**	
	EW	**LW**
$f_{t,R}$	1.15	3.50
$f_{c,R}$	-1.15	-3.50
$f_{t,T}$	4.30	12.00
$f_{c,T}$	-4.30	-12.00
$f_{t,L}$	60.00	126.00
$f_{c,L}$	-35.40	-58.00
$f_{s,L}$	3.40	6.50
$f_{s,Q}$	3.40	6.50

In the tests performed, the influence of radial, tangential and longitudinal failure stresses were the greatest. The values of the shear failure stresses have a relatively small influence on the utilization, but can make a difference which damage initiation criterion is activated.

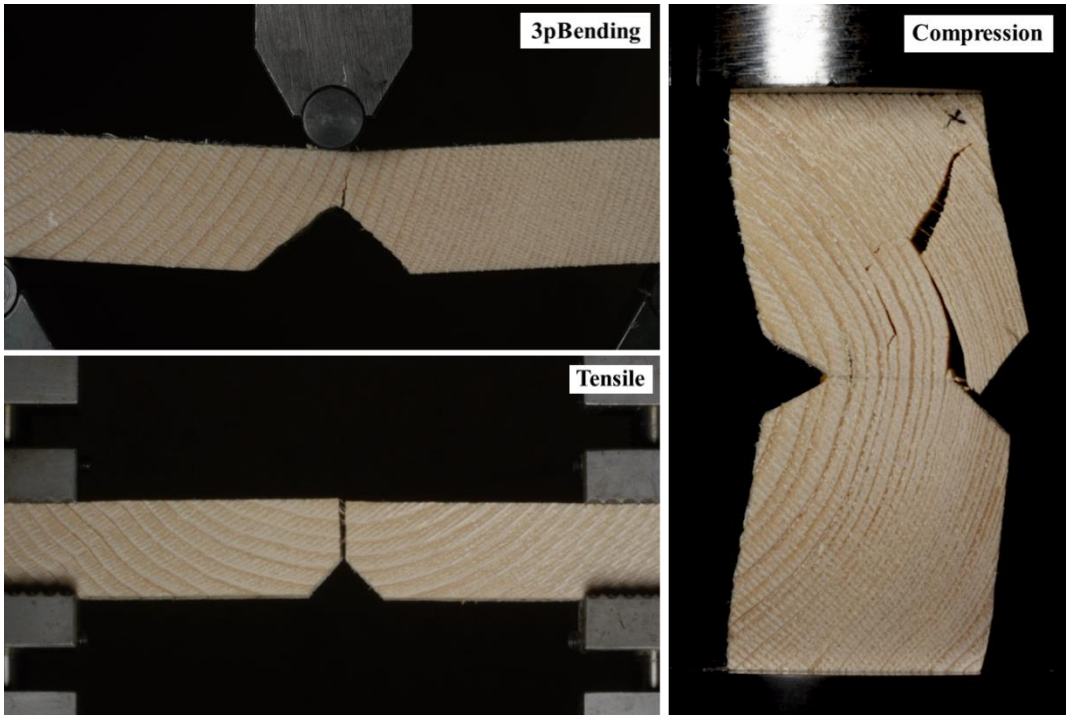

Fig. 26: Example of the tests: 3-point bending, tension and compression.
(Source: own illustration)

The specimens of the 3-point bending tests and the tensile tests fail dominantly with brittle fracture. The failure mode of these tests can be reproduced by the means of XFEM. However, in the compression test, a horizontal plateau is observed in the force-displacement curve, indicating a large elastoplastic deformation. For this reason, its failure behavior of Norway spruce cannot be adequately investigated by linear fracture mechanics. Examples of the 3 types of tests are shown in Fig. 26.

6.7 Comparison of the XFEM and experiment results

After the 3 types of tests with 9 specimens each, additional test specimens were selected and tested. XFEM calculations were performed for these further specimens using the material values from Tab. 12 and Tab. 18. The implemented FORTRAN subroutine differentiates between the acting most critical damage criteria in the enriched finite elements, see Fig. 27. From the results, it can be seen that the types of damage at the crack tip sometimes change from one element to another during deterioration. The criteria are recalculated for each integration point of each element at each iteration, until f does not reach 1.0. It may happen that from one increment to the next another criterion becomes more critical after a crack has occurred and the system does not give a linear response. The damage criteria are stored as solution dependent

variables. Variable number 1 is the damage initiation mode 1 and so on, see the list of modes in Tab. 19.

Tab. 19: Naming convention and mode ID of the damage initiation criteria in the implemented FORTRAN subroutine

(Source: own illustration)

variable	eq.	damage mode	description
SDV_RFTL	Eq. 36	1	tensile failure mode parallel-to-grain in longitudinal direction
SDV_RFTR	Eq. 37	2	tensile failure mode perpendicular-to grain in radial direction
SDV_RFTT	Eq. 38	3	tensile failure mode perpendicular-to grain in tangential direction
SDV_RFCL	Eq. 39	4	compressive failure mode parallel-to-grain in longitudinal direction
SDV_RFCR	Eq. 40	5	compressive failure mode perpendicular to-grain in radial direction
SDV_RFCT	Eq. 41	6	compressive failure mode perpendicular to-grain in tangential direction

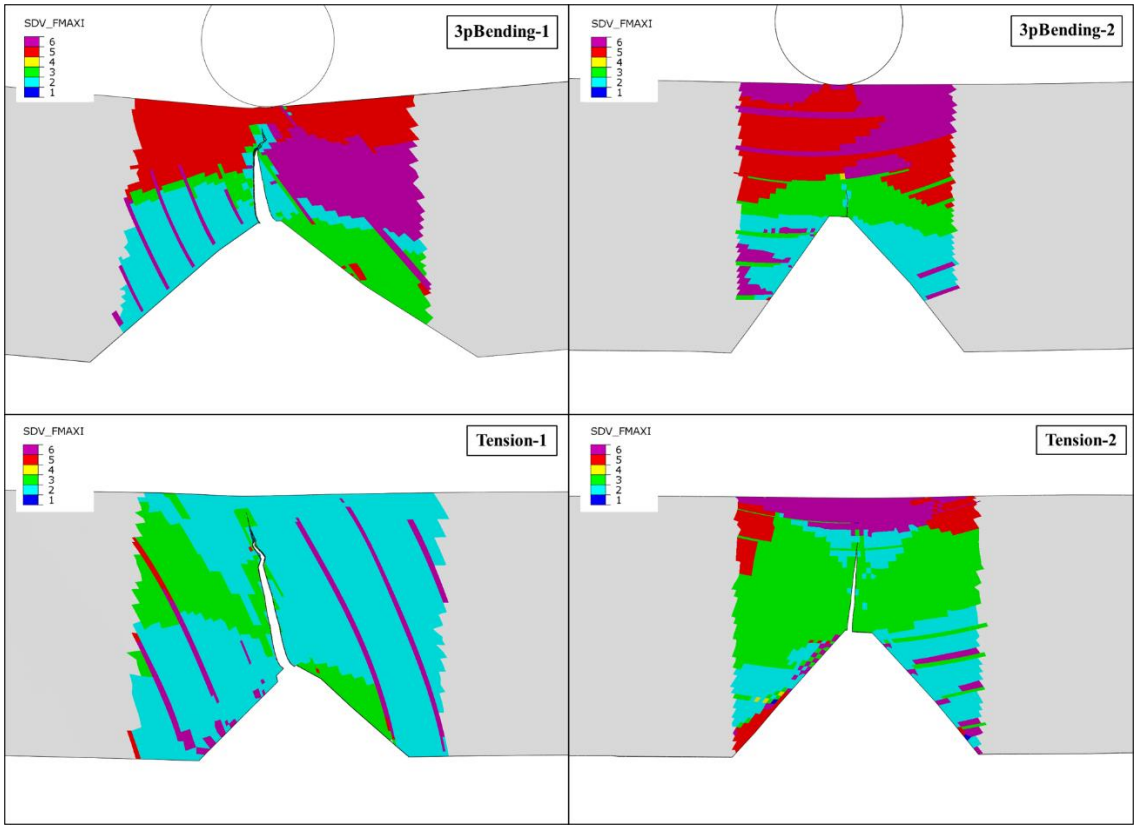

Fig. 27: Contour plot of the most critical damage criterion (SDV_FMAXI) per element. (Source: own illustration)

The comparison of the results of the 3-point bending tests is shown in Fig. 28 and the tensile tests in Fig. 30 respectively. The origin of the cylindrical coordinate systems was determined by averaging the centers of the annual rings near the edge-notch. With this method, the stiffness was reproduced accurately with the FE models, see the force-displacement diagrams. However, the tougher challenge is to determine the ultimate load, which was less successful in the case of the 3-point bending tests than in the case of the tensile tests. A summary of the results can be found in Tab. 20.

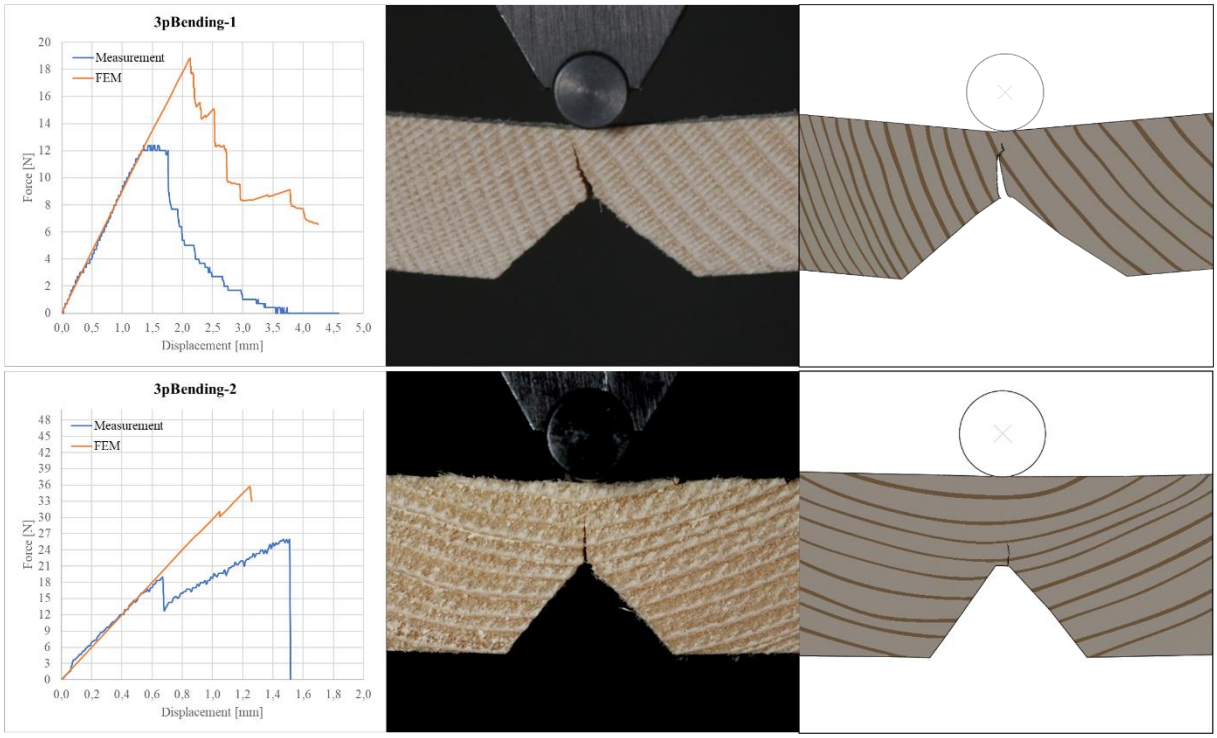

Fig. 28: Comparison of the measurement and XFEM results of the 3-point bending tests: force-displacement diagram (left); photo of measurement (middle); screenshot of XFEM (right).

(Source: own illustration)

In the case of the 3-point bending test, both the starting point of the crack and its initial path are well predicted by the XFEM calculation. For specimen *3pBending-1*, the ultimate load is overestimated by about 50%. This is due to the fact that in the calculation the crack propagates through a latewood layer, while in reality the crack path only propagates in the earlywood layer. Fig. 29 shows the acting damage criteria per element for this specimen. It can be clearly seen that the critical failure modes are tension in radial (*SDV_RFTR*) and tangential (*SDV_RFTT*) directions, which are alternately most critical as the crack progresses.

For specimen ”*3pBending-1*” the fracture energy plays a major role. It can be seen that after reaching the ultimate load, the horizontal plateau of the force-displacement curve is not accurately represented in the XFEM calculation, but the regression of the curve is correct with sufficient accuracy. In specimen ”*3pBending-2*”, failure occurs abruptly after the first two latewood layers crack. The XFEM calculation runs into convergence difficulties when calculating the contact under the stamp and it terminates earlier as defined.

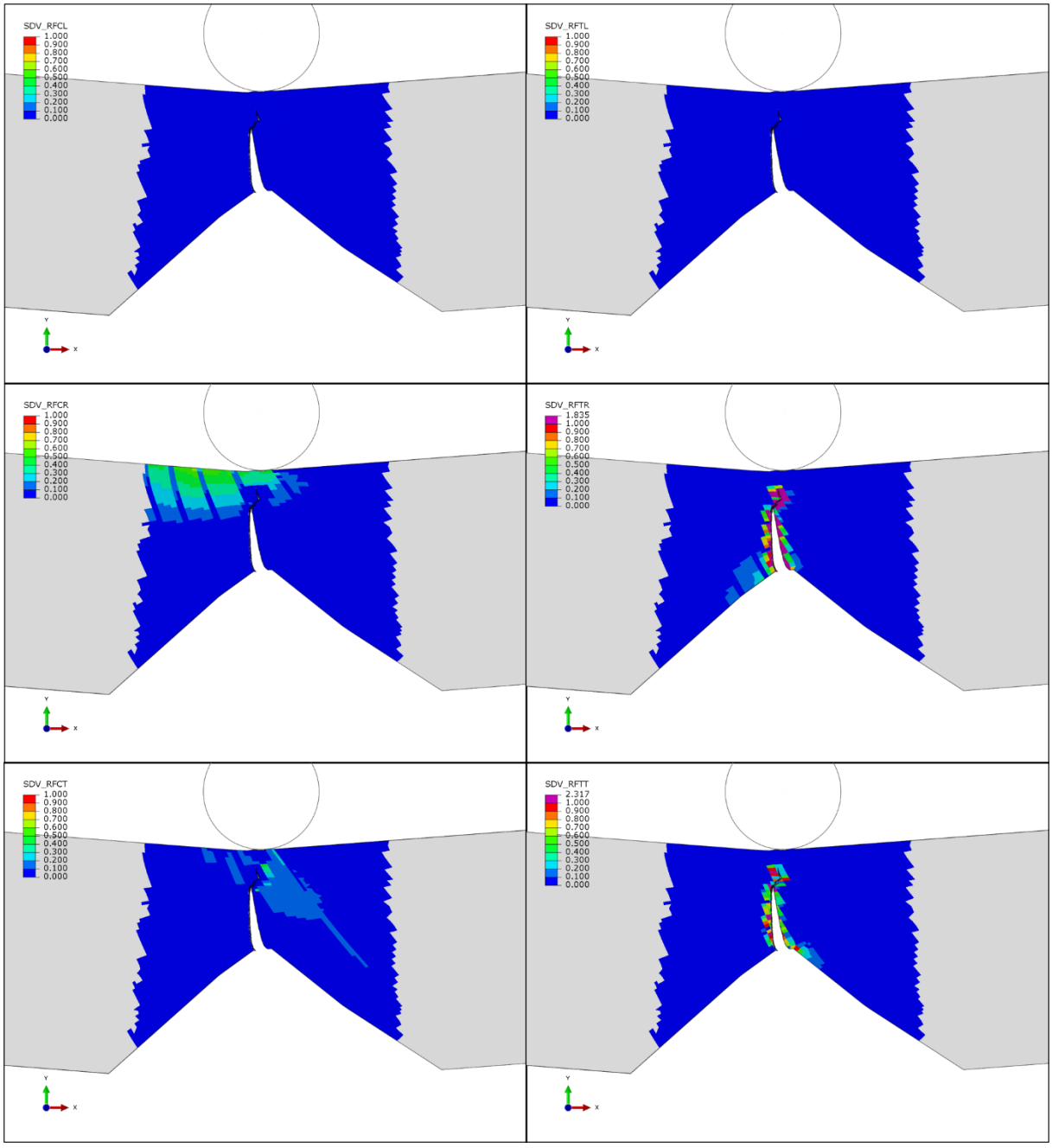

Fig. 29: Contour plot of the damage modes: as an example, test specimen 3pBending-1. (Source: own illustration)

For the specimen *3pBending-2*, the first earlywood layer fails at 19 N in the measurement and at 31 N in the XFEM calculation. Afterwards, the loss of stiffness in the XFEM model is lower, but the final failure occurs earlier than in the measurement. The stiffness values of the selected specimens in the 3-point bending tests are quite low, which makes this type of calculation particularly sensitive to modeling as well as to accurate material values.

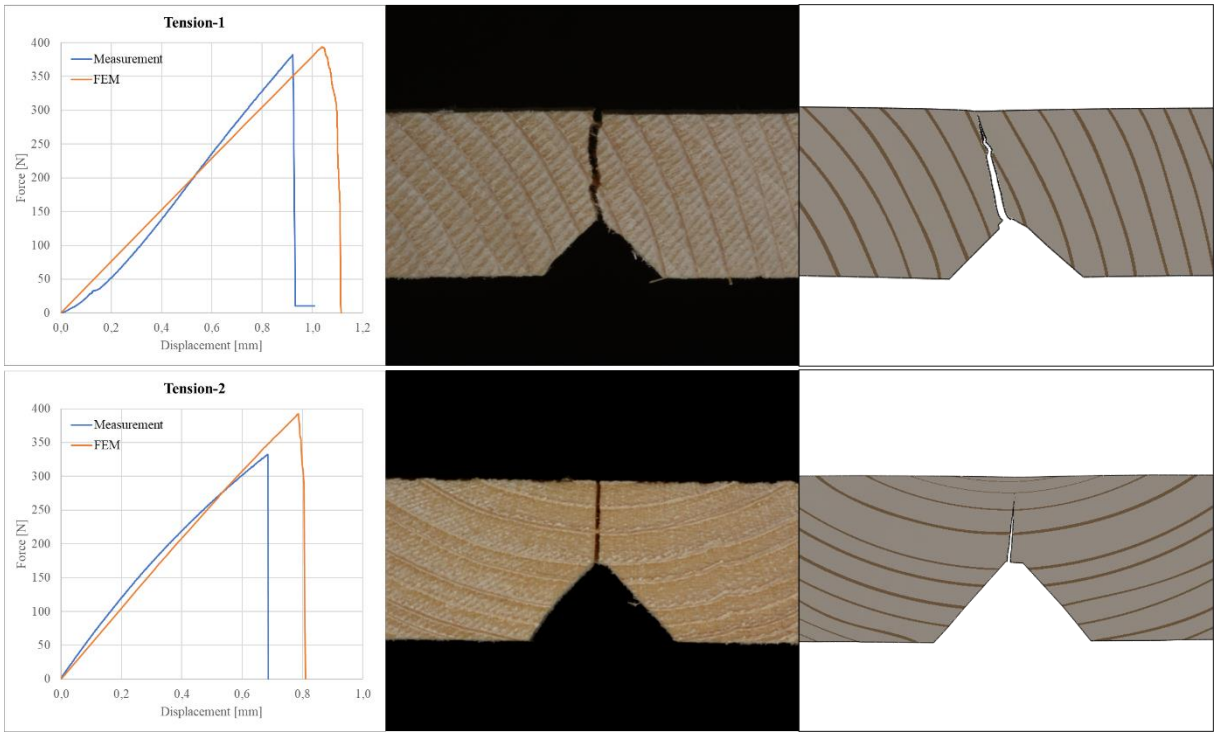

Fig. 30: Comparison of the measurement and XFEM results of the tensile tests: force-displacement diagram (left); photo of measurement (middle); screenshot of XFEM (right).

(Source: own illustration)

The results of the tensile tests generally show a much better agreement than the 3-point bending test. The ultimate loads are overestimated by less than 20% and the crack initiation points are predicted correctly in both cases. The crack path agrees with very good accuracy for the specimen ”*Tension- 2*”. For specimen ”*Tension-1*”, the direction of crack growth is correct at the beginning, but in reality the crack reaches the latewood layer earlier. In this specimen, the failure modes tension in radial and tangential directions vary during the failure, resulting in a jagged crack path. In the tensile test, the fracture energy plays a less important role than in the 3-point bending test, because of the brittle fracture. The simulations also converge better because there is no sliding in the contacts considered while deterioration.

Overall, it can be concluded that the quality of the results means that the *3. Hypothesis* is plausible, see Tab. 20.

Tab. 20: Summary table of measurement and XFEM results

(Source: own illustration)

Basic information:

specimen	height at the notch [mm]	annual ring orientation at the notch [deg]	latewood ratio recognized by the tool [%]
3pBending-1	9.0	28.4	18.8
3pBending-2	9.3	90.0	24.7
Tension-1	13.0	33.5	32.3
Tension-2	10.1	90.0	24.1

Comparison of weight [g]:

specimen	measurement	FE model	difference in [%]
3pBending-1	18.8	18.2	-3.6
3pBending-2	24.7	19.5	-26.7
Tension-1	32.3	31.2	-3.5
Tension-2	24.1	22.9	-5.4

Comparison of ultimate load [N]:

specimen	measurement	XFEM	difference in [%]
3pBending-1	12.4	18.8	34.1
3pBending-2	26.0	35.7	27.2
Tension-1	382.4	393.5	2.8
Tension-2	332.4	388.7	14.5

7 Summary and prospects for future research

Depending on the task, the analysis of wooden structures can be done on different anatomical scales: from atomic through micro -microfibrils- or meso -annual rings-to macro- the wooden bulk itself. By the numerical modeling of wood used as a construction material, it is a more appropriate way to investigate its properties on the meso scale. The results gained through experiments give a better understanding of the behavior of timber beams under loading. The aim was to reconstruct the experiments by using the photos of end-grains and creating unique FE models of timber beams, which lead to an outcome shown by the experiments. As for any other modeling approach, a major issue lies in the determination of the necessary mechanical properties. As the model performance and prediction capacity is highly dependent on these properties.

In the first stage of my research, two hypotheses have been introduced, with the help of which, the measurement results can be reproduced by finite element simulation. The first one states, that for high quality wood we can assume, that the surface and volume ratios of the earlywood and latewood nearly equals in all cross-sections along the longitudinal axis of the beam. The second one introduces empirical formulas for the orthotropic material properties with the help of the ROM-relation and the correlation among the material properties and density of earlywood and latewood. The results of the compared measurements and FE calculations show a good correlation within the linear elastic limit.

To create the finite element models, a photoanalytical processing tool was used to detect the annual ring pattern of the specimens on the images. The annual ring detection tools use the fact, that the brightness of the wood changes from the earlywood layer to the latewood layer. For this purpose, an object detection algorithm is used to detect the end-grain cross section in the image and an edge detection algorithm is used to determine the annual rings. To improve the performance of the tool detecting the annual rings, the specimens can be painted. Some of the specimens were painted with a colorless nitro topcoat (Milesi LEC 040). The treatment does not affect the strength properties of the specimens, but it does highlight the annual rings. The treatment makes it easier for the photoanalytical program to distinguish between latewood and earlywood.

There is also a growing need to combine the experimental data with finite element models to develop a material model that adequately represents the macroscopic failure behavior of wood. The results of many researchers' experimental campaigns show how difficult it is to determine the failure properties of wood, which are often system properties rather than material

properties. In the second stage of my research, XFEM with linear elastic fracture mechanics is used to describe the crack initiation and propagation. At this point, the 3. Hypothesis was formulated, that it is possible to describe the damage processes of Norway spruce with the presented failure criteria. To describe the failure mechanisms of the Norway spruce clear wood specimens, 6 damage initiation criteria are used. A normal vector to the crack surface is calculated for each damage mode, taking into account the orientation of the maximum and minimum principal stresses. In examining the fracture of wood at the meso scale, no attempt is made to investigate the failure at lower levels of material structure, only the behavior under load. The predictive ability of the failure model is highly dependent on appropriate calibration. This work is related to Norway spruce only and for other species, new measurements and calibrations are certainly required, but the species-specific failure model may also be necessary.

For the FE calculations, orthotropic material properties of earlywood and latewood, and the relationship between the density and strength of Norway spruce were used. To determine the failure properties for earlywood and latewood, 3-point bending, tension, and compression tests to failure were conducted. The experiments were recorded with a high-resolution highspeed camera, where the failure mode and the crack path are clearly visible. The force-displacement curves were also recorded and synchronized with the video footages. After obtaining the failure properties, further edge-notched specimens from the same batch were tested until failure. These specimens were also calculated using XFEM in ABAQUS, and the ultimate load and crack propagation in the specimens were compared with the measurement results. However, this required sufficiently accurate finite element models.

In the 3-point bending tests, both the starting point of the crack and its initial path are well predicted by the XFEM calculation. In reality, however, the crack sometimes propagates between the earlywood and latewood layers in the transition zone. In such situations, the XFEM calculation overestimates the ultimate load. Considering the transition zone could be quite cumbersome, but a debonding mechanism between earlywood and latewood could be a possible simplified solution to obtain even more accurate results. The results of the tensile tests show an even better agreement than in case of the 3-point bending tests. The tensile specimens break with brittle fracture, so the fracture energy plays a less important role than in the 3-point bending tests. Also, no major sliding effects of the crack surfaces have to be considered, which generally leads to better convergence. The LEFM is only suitable for problems where the zone of plasticity is small compared to the crack size. However, there are studies on ductile and elasto-plastic fracture problems where strain-softening is considered to adequately capture larger plasticized areas. With the gathered knowledge for this development, it would be possible to

further develop the damage model, which can also take into account the failure under compression. Overall, it can be stated that the use of a subroutine requires some expertise. The user is advised that the implementation of a realistic constitutive model requires extensive development and testing.

In the future, when creating finite element models from a 2D cross sectional mesh, one should consider the entasis of the wood and further increase the level of realism of the developed model. In addition, the potential of the presented XFEM calculations can be used to build up a database for design and future model validation by investigating material failure behavior. For this purpose, the model generation should be further automated, perhaps using today's increasingly popular artificial intelligence technology. It is definitely time to explore the artificial intelligence in case of wood and training it with the collected databases so that more accurate results can be obtained with the FE models in the future.

Doctoral Thesis

1. Thesis

For class A (highest quality class) or class B wood it can be assumed, that proportion of earlywood and latewood in the end cross-section of the analyzed timber beam is constant in all cross-sections along its longitudinal axis.

For the development of the finite element model of timber beams, their unique annual ring pattern is considered. The HSV color spectrum of picture of the end-grain pattern is analyzed in combination with the Canny edge detection technique using a proprietary photo analytical tool in order to separate the earlywood and latewood phases in the bulk.

By determining the surface ratio of earlywood and latewood, the thesis states that this value can be converted to a volume ratio. The density of the earlywood and latewood rings can be determined by measuring finite small specimens. If the assumptions are good enough, the given formula should lead to the measured weight of the beam. This indicator is easy to determine and non-destructive.

The results of the compared measurements and finite element models based on the introduced thesis show good agreement within the linear elastic limit. For natural wood, EUROCODE 5 requires a safety factor of at least 1.3, which is very optimistic. For this reason, the values within the 30% margin of error can be considered good.

2. Thesis

The rule of mixtures combined with the correlation between the orthotropic material properties and density of earlywood and latewood lead to equations, which can be used to define the stiffness relations for the Norway spruce between earlywood and latewood.

Based on the conducted research the material properties of earlywood and latewood for Norway spruce are obtained. These values provide a good basis for further investigations. However, it should be noted, that depending on the origin of the wood material, a recalibration of the material values may be necessary. The equations established in this thesis allow the determination or calibration of the material values for the batch of Norway spruce used.

3. Thesis

With the presented failure criteria and failure stress values, it is possible to describe the damage processes and the crack propagation of clearwood Norway spruce specimens in case of brittle failure.

Wood shows ductile behavior in compression and brittle behavior in tension and shear, where both failure modes can occur simultaneously. In cases, where wood mainly behaves like a brittle material, the linear elastic fracture mechanic principles based on the fracture toughness parameter K_{IC} are able to characterize the fracture process adequately. In these cases, the failure of spruce specimens can be described by 6 failure criteria. The damage initiation mechanisms are: tension and compression in the 3 main directions. Pure shear modes are not considered.

When at least one of the 6 failure criteria is met, the damage initiation is triggered. The criterion that reaches the critical value sooner is responsible for the failure.

Overall, it can be concluded that the quality of the results means that the 3rd thesis is plausible.

References

Andor, K., Lengyel, A., Polgár, R., Fodor, T., Karácsonyi, Z. (2015): Experimental and statistical analysis of spruce timber beams reinforced with CFRP fabric. Construction and Building Materials, Vol. 99, pp. 200-207

Anphy, J., Deepa, M., Naiji, J., Silpa, E.G., Anjitha, V. (2014): Performance study of edge detection operators. 2014 International Conference on Embedded Systems, Coimbatore, India, pp. 7-11

Anonymous (1997): Nordic Timber - Grading rules for pine and spruce sawn timber. 2nd Edition. Arbor Publishing, Stockholm, pp. 64

Ashby, M. F., Easterling, K. E., Harryson, R., & Maiti, S. K. (1985): The fracture toughness of woods. Proceedings of the Royal Society of London. Series A, Mathematical and Physical Sciences, Vol. 398(1815), pp. 261–280

ASTM D198-02: Standard Test Methods of Static Tests of Lumber in Structural Sizes.

Balter, S. (1993): Fundamental properties of digital images. Radio Graphics, Vol. 13, pp. 129–141

Belalpour Dastjerdi, P.; Landis, E.N., (2021): Growth Ring Orientation Effects in Transverse Softwood Fracture. MDPI Materials 2021, Vol. 14, article number 5755

Belytschko, T., & Black, T. (1999): Elastic crack growth in finite elements with minimal remeshing. International Journal for Numerical Methods in Engineering, Vol. 45, pp. 601–620

Brocks, W. (2018): Plasticity and Fracture. (1st ed.): Springer.

Bodig, J., Jayne, B.A., (1993): Mechanics of Wood and Wood Composites. Rep. Edition, Krieger Publishing, pp. 291-30

Bodig., J., (1965): The effect of anatomy on the initial stress-strain relationship in transverse compression. Forest Products Journal, Vol. 15(5): pp. 197-202

Bulcke, J. V., Wernersson, E. L. G., Dierick, M., Loo, D. V., Masschaele, B., Brabant, L., Boone, M. N., Hoorebeke, L. V., Haneca, K., Brun, A., Hendriks, C. L., Acker, J. V., (2014):

3D tree-ring analysis using helical X-ray tomography, Dendrochronologia, Vol. 32(1), pp. 39-46

Canny, J. (1986): A computational approach to edge detection. IEEE Transactions on Pattern Analysis and Machine Intelligence, Vol. 6, pp. 679–698

Cerda, M., Hitschfeld, N., & Mery, D. (2007): Robust tree-ring detection. Conference: Advances in Image and Video Technology, Second Pacific Rim Symposium, PSIVT 2007, Santiago, Chile, pp. 575–585

Cho, H., Sung, M., & Jun, B. (2016): Canny text detector: Fast and robust scene text localization algorithm. Conference: 2016 IEEE Conference on Computer Vision and Pattern Recognition (CVPR), pp. 3566–3573

Dassault Systèmes (2019): Abaqus 2020: Analysis User's Manual.

Dahl, K.B., Malo, K.A. (2009): Linear shear properties of spruce softwood. Wood Science and Technology, Vol. 43, pp. 499-525

De Megistris, F., & Salmén, L. (2015): Finite Element modelling of wood cell deformation travsverse to the fibre axis. Materials Science, Nordic Pulp and Paper Research Journal, Vol. 23, pp. 240–246

Deta, U., Suprapto, N., Mubarok, H., Syaiful Adam, A., Kholiq, A. (2019): The comparison of static friction coefficient on wood between the combination of wood-metal load system and wood-sand load system, Conference: Proceedings of the International Conference on Science and Technology (ICST 2018), pp. 887–890

DIN EN 408-2012-10 (2012): Timber structures. Structural timber and glued laminated timber. Determination of some physical and mechanical properties.

Dívós, F., Horváth, M. (2006): Faanyag rugalmas állandóinak dinamikus meghatározása, összehasonlítása. [Dynamic determination and comparison of elastic constants of wood.] Faipar, Vol. 54, pp. 3-8

Ebrahimi, G., Sliker, A. (1981): Measurement of shear modulus in wood by a tension test. Wood Science, Vol. 13, pp. 171-176

Ehart, R. J. A., Stanzl-Tschegg, S. E., & Tschegg, E. K. (1999): Mode III fracture energy of wood composites in comparison to solid wood. Wood Science and Technology, Vol. 33, pp. 391–405

EN 1995 (2004): Eurocode 5 - Design of Timber Structures

Fajdiga, G., Rajh, D., Nečemer, B., Glodež, S., Šraml, M. (2019): Experimental and Numerical Determination of the Mechanical Properties of Spruce Wood. MPDI Forest, Vol. 10(12), article number 1140

Fleischmann, M., (2005): Numerische Berechnung von Holzkonstruktionen unter Verwendung eines realitätsnahen orthotropen elasto-plastisches Werkstoffmodells (in German: Numerical calculation of timber structures using a realistic orthotropic elasto-plastic material model): PhD Dissertation. Technische Universität Wien

Füssl, J., Li, M., Lukacevic, M., & Martin, C. (2016): Three different methods for predicting the strength behaviour of clear wood - A performance comparison and basis for a combined approach. Conference: WCTE 2016 - World Conference on Timber Engineering

Gecys, T., Daniunas, A., Bader, T.K., Wagner, L., Eberhardsteiner, J. (2015): 3D finite element analysis and experimental investigations of a new type of timber beam-to-beam connection. Engineering Structures, Vol. 86, pp. 134-145

George, M., Lakshmi, C. (2013): Object Detection using the Canny Edge Detector. International Journal of Science and Research (IJSR), Vol. 2(5), pp. 213-215

Gereke, T., Hering, S., Niemz, P. (2015): Finite element analysis of wood adhesive joints. Pro Ligno 12(1), pp. 13-14

Gibson, L.J. Ashby, M.F. (1997): Cellular solids: Structure and properties. Cambridge University Press, pp. 510

Guindos, P. (2014): Comparison of different failure approaches in knotty wood, Vol. 57, pp. 51–68

Habite, T., Abdeljaber, O., Olsson, A. (2021): Automatic detection of annual rings and pith location along Norway spruce timber boards using conditional adversarial networks, Wood Science and Technology, Vol. 55(9), pp. 461-488

Hashin, Z., & Rotem, A. (1973): A fatigue failure criterion for fiber reinforced materials. Journal of Composite Materials, Vol. 7, pp. 448–464

Hashin, Z., & Rotem, A. (1980): Failure criterion for unidirectional fiber composites. ASME Journal of Applied Mechanics, Vol. 47, pp. 329–334

Hearmon, R.F.S. (1948): The Elasticity of wood and plywood – Forest Product Research, Special Report No. 7; London: His Majesty's Stationery Office, pp. 5-57

Hoffman, O. (1967): The brittle strength of orthotropic materials. Journal of Composite Materials, Vol. 1, pp. 200–206

Hu, M., Olsson, A., Johansson, M., Oscarsson, J., (2018): Modelling local bending stiffness based on fibre orientation in sawn timber. European Journal of Wood and Wood Product, Vol. 76, pp. 1605–1621

Irwin, G. R. (1957): Analysis of stresses and strains near the end of a crack traversing a plate. Journal of Applied Mechanics, Vol. 24, pp. 361–364

Isaac, M.D., Ori, I. (2006): Engineering Mechanics of Composite Materials. (Second ed.) Oxford University Press, pp. 464

Janssen, M., Zuidema, J., & Wanhill, R. (2004): Fracture Mechanics: Fundamentals and Applications.

Jernkvist, L.O., Thuvander, F. (2001): Experimental determination of stiffness variation across annual rings in Picea abies. Holzforschung, Vol. 55(3), pp. 309-317

Keunecke, D., Sondereeger, W., Pereteanu, K., Lüthi, T., Niemz, P. (2007): Determination of Young's and shear moduli of common yew and Norway spruce by means of ultrasonic waves. Wood Science and Technology, Vol. 41, pp. 309-327

Khokhar, A., Zhang, H., Ridley-Ellis, D., Moore, J. (2010): The shear strength and failure modes of timber joists obtained from the torsion test method. 11th World Conference on Timber Engineering 2010, pp. 20-24

Király T., Polgár R., Andor K. (2020): Modeling the early- and latewood annual rings as orthotropic material for FE calculation of Norway spruce timber beams using the rule of

mixture. Abstract book for the 16th Miklós Iványi International PhD & DLA Symposium, Pollack Press, pp. 73-74

Király T. (2021): Macroscopic Material Degradation Model of Wood for XFEM using the Rule of Mixtures. Abstract book for the 17th Miklós Iványi International PhD & DLA Symposium, Pollack Press, pp. 147-148

Király, T., & Karácsonyi, Z. (2023a): Fracture testing of edge-notched timber beams with different growth ring orientations. Wood Research, Vol. 68(3), pp. 558–571

Király, T., Karácsonyi, Z., & Polgár, R. (2023b): Modeling the earlywood and latewood growth rings of Norway spruce timber beams for finite element calculation. Wood Research, Vol. 68(1), pp. 28–43

Király, T., Karácsonyi, Z., & Polgár, R. (2023c): Macroscopic material degradation model of Norway spruce clear wood for XFEM. Results in Engineering, (*to be published*)

Kyziol, L. (2010): Analysis of fracture toughness of structural timber. POLISH MARITIME RESEARCH, Vol. 17, pp. 53–58

Le-Ngoc, L., & McCallion, H. (1997): On the fracture toughness of orthotropic materials. Elsevier Science Ltd., Engineering Fracture Mechanics, Vol. 58, pp. 355–362

Liu, J.Y., 2002: Analysis of off-axis tension test of wood specimens. Wood and Fiber Science, Vol. 34, pp. 205-211

Liu, J.Y., Ross, R.J., 2005: Relationship between radial compressive modulus of elasticity and shear modulus of wood. Wood and Fiber Science, Vol. 37, pp. 201-206

Luimes, R. A., Suiker, A. S. J., Verhoosel, C. V., Jorissen, A. J. M., & Schellen, H. L. (2018): Fracture behaviour of historic and new oak wood. Wood Science and Technology, Vol. 52, pp. 1243–1269

M. Cerda, N. Hitschfeld-Kahler, and D. Mery (2007): Robust Tree-Ring Detection. Pacific-Rim Symposium on Image and Video Technology 2007, LNCS 4872, pp. 575-585

Melenk, J., & Babuska, I. (1996): The partition of unity finite element method: Basic theory and applications. Computer Methods in Applied Mechanics and Engineering, Vol. 39, pp. 289–314

Modén, C.S., Berglund, L. A. (2008): A two-phase annual ring model of transverse anisotropy in softwoods. Composites Science and Technology, Vol 68(14), pp. 3020-3026

Moës, N., Dolbow, J., & Belytschko, T. (1999): A finite element method for crack growth without remeshing. International Journal for Numerical Methods in Engineering, Vol. 46, pp. 131–150

Moshtaghin, A.F., Franke, S., Keller, T.P., Vassilopoulos, A. (2021): Experimental investigation of mesoscale variability of clear spruce mechanical properties in the radial direction. Construction and Building Materials, Vol. 270-121401

Nairn, J. A. (2007): A numerical study of the transverse modulus of wood as a function of grain orientation and properties. Holzforschung, Vol. 61(4), pp. 406–413

Nairn, J.A., 2006: Numerical simulations of transverse compression and densification in wood. Wood a Fiber Science, Vol. 38(4), pp. 576-591

Nilsen, T.S. (2015): Numerical modelling of wood microstructure. Master Thesis. Norwegian University of Science and Technology, NTNTU Trondheim, pp. 7-12

Norris, C. B. (1962): Strength of orthotropic materials subjected to combined stresses. Misc. Pub FPL-1816. Madison, Wis.: U.S. Dept. of Agriculture, Forest Service, Forest Products Laboratory. (40 pages)

Ormarsson, S., Dahlblom, O., Johansson, M. (2008): Finite element study of growth stress formation in wood and related distortion of sawn timber. Wood Science and Technology, Vol. 43, pp. 387-403

P. C. Conrad, M., D. Smith, G., & Fernlund, G. (2003): Fracture of solid wood: a review of structure and properties at different length scales. Wood and Fiber Science, Journal of the Society of Wood Science and Technology, Vol. 35(4), pp. 570-584

Pietikäinen, M., & Okun, O. (2001): Edge-based method for text detection from complex document images. Conference: Document Analysis and Recognition, 2001. Proceedings. Sixth International Conference, pp. 286-291

Pinho, S., Dávila, C. G., Camanho, P. P., & Iannucci, L. (2005): Failure models and criteria for FRP under in-plane or three-dimensional stress states including shear non-linearity. Technical Report NASA Langley Research Center, Hampton, VA. NASA/TM-2005-213530.

Polgár, R. (2017): Offer for the quantitative determination of selection of stacked wood photo analytical processing algorithm by using spline functions. PhD Dissertation. West Hungarian University, pp. 23-44

Qing, H., Mishnaevsky, Jr. L. (2010): 3D multiscale micromechanical model of wood: From annual rings to microfibrils. International Journal of Solids and Structures, Vol. 47(9), pp. 1253-1267

Raftery, G.M., Kelly, F., 2015: Basalt FRP rods for reinforcement and repair of timber. Composites Part B: Engineering 70: pp. 9–19.

Ramadevi, Y., Sridevi, T., Poornima, B., Kalyani, B. (2010): Segmentation and object recognition using edge detection techniques. International Journal of Computer Science & Information Technology (IJCSIT), Vol 2(6), pp. 153-161

Raposo, P., Correia, J., Sousa, D., Salavessa, M., Reis, C., Oliveira, C. and De Jesus, A., (2017): Mechanical Properties of Wood Construction Materials from a Building from the 19th Century. Procedia Structural Integrity, Vol. 5, pp. 1097-1101

Ross, R.J. (2010): Wood handbook: Wood as an engineering material. Centennial ed. General technical report FPL-GTR-190. Madison WI, U.S. Dept. of Agriculture. Forest Service, Forest Products Laboratory, chapters 3 & 5

Ruta, A., Porikli, F., Watanabe, S., & Li, Y. (2011): In-vehicle camera traffic sign detection and recognition. Machine Vision Applications, Vol. 22, pp. 359–375

Saad, K., Lengyel, A. (2021): Inverse calculation of timber-CFRP composite beams using finite element analysis. Periodica Polytechnica Civil Engineering, Vol. 65(2), pp. 437–449

Salmén, L., Megistris, F.D. (2008): Finite element modelling of wood cell deformation travsverse to the fibre axis. Nordic Pulp and Paper Research Journal, Vol. 23(2), pp. 240-246

Sandhaas, C., & van de Kuilen, J. (2013): Material model for wood. Heron, Vol. 58(2), pp. 179–199

Serrano, E., Enquist, B., 2010: Compression strength perpendicular to grain in cross-laminated timber (CLT). 11th World Conference on Timber Engineering 2010, WCTE 2010, Vol. 1, pp. 441-448

Shao, B., Lewis, N., Fischer, A., Huang, Y., Lancelot, F. (2020): Parameters identification for wood material (*MAT143) and its application on the modeling of a typical timber nuki joint. 16th International LS-DYNA® Users Conference, pp. 16

Sih, G. C., Paris, P. C., & Irwin, G. R. (1965): On cracks in rectilinearly anisotropic bodes. International Journal of Fracture Mechanics, Vol. 1, pp. 189–203

Sliker, A., Yu, Y., (1993): Elastic constants for hardwoods measured from plate and tension tests. Wood and Fiber Science, Vol. 25, pp. 8-22

Song, J. H., Areias, P. M. A., & Belytschko, T. (2006): A method for dynamic crack and shear band propagation with phantom nodes. International Journal for Numerical Methods in Engineering, Vol. 67, pp. 868–893

Stanzl-Tschegg, S. E., & Navi, P. (2009): Fracture behaviour of wood and its composites. Holzforschung, Vol. 63(2), pp. 139–149

Stolarska, M., Chopp, D. L., Moës, N., & Belytschko, T. (2001): Modelling crack growth by level sets in the extended finite element method. International Journal for Numerical Methods in Engineering, Vol. 51, pp. 943–960

Szalai, J. (1994): Anisotropic elasticity and strength of wood and wood-based materials, Part 1: Anisotropy of mechanical properties [in Hungarian: A faanyag és faalapú anyagok anizotróp rugalmasság- és szilárdságtana, 1. rész: A mechanikai tulajdonságok aniztrópiája]. Hillebrand Nyomda, pp. 38-127

Tampone, G., (2007): Mechanical Failures of the Timber Structural Systems. ICOMOS IWC, XVI International Symposium.

Thorhallsson, E.R., Hinriksson, G.I., Snæbjörnsson, J.T., (2017): Strength and stiffness of glulam beams reinforced with glass and basalt fibres. Composites Part B: Engineer 115, pp. 300–307.

T. Akter, S., & K. Bader, T. (2020): Experimental assessment of failure criteria for the interaction of normal stress perpendicular to the grain with rolling shear stress in norway spruce clear wood. Wood Research, Vol. 78, pp. 1105–1123

Tsai, S. W. (1968): Strength theories of filamentary structure. Fundamental aspects of fiber reinforced plastic composites, R. T. Schwartz and H. S. Schwartz (eds.), Wiley Interscience, New York, pp. 3–11

Warnet, L., Akkerman, R. (2008): Composite mechanics handouts, University of Twente, pp. 19-36

Yoshihara, H., Kubojima, Y., Nagaoka, K. (1998): Measurement of the shear modulus of wood by static bending tests. Journal of Wood Science, Vol 44, pp. 15–20

Zhu, X. (2014): Nondestructive testing and system reliability based on finite element modeling in GFRP-reinforced timber beams. BioResources, Vol 9(3), pp. 5501-5510

Appendix

Photoanalytical processing tool

The amount of coded data goes far beyond several thousand lines, so only an overview of the structure of the tool is given here.

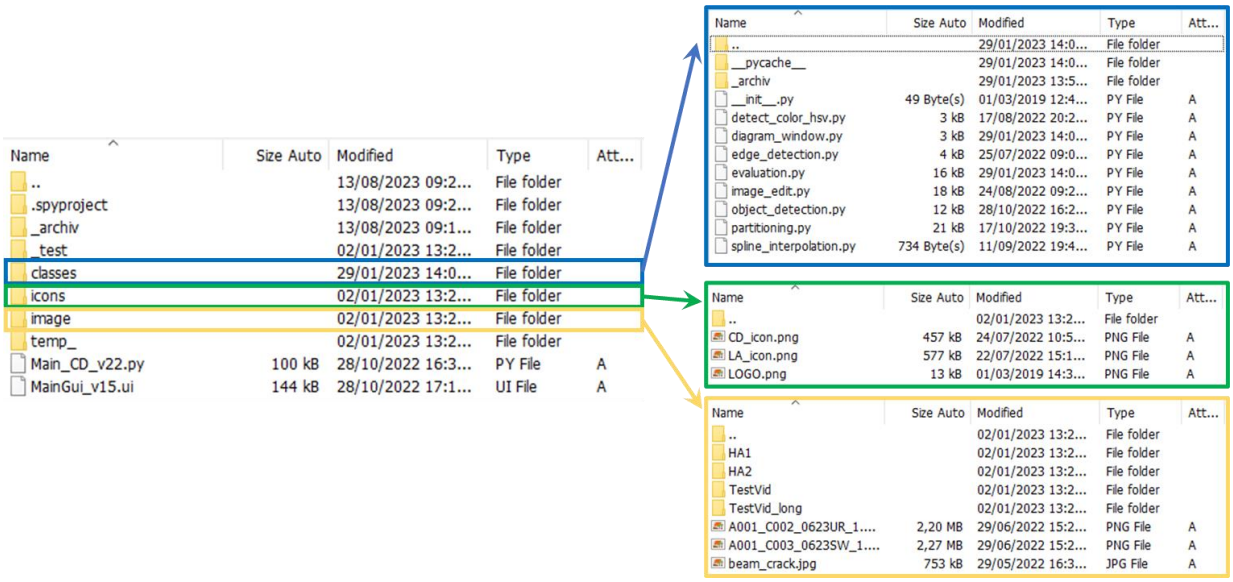

Appx. -Fig. 1: Folder structure of the developed photoanalytical processing tool.

(Source: own illustration)

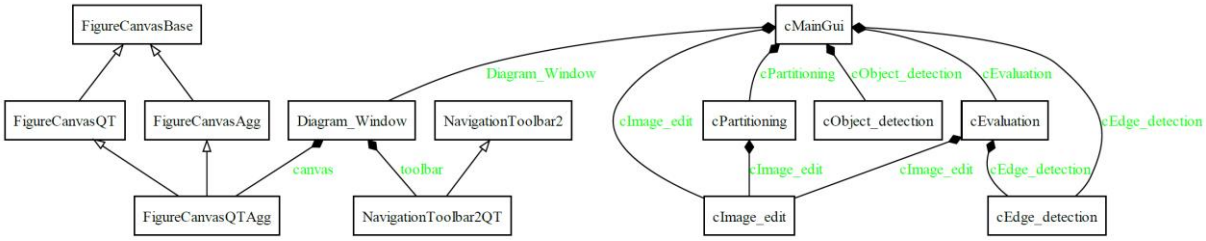

Appx.-Fig. 2: Class diagram of the developed photoanalytical processing tool - main level.

(Source: own illustration)

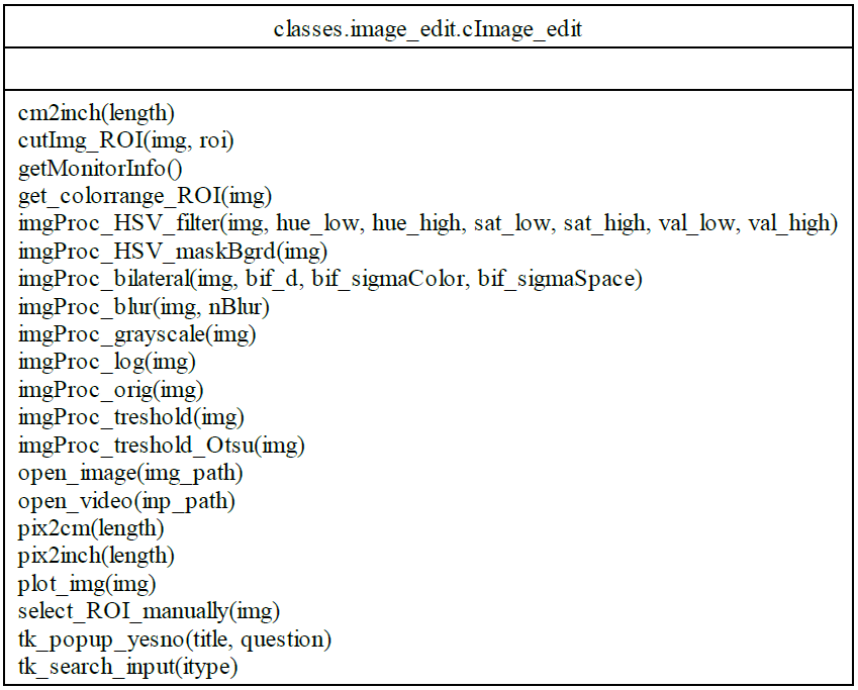

Appx.-Fig. 3: Class diagram of the developed photoanalytical processing tool – sub level of image editing.

(Source: own illustration)

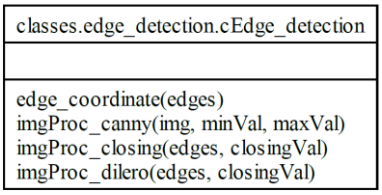

Appx.-Fig. 4: Class diagram of the developed photoanalytical processing tool – sub level of edge detection.

(Source: own illustration)

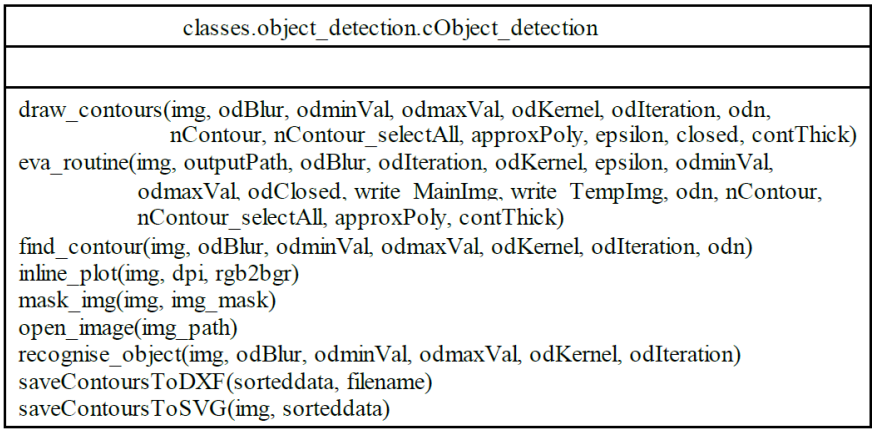

Appx.-Fig. 5: Class diagram of the developed photoanalytical processing tool – sub level of object detection.

(Source: own illustration)

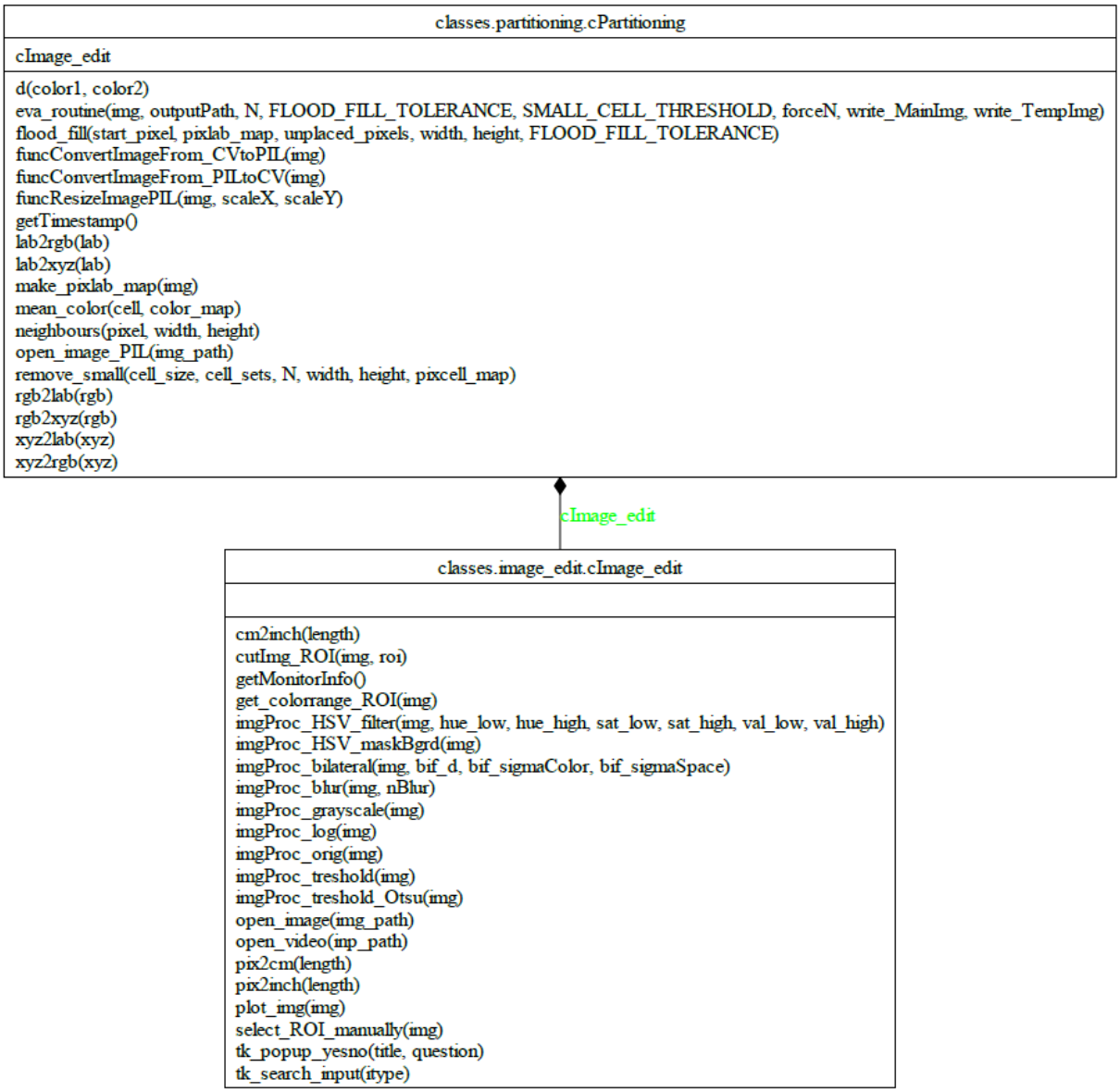

Appx.-Fig. 6: Class diagram of the developed phototanalytical tool – sub level of partitioning (image segmentation).

(Source: own illustration)

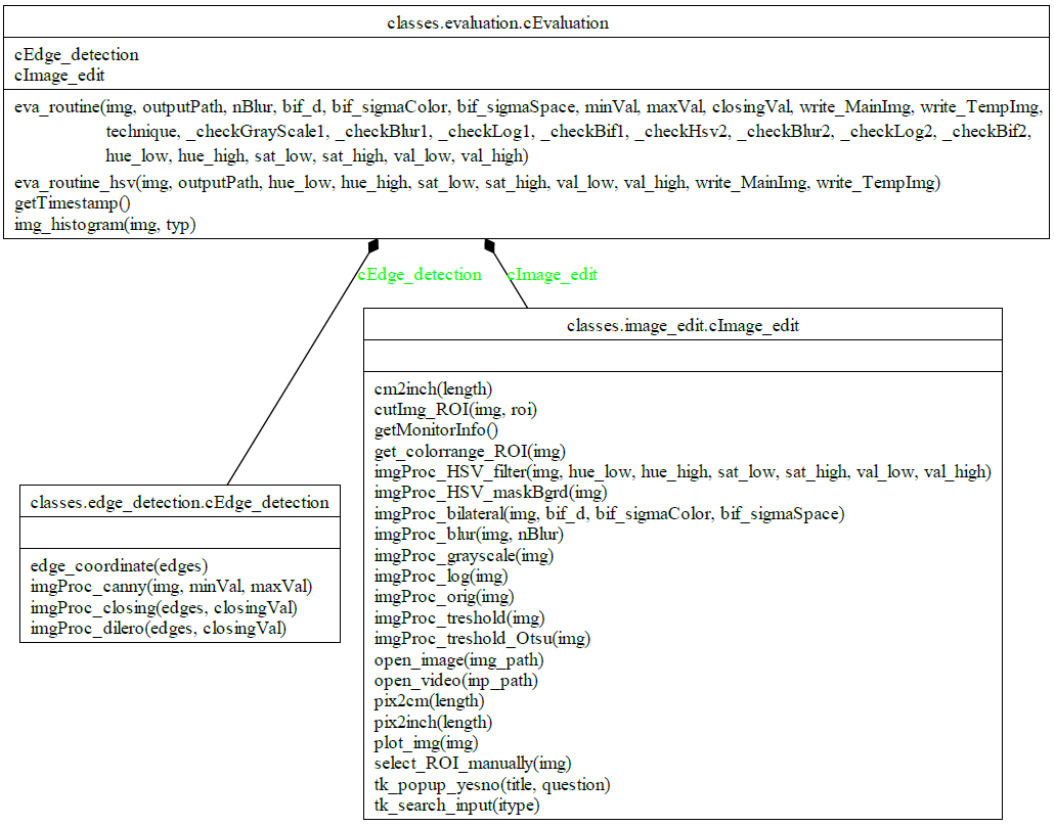

Appx.-Fig. 7: Class diagram of the developed photoanalytical processing tool – sub level of evaluation algorithms.

(Source: own illustration)

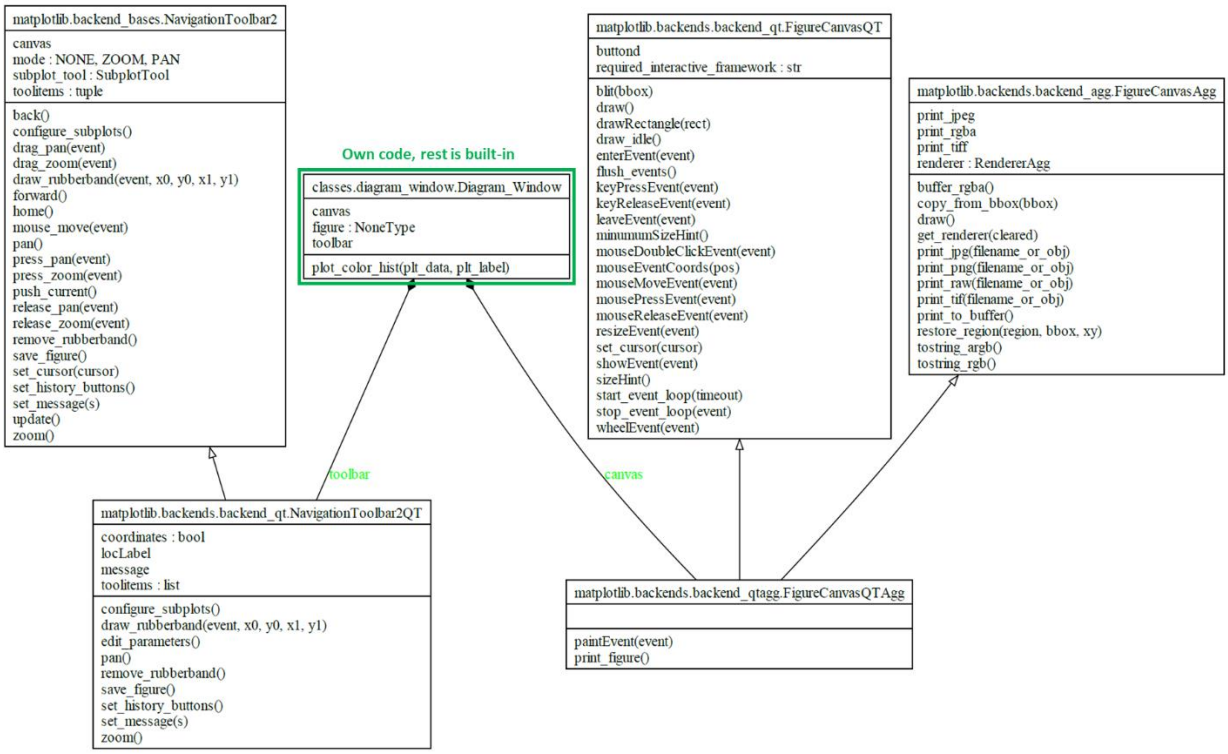

Appx.-Fig. 8: Class diagram of the developed photoanalytical processing tool – sub level of creating new GUI windows.

(Source: own illustration)

Finite element simulations and damage model

Several finite element models were created for the research. Since some of the features at this level were not available in ABAQUS CAE (2017) and I prefer to work in the text editor, I show below the part of the code needed to perform the simulations. I also provide an overview of how the input files of FE model is structured.

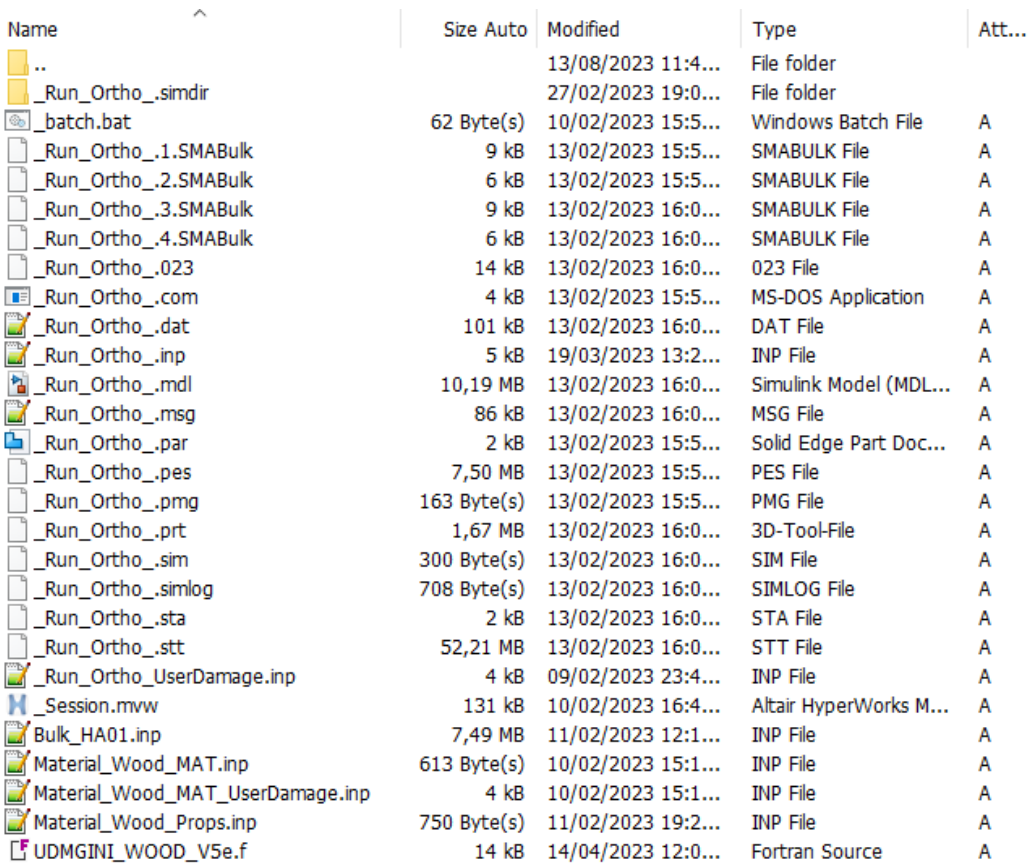

Name	Size Auto	Modified	Type	Att...
..		13/08/2023 11:4...	File folder	
_Run_Ortho_.simdir		27/02/2023 19:0...	File folder	
_batch.bat	62 Byte(s)	10/02/2023 15:5...	Windows Batch File	A
_Run_Ortho_.1.SMABulk	9 kB	13/02/2023 15:5...	SMABULK File	A
_Run_Ortho_.2.SMABulk	6 kB	13/02/2023 15:5...	SMABULK File	A
_Run_Ortho_.3.SMABulk	9 kB	13/02/2023 16:0...	SMABULK File	A
_Run_Ortho_.4.SMABulk	6 kB	13/02/2023 16:0...	SMABULK File	A
_Run_Ortho_.023	14 kB	13/02/2023 16:0...	023 File	A
_Run_Ortho_.com	4 kB	13/02/2023 15:5...	MS-DOS Application	A
_Run_Ortho_.dat	101 kB	13/02/2023 16:0...	DAT File	A
_Run_Ortho_.inp	5 kB	19/03/2023 13:2...	INP File	A
_Run_Ortho_.mdl	10,19 MB	13/02/2023 16:0...	Simulink Model (MDL...	A
_Run_Ortho_.msg	86 kB	13/02/2023 16:0...	MSG File	A
_Run_Ortho_.par	2 kB	13/02/2023 15:5...	Solid Edge Part Doc...	A
_Run_Ortho_.pes	7,50 MB	13/02/2023 15:5...	PES File	A
_Run_Ortho_.pmg	163 Byte(s)	13/02/2023 15:5...	PMG File	A
_Run_Ortho_.prt	1,67 MB	13/02/2023 16:0...	3D-Tool-File	A
_Run_Ortho_.sim	300 Byte(s)	13/02/2023 16:0...	SIM File	A
_Run_Ortho_.simlog	708 Byte(s)	13/02/2023 16:0...	SIMLOG File	A
_Run_Ortho_.sta	2 kB	13/02/2023 16:0...	STA File	A
_Run_Ortho_.stt	52,21 MB	13/02/2023 16:0...	STT File	A
_Run_Ortho_UserDamage.inp	4 kB	09/02/2023 23:4...	INP File	A
_Session.mvw	131 kB	10/02/2023 16:4...	Altair HyperWorks M...	A
Bulk_HA01.inp	7,49 MB	11/02/2023 12:1...	INP File	A
Material_Wood_MAT.inp	613 Byte(s)	10/02/2023 15:1...	INP File	A
Material_Wood_MAT_UserDamage.inp	4 kB	10/02/2023 15:1...	INP File	A
Material_Wood_Props.inp	750 Byte(s)	11/02/2023 19:2...	INP File	A
UDMGINI_WOOD_V5e.f	14 kB	14/04/2023 12:0...	Fortran Source	A

Appx.-Fig. 9: Folder structure of a finite element calculation with ABAQUS (Source: own illustration)

The following input files are required to start the simulation, see Appx.-Fig. 9:

- **_Run_Ortho_.inp:** main input file to start the linear-elastic simulation;
- **_Run_Ortho_UserDamge.inp:** main input file to start the fracture mechanical simulation;
- **Bulk_HA01.inp:** bulk data, which consists the nodal coordinates, element definitions, node and element sets etc…;
- **Material_Wood_MAT:** material definition for the linear elastic simulations;

- **Material_Wood_MAT_UserDamage:** material definition for the fracture mechanical simulations;
- **Material_Wood_Props:** property definitions of the element sets;
- **UDMGINI_WOOD_V5e.f:** developed damage initiation model in FORTRAN for Norway spruce.

Appx. -Tab. 1: ABAQUS input file for specimen HA01 (_Run_Ortho_.inp)

(Source: own illustration)

```
*INCLUDE, INPUT=Bulk_HA01.inp
*INCLUDE, INPUT=Material_Wood_Props.inp
*INCLUDE, INPUT=Material_Wood_MAT.inp
****INCLUDE, INPUT=Material_Wood_MAT_UserDamage.inp
***
***
**************************
*****     SETS     *****
**************************
***
***
*ELSET, ELSET=SO_Bulk
 ELSET_Earlywood, ELSET_Latewood
***
*ELSET, ELSET=SO_Bulk_ENR
 Latewood_dam, Earlywood_dam
***
***
*NSET, NSET=NSET_Bulk, ELSET=SO_Bulk
*NSET, NSET=NSET_Bulk_ENR, ELSET=SO_Bulk_ENR
*ELSET, ELSET=NSET_Bulk
***
***
*******************************
*****     DEFINITION     *****
*******************************
***
***
*ORIENTATION, NAME = Ori_Rec, DEFINITION = COORDINATES, SYSTEM = RECTANGULAR
*** Longitudinal, Radial, Origo
 96.171, 23.318, 1.000,    10.889,  -21.271,  0.00,     96.171, 23.318, 0.000,
 1, 0
*ORIENTATION, NAME = Ori_CYL, DEFINITION = COORDINATES, SYSTEM = CYLINDRICAL
*** Origin, Longitudinal
 96.171, 23.318, 0.000,    96.171, 23.318, 10.000,
*** Material definition is: L R T
 2, -90, 3, -90
```

```
***
***
*** Material lin. elastic
*SOLID SECTION, ELSET=Earlywood, ORIENTATION=Ori_CYL , MATERIAL=MAT_ORTHO_SPRUCE_EW
*SOLID SECTION, ELSET=Latewood, ORIENTATION=Ori_CYL , MATERIAL=MAT_ORTHO_SPRUCE_LW
**
*SOLID SECTION, ELSET=Earlywood_dam, ORIENTATION=Ori_CYL , MATERIAL=MAT_ORTHO_SPRUCE_EW
*SOLID SECTION, ELSET=Latewood_dam, ORIENTATION=Ori_CYL , MATERIAL=MAT_ORTHO_SPRUCE_LW
***
**************************
****     CONTACT     ****
**************************
***
***
*SURFACE INTERACTION, NAME=Int_TIED
***
*SURFACE INTERACTION, NAME=Int_Wood_Metal
*FRICTION
 0.5
***
*CONTACT PAIR, INTERACTION=Int_Wood_Metal, TYPE=SURFACE TO SURFACE
 Surf_Wood_Stamp, Surf_Stamp_Stamp
*CONTACT PAIR, INTERACTION=Int_TIED, TYPE=SURFACE TO SURFACE, TIED, ADJUST=0.1
 Surf_Wood_Fix_1, Surf_Stamp_Fix_1
 Surf_Wood_Fix_2, Surf_Stamp_Fix_2
***
***
***********************************
*****     S T   E   P     *******
***********************************
***
*STEP, NAME=Bending, NLGEOM=YES, INC=100000000, UNSYMM=YES
*DYNAMIC, SINGULAR MASS=WARNING
*** 0.005, 1.0, 1e-9
 0.1, 3.0, 1e-9
***
***
*BOUNDARY, TYPE=VELOCITY
 RB_Fix_1, 2, 5
***
 RB_Fix_2, 2, 5
***
 RB_Stamp, 1, 1
 RB_Stamp, 2, 2, -1.0
 RB_Stamp, 3, 6
***
***OUTPUT, FIELD, FREQUENCY = 1
```

```
*OUTPUT, FIELD, TIME INTERVAL = 0.05
***OUTPUT, FIELD, TIME INTERVAL = 0.005
*NODE OUTPUT
 U,
 RF,
*ELEMENT OUTPUT, POSITION = INTEGRATION POINT, ELSET = SO_Bulk
 S,
 E,
*CONTACT OUTPUT
 CSTRESS
***
*OUTPUT,HISTORY
*ENERGY OUTPUT
 ALLAE, ALLCD, ALLFD, ALLIE, ALLKE, ALLPD, ALLSE,
 ALLVD, ALLWK, ETOTAL
*NODE PRINT
 RF
*END STEP
*****
```

The amount of coded data of the damage initiation model as well as its implementation is extensive and its presentation is cumbersome. Therefore, only an overview of the coded data is given in Appx.-Fig. 10.

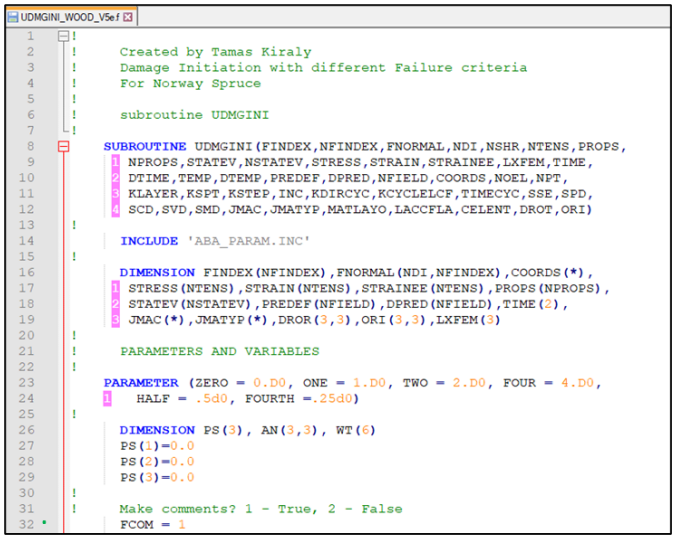

```
UDMGINI_WOOD_V5e.f
!
!     Created by Tamas Kiraly
!     Damage Initiation with different Failure criteria
!     For Norway Spruce
!
!     subroutine UDMGINI
!
      SUBROUTINE UDMGINI(FINDEX,NFINDEX,FNORMAL,NDI,NSHR,NTENS,PROPS,
     1 NPROPS,STATEV,NSTATEV,STRESS,STRAIN,STRAINEE,LXFEM,TIME,
     2 DTIME,TEMP,DTEMP,PREDEF,DPRED,NFIELD,COORDS,NOEL,NPT,
     3 KLAYER,KSPT,KSTEP,INC,KDIRCYC,KCYCLELCF,TIMECYC,SSE,SPD,
     4 SCD,SVD,SMD,JMAC,JMATYP,MATLAYO,LACCFLA,CELENT,DROT,ORI)
!
      INCLUDE 'ABA_PARAM.INC'
!
      DIMENSION FINDEX(NFINDEX),FNORMAL(NDI,NFINDEX),COORDS(*),
     1 STRESS(NTENS),STRAIN(NTENS),STRAINEE(NTENS),PROPS(NPROPS),
     2 STATEV(NSTATEV),PREDEF(NFIELD),DPRED(NFIELD),TIME(2),
     3 JMAC(*),JMATYP(*),DROR(3,3),ORI(3,3),LXFEM(3)
!
!     PARAMETERS AND VARIABLES
!
      PARAMETER (ZERO = 0.D0, ONE = 1.D0, TWO = 2.D0, FOUR = 4.D0,
     1    HALF = .5d0, FOURTH =.25d0)
!
      DIMENSION PS(3), AN(3,3), WT(6)
      PS(1)=0.0
      PS(2)=0.0
      PS(3)=0.0
!
!     Make comments? 1 - True, 2 - False
      FCOM = 1
```

```
!     ----- Radial
      IF ( TSRR .LT. ZERO ) THEN
          RFCR = TSRR*FCRI
      ELSE
          RFCR = ZERO
      END IF
      FINDEX(5) = ABS(RFCR)
        IF ( FCOM == 1) THEN
          IF ( RFCR .GT. ONE ) THEN
              WRITE(7,*) 'Element: ', NOEL
              WRITE(7,*) '    Compressive Failure Mode, RFCR =', RFCR
              WRITE(7,*) '    Max Principial stress 1 =', PS(1)
              WRITE(7,*) '    Max Principial stress 2 =', PS(2)
              WRITE(7,*) '    Max Principial stress 3 =', PS(3)
              WRITE(7,*) '    TSRR =', TSRR
              WRITE(7,*) '    TSTT =', TSTT
              WRITE(7,*) '    TSLL =', TSLL
              WRITE(7,*) '    TSRT =', TSRT
              WRITE(7,*) '    TSRL =', TSRL
              WRITE(7,*) '    TSTL =', TSTL
              WRITE(7,*) '    Max Principial direction KMAX=', KMAX
              WRITE(7,*) '    Max Principial direction KMID=', KMID
              WRITE(7,*) '    Max Principial direction KMIN=', KMIN
          END IF
        END IF
!
      DO K1=1, NDI
          FNORMAL(K1,5)=ORI(K1,2)
      END DO
!
!       L - 1, R - 2, T - 3
        FNORMAL(1,5) = AN(KMIN,3)
        FNORMAL(2,5) = AN(KMIN,2)
        FNORMAL(3,5) = AN(KMIN,1)
      DO K1=1, NDI
!         FNORMAL(K1,5) = AN(KMID,K1)*ORI(K1,2)
          IF ( FCOM == 1) THEN
            IF ( RFCR .GT. ONE ) THEN
              WRITE(7,*) '    RFCR', K1,' FNORMAL =', FNORMAL(K1,5)
            END IF
          END IF
      END DO
```

```
!
!   Solution-dependent state variables
      STATEV(1) = FINDEX(1)
      STATEV(2) = FINDEX(2)
      STATEV(3) = FINDEX(3)
      STATEV(4) = FINDEX(4)
      STATEV(5) = FINDEX(5)
      STATEV(6) = FINDEX(6)
!
!   Maximum criterion
!     RFTL, RFTR, RFTT, RFCL, RFCR, RFCT
      FMAX = MAX(RFTL, RFTR, RFTT, RFCL, RFCR, RFCT)
      IF ( FMAX == RFTL) THEN
          FMAXI = 1
      ELSE IF ( FMAX == RFTR) THEN
          FMAXI = 2
      ELSE IF ( FMAX == RFTT) THEN
          FMAXI = 3
      ELSE IF ( FMAX == RFCL) THEN
          FMAXI = 4
      ELSE IF ( FMAX == RFCR) THEN
          FMAXI = 5
      ELSE IF ( FMAX == RFCT) THEN
          FMAXI = 6
      ELSE
          FMAXI = 0
      END IF
!
      STATEV(7) = FMAXI
!
!
      RETURN
      END SUBROUTINE
!*****************************************************************************
```

Appx.-Fig. 10: Code segments of the damage initiation model (UDMGINI_WOOD_V5e.f)

(Source: own illustration)